

DISSERTATION

OPTICALLY DETECTED ION INSERTION DYNAMICS IN HEXAGONAL TUNGSTEN OXIDE

Submitted by

R. Colby Evans

Department of Chemistry

In partial fulfillment of the requirements

For the Degree of Doctor of Philosophy

Colorado State University

Fort Collins, Colorado

Summer 2021

Doctoral Committee:

Advisor: Justin Barret Sambur

Amy Prieto
Nancy Levinger
Christopher R. Weinberger

Copyright by R. Colby Evans 2021

All Rights Reserved

ABSTRACT

OPTICALLY DETECTED ION INSERTION DYNAMICS IN HEXAGONAL TUNGSTEN OXIDE

Nanoparticle electrodes are attractive for electrochemical energy storage applications because their nanoscale dimensions decrease ion transport distances and generally increase ion insertion/extraction efficiency. However, nanoparticles vary in size, shape, defect density, and surface composition, which impacts charge storage dynamics and warrants their investigation at the single-nanoparticle level. This dissertation demonstrates a non-destructive, high-throughput electro-optical imaging approach to quantitatively measure electrochemical ion insertion reactions at the single-nanoparticle level. Electro-optical measurements relate the optical density change of a nanoparticle to redox changes of its redox-active elements under working electrochemical conditions. The technique was benchmarked by studying Li-ion insertion in hexagonal tungsten oxide ($h\text{-WO}_3$) nanorods. Interestingly, the optically detected response revealed underlying processes that are hidden in conventional electrochemical measurements. This imaging technique may be applied to $h\text{-WO}_3$ particles as small as 13 nm in diameter and a wide range of electrochemical materials such as electrochromic smart windows, batteries, solid oxide fuel cells, and sensors. This dissertation will focus on the impact of single particle $h\text{-WO}_3$ on smart windows and batteries.

Smart windows are devices used to modulate solar radiation into buildings and rely on the same ion insertion reaction as batteries. Electro-optical imaging showed that single nanorods exhibit a particle-dependent waiting time for optical changes (from 100 ms to 10 s) due to Li-ion insertion at optically inactive surface sites. Additionally, longer nanorods have larger optical modulation at equivalent electrochemical conditions than shorter nanorods and exhibit a Li-ion gradient that increases from the nanorod ends to the middle. The particle-dependent ion-insertion kinetics contribute to variable rate for optical density change and magnitudes across large-area smart windows. Single particles modulate optical density (undergo ion insertion reactions) 4 times faster and 20 times more reversibly than thin films made of the same particles.

A smart window device architecture is proposed to maximize lifetime based on these findings. More information can be found in CHAPTER 4:.

Further, the role of crystalline surface facets on the role of ion insertion were investigated. Two samples of h-WO₃ were synthesized with different ratios of surface facets exposed to a Li-ion containing electrolyte. The sample with unique {120} facets exhibited reversible optical switching after 500 cycles and negligible variation in interfacial charge transfer resistance. The (120) surface features an open network of square window channels that may enable reversible ion transport and reduced ion trapping, enhancing the optical switching stability. However, the {120}-dominant sample exhibited lower coloration efficiency (CE) than the {100}-dominant sample. The reduced optical density changes in the {120}-dominant sample could be due to a greater fraction of optically inactive trigonal cavity sites on the {001} endcaps. The results indicate surface facet and particle morphology engineering are viable strategies to enhance the CE and long-term stability/lifetime in electrochromic thin films for smart window applications. More information can be found in CHAPTER 5:.

On average, these h-WO₃ particles exhibit a hybrid charge storage mechanism: both diffusion-limited (battery-like, slower) and pseudocapacitive (capacitor-like, faster) mechanisms contribute to the total charge stored. Individual particles exhibit different charge storage mechanisms at the same applied potential. Longer nanorods store more pseudocapacitive charge than shorter nanorods, presumably due to 1) a surface step edge gradient that exposes large hexagonal window Li-ion binding sites along the nanorod length and/or 2) higher structural water content that influences the Li-ion binding energetics and diffusion behavior. Importantly, penetration depth of Li-ion insertion was quantified which showed that Li ions insert as deep as two-unit cells below the surface. The methodology presented herein can be applied to a wide range of solid-state ion-insertion materials and its implications for future discoveries are discussed. More information can be found in CHAPTER 6:.

ACKNOWLEDGMENTS

I would like to express gratitude to all those who supported me (academically, emotionally, or otherwise) while I was earning my PhD. Special thanks to Justin Sambur for providing challenges that helped me grow intellectually. The challenging questions I received from Justin Sambur, Nancy Levinger, Amy Prieto, and Chris Weinberger were essential to the development of my critical thinking and science communication skills – I was lucky to have a caring committee. Sherry Evans and Russ Evans deserve credit for both conceiving me and providing guidance throughout my formative years. Kevin Galloway of KMG Martial Arts taught me how to maintain focus on objectives while maintaining honesty, integrity, and respect over a decade ago. My ability to persevere is in large part due to these traits, Mr. Galloway. All the faculty and staff of the Chemistry Department at the University of Central Oklahoma were very important to my initial exploration of research. Thanks to Mike Jezercak and Lilian Chooback for propelling me forward during my undergraduate career. Dane Flemming, you made research a blast and you are a great pal. Dallas New should also be acknowledged here.

Daltyn Moeckle (Moeckel?), though I cannot remember how to spell your last name at the time of writing, our relationship was an important catalyst for the development of my emotional intelligence, without which would have spelled my demise by now. Jokes aside, thank you.

Thanks to Connor Steward and Hayden Contreras for always playing and pretending to be scientists when we were kids. We call it “imagination” as children and “creativity” as adults, but regardless of the name, you two remind me of its importance.

In alphabetical order of the second-to-last letter of their first name, thanks to Ethan Kohrumel (Eevee), Brenden M.M. Balch (Beezo), and Andrew Simpson (CD), for being amazing friends. The comradery exhibited by you gentlemen is (in most cases, e.g. CD) exemplary and you all have my upmost respect. Special points to Brenden for helping with mathematical issues throughout my PhD. It is an honor to be able to include you on a publication that served as an entire chapter of this dissertation.

If you did not see your name on the list, please refer to the first sentence of this acknowledgement.

DEDICATION

The pursuit of this PhD is entirely due to my selfish desire to learn new things and have life experiences that are challenging and rewarding. However, there is one individual worthy of this dissertation's dedication. So, to the memory of a great woman by the name of Lou Warren, lovingly referred to as "Nan", who once offered the analogy "Tough titty said the kitty, there ain't no more milk" when questioned on the hardships of life.

TABLE OF CONTENTS

ABSTRACT.....	ii
ACKNOWLEDGMENTS	iv
DEDICATION	vi
LIST OF FIGURES	x
CHAPTER 1: INTRODUCTION	1
1.1 Probing Single Particle Ion Insertion Reaction Dynamics.....	2
1.2 Hexagonal Tungsten Trioxide (h-WO ₃) as a Model System.....	5
CHAPTER 2: BACKGROUND	7
2.1 Electrochromism	7
2.1.1 Electrochromic Mechanisms.....	7
2.2 Beer-Lambert Law for Electrochromics	9
2.3 A Note on Electrochromic Smart Windows	11
CHAPTER 3: EXPERIMENTAL DESIGN.....	12
3.1 Material Synthesis.....	12
3.2 Characterization	13
3.2.1 PXRD.....	13
3.2.2 TEM	14
3.2.3 SEM and AFM.....	15
3.2.4 Characterization Summary.....	18
3.3 Experimental Design.....	19

3.3.1 Overview.....	19
3.3.2 Choosing A Light Source.....	20
3.3.3 Electrochemical Flow Cell.....	21
3.3.4 Experimental Set Up	23
3.3.5 Optical / SEM image correlation	26
3.3.6 Image Processing	27
3.3.7 X-Y Stage Drift.....	31
3.3.8 Calculating the Optical Density Profile Along a Single Nanorod	32
3.3.9 Limit of Detection.....	33
 CHAPTER 4: INVESTIGATION OF STRUCTURE-PROPERTY RELATIONSHIPS IN HEXAGONAL WO ₃ NANORODS	 35
4.1 Kinetic Model	36
4.2 Results and Discussion	40
4.2.1 Coloration and Bleaching Dynamics in Single h-WO ₃ Nanorods	40
4.2.2 Effect of Particle Size and Surface Structure on Optical Density Magnitude and Dynamics....	46
4.2.3 Role of Particle-Particle Interfaces on Electrochromic Dynamics and Reversibility	53
4.2.4 Material Insight from Cyclic Voltammetry.....	57
4.3 Conclusion	62
 CHAPTER 5: SURFACE FACET-DEPENDENT ELECTROCHROMIC PROPERTIES OF WO ₃ NANOROD THIN FILMS	 64
5.1 Results.....	65
5.2 Discussion	81

5.3 Conclusion	86
CHAPTER 6: QUANTIFYING CAPACITIVE-LIKE AND BATTERY-LIKE CHARGE STORAGE CONTRIBUTIONS USING SINGLE NANOPARTICLE ELECTRO-OPTICAL IMAGING.....	87
6.1 Results and Discussion	88
6.1.1 Materials Synthesis and Characterization	88
6.1.2 Hybrid Charge Storage Mechanism	91
6.1.3 Single Nanoparticle Charge Storage Behavior	94
6.1.4 Quantifying Pseudocapacitive Chare Storage at Surface and Sub-Surface Sites.....	99
6.2 Algorithms and Derivations	101
6.2.1 Mean Square Error Algorithm	101
6.2.2 Quantifying Li ⁺ Insertion Depth.....	103
6.3 Conclusion	107
CHAPTER 7: CONCLUSIONS AND OUTLOOK	108
BIBLIOGRAPHY	110
APPENDIX A.....	120
LIST OF ABBREVIATIONS.....	121

LIST OF FIGURES

Figure 1.1 – Ragone plot. Power and energy density for representative electrochemical storage devices. ⁶	1
Figure 2.1 – Smart window. Electrochromic smart windows absorb IR radiation in the colored state, but do not in the transparent state.	11
Figure 3.1 – Schematic representing the two-step process for making hexagonal WO₃ nano rods. 1) add precursors and use correct temperature, pH, and solvent. 2) clean and store nanorods.	13
Figure 3.2 – PXRD structural characterization for WO₃ nanorods. Black circles represent data points and red lines represent the P6/mmm, JCPDS 00-033-1387 reference.	13
Figure 3.3 – Crystallographic characterization of h-WO₃. a) TEM image showing the rod-like morphology of the nanoparticles. b) High resolution TEM image showing a nanorod with regular atomic spacing. Inset is a selected area diffraction pattern for the nanorod showing a regular atomic spacing of 3.83 Å.....	15
Figure 3.4 – SEM images of nanorods. a) An SEM image showing the different morphologies of nanorods. b) The same SEM image as in (a), but with the hexagonal capped nanorods pointing at the detector highlighted with black outlines.	16
Figure 3.5 – Atomic force microscopy (AFM) of a hexagonal nanorod. a) AFM image of a nanorod. The white line indicates where the line profile was drawn to obtain (b). b) The height profile obtained from the white line drawn in (a). The gray dashed lines illustrate how the high profile can originate from a particle with a hexagonal prism morphology.....	17
Figure 3.6 – Determine particle length and width from SEM. a) Representative SEM image. b) Length of scale bar determined by user clicks (red cross) cut in from (a). c) Length and width of nanorods selected by user clicks (red cross).....	17

Figure 3.7 – Correlated SEM and AFM. a) SEM image with 3 individual nanorods marked. b) AFM image with the same individual nanorods marked. 18

Figure 3.8 – Electro-optical overview a) An optically transparent electrochemical cell is mounted on a microscope and an LED or lamp illuminates the sample. The light transmitted through the sample is collected by a microscope objective and imaged on an EM-CCD camera (not shown). b) optical image of an object. c) SEM image correlated with the optical image in (b) of the same object. d) Representative potential dependent optical density changes with time. 19

Figure 3.9 – Transmission spectra of h-WO₃ on ITO under electrochemical bias. The film is in the colored/tinted state at -1.0 V and bleached/transparent at 1.5 V vs Ag/AgCl. Optical modulation increases with increasing wavelength. 20

Figure 3.10 – Electrochemical flow cell. a) Cartoon of the electrochemical flow cell with all necessary components labeled. b) photograph of the electrochemical flow cell with all necessary components labeled. 21

Figure 3.11 – Cartoon overview of the electro-optical microscope set up. An optically transparent 3-electrode electrochemical cell is mounted on an inverted microscope and an LED or lamp illuminates the sample from above. The light transmitted through the sample is collected by a microscope objective and imaged on an EM-CCD camera. The CCD camera and potentiostat are connected to a data acquisition card (DAQ). 25

Figure 3.12 – Optical and SEM correlation and identification of single nanorods. a) optical image of the scratch area. b) SEM image of the same area as indicated in (a) by the red dashed square. c) optical image of h-WO₃ nanorods. d) corresponding SEM image of the same particles. e) identification of a single nanorod. (c-e) red ovals indicate the same object. 27

Figure 3.13 – Assigning time to camera TTL signal. a) Digital camera shutter TTL signal. b) Derivative of digital camera shutter TTL signal in (a). c) Digital camera shutter TTL signal with blue lines marking “on” and “off” points for camera exposure. 28

Figure 3.14 – Image processing to assign potential and current. a) Representative transmission image stack during a cathodic polarization pulse. b) Camera shutter and potentiostat signals measured by the DAQ. Top: camera shutter, middle: applied potential, bottom: electrochemical current. The red symbols represent the camera shutter open time points..... 29

Figure 3.15 – Image processing for object boundaries in optical images. a) Average optical transmission image of lithiated WO₃ nanoparticles (NPs) on the ITO electrode. b) same as in (a), but for WO₃ NPs in the delithiated state. c) Difference image obtained from (a) and (b). d) Thresholded binary image of (c). White pixels indicate lithiated particles and black pixels represent ITO pixels or inactive particles..... 30

Figure 3.16 – Image analysis procedure for single particle $\Delta OD(t)$ trajectories. a) Representative bright field transmission image of a h-WO₃ NR/ITO electrode. b) Cropped transmission image from the red square in (a). The blue and green pixel areas represent equal-sized pixel areas from a WO₃ NR and ITO substrate, respectively, and therefore the light transmitted through a single nanorod (I) and the ITO substrate (I_0). c, I (blue circles) and I_0 (green squares) trajectories from the regions in (b). d) $OD(t)$ trajectory calculated according to $-\log_{10}(I/I_0)$ in (c)..... 31

Figure 3.17 – Illustration of x-y drift. a) Binary image containing one object with the centroid (yellow circle) at some frame, n . b) Binary image of the same object as in (a) but shifted in the x-y plane. 32

Figure 3.18 – Experimental procedure to calculate the optical density profile along a single nanorod. a) SEM image of a nanorod. The nanorod major axis, end points, and centroid are extracted. The red line represents a linear fit to the nanorod pixels and therefore the major axis. The green squares represent the nanorod end points. The blue square represents the centroid position. b) Optical image of the same nanorod in (a). The red line, green squares and blue hollow square represents the nanorod major axis, end points, and centroid position, respectively. c) Same transmission as in (b) but the blue squares represent 200 nm segments for ΔOD versus distance to centroid analysis. 33

Figure 3.19 – Determination of the limit of detection. (a) Single background pixel $\Delta OD(t)$ trajectory during a cathodic potential pulse (-1.0 V vs Ag/AgCl). The data points represent the average response of

three pulses. (b) Histogram of the data in (a). The data was fit with a Gaussian function to obtain the population mean $\mu = 2.75 \times 10^{-4}$, the standard deviation σ (3.70×10^{-3}), and the single pixel limit of detection ($\text{LOD} = \mu + 3\sigma = 1.11 \times 10^{-2}$). (c) The distribution of 58 single pixel LOD values. The single pixel average $\text{LOD} = 1.08 \times 10^{-2}$ 34

Figure 4.1 – Single particle electro-optical kinetics. A cathodic chronoamperometric pulse (-1.0 V vs Ag/AgCl) induces an optical response with three distinct regions in h-WO₃: 1) a period with no optical change (t_{wait}), 2) a burst, and 3) a slow rise..... 36

Figure 4.2 – Current-time response of these h-WO₃ NR/ITO electrodes. a) Potential versus time waveform and (b), corresponding current versus time response (black dots). The red line represents a fit to the current versus time response using Equation 4-1. Fitting current-time data with Equation 4-1 yields $A = 5.1\text{e-}06$ C/s-cm², $k_{\text{pseudo}} = 0.58$ s⁻¹, and $D' = 1.5\text{e-}06$ C/s^{3/2}-cm² for the bleach and $A = 4.6\text{e-}06$ C/s-cm², $k_{\text{pseudo}} = 0.85$ s⁻¹, and $D' = 1.4\text{e-}05$ C/s^{3/2}-cm² for coloring. Ag / AgCl was used as a reference electrode. 38

Figure 4.3 – Thickness corrected optical density response at -1.0 V vs Ag/AgCl fit with kinetic model. A cathodic chronoamperometric pulse induces an optical response with three distinct regions in h-WO₃: 1) a period with no optical change (t_{wait}), 2) a burst, and 3) a slow rise all fit with Equation 4-4 (red line). Error bars are standard deviation between three cycles. 40

Figure 4.4 – Quantitative analysis of single nanoparticle optical density trajectories. a) SEM image of a single WO₃ nanorod (length = 1.64 μm , width = 0.11 μm). b) $\Delta\text{OD}(t)_d$ trajectory of the same nanorod in (a). The $\Delta\text{OD}(t)_d$ data points and error bars represent the mean and standard deviation of 3 consecutive cathodic (-1.0 V vs Ag/AgCl) and anodic ($+1.5$ V vs Ag/AgCl) potential cycles. The dashed vertical lines represent $t_{90\text{color}}$ (67.78 s) and $t_{90\text{bleach}}$ (4.33 s). The solid red line represents the fit to the data using equation (2) in Methods. c) $\Delta\text{OD}(t)_d$ trajectory in (b) from $t = 0$ to 30 s, showing $t_{\text{wait}} = 1.78$ s. (d-f) same data as (a-c), but for a shorter WO₃ nanorod (length = 0.52 μm , width = 0.16 μm) with longer $t_{90\text{color}}$ (115.53 s), $t_{90\text{bleach}}$ (3.33 s), and slightly longer t_{wait} (2.78 s). (g-i) same data as (a-c), but for a shorter

WO₃ nanorod (length = 0.67 μm , width = 0.10 μm) with longer $t_{90color}$ (96.78 s) , $t_{90bleach}$ (209.33 s), and much longer t_{wait} (18.03 s). 41

Figure 4.5 – Li-ion binding sites in hexagonal WO₃. Structure of *h*-WO₃ with *c*-axis a) perpendicular and b) parallel to the plane. The TC site is optically inactive. The HW and SW sites are optically active..... 42

Figure 4.6 – Electrochemical characterization of ensemble WO₃ nanorod film. a) Electrochemical response versus scan rate according to equation (S1). The circles and squares represent currents measured at –1.0 V (circles) and –0.08 V (squares) vs Ag/AgCl, respectively. The solid red line represents a linear fit and the dashed lines represent the 95% confidence intervals. b) Fraction of injected charge using the constants k_1 and k_2 from the fit in (a) according to Equation 4-6. The blue and orange bars represent the fractions of pseudocapacitive surface charge and diffusion-controlled bulk charge, respectively. Error bars represent the standard error of the mean. 43

Figure 4.7 – X-ray photoelectron spectroscopy of a h-WO₃ NR film. a) before and b) after coloration for 600 s at –1.0 V vs Ag / AgCl. The blue dots represent the data and the solid red lines represent fits from Multipack (v. 9.3) software. The red and green dashed vertical lines represent expected peak positions of W 4f core level binding energies that are consistent with W⁶⁺ and W⁵⁺ oxidation states, respectively. The chamber pressure was 10⁻⁸ mbar. 44

Figure 4.8 – Examples of anomalous optical modulation behavior. a, c, e) SEM image of a single WO₃ nanorod. b, d, f) Normalized OD trajectory for the pictured nanoparticle (black circles) compared to the normalized trace for the average of all single nanoparticles (blue squares) and film (grey circles). The error bars for the average of singles represent the standard error of the mean. Error bars for abnormal OD trajectories are omitted for clarity. 45

Figure 4.9 – Correlation between optical density magnitude and nanorod structural properties. a) The particle thickness-corrected change in optical density ΔODd_{max} versus nanorod length (Pearson correlation coefficient $\rho = 0.34 \pm 0.06$, $N = 98$ particles). b) Charge inserted into optically active surface sites per electrochemically active surface area of the nanorod $Q_{pseudoactive}$ versus length ($\rho = 0.52 \pm$

0.05, $N = 83$ particles) and c) bulk charge per unit volume $Q_{\text{diffactive}}$ versus length ($\rho = 0.33 \pm 0.07$, $N = 83$ particles). The black circles in (a-c) represent data from individual nanorods and the solid red line is a linear fit to show the general trend. d) SEM image of a single nanorod. The distance between all vertical black and red lines represent 200 nm segments for sub-particle-level trajectory analyses. Small nanorod segments extending beyond the vertical black lines were not analyzed. e) Representative $\Delta OD(t)$ trajectories measured from the middle (hollow green circles) and end segments (hollow and solid blue squares) on the single nanorod in in (d). f) Maximum ΔOD versus distance from nanorod centroid calculated from the trajectory analyses in (e). The red line represents a linear fit to the segmented data. Error bars are the standard deviation of the ΔOD within the 200 nm segment. g) ΔOD^{max} of 13 single particles versus its slope parameter defined in (f). The red line is a linear fit to show the general trend ($\rho = 0.73 \pm 0.31$)..... 46

Figure 4.10 – High resolution TEM imaging of the h-WO₃ nanorod sample. a-b) Representative TEM images showing perpendicular (indicated by yellow arrows) and parallel step edge features along single nanorods. c) TEM image showing two physically coupled nanorods and d) a zoom-in view of the interfacial region in (c) that shows a heterogeneous interfacial structure at the particle-particle interface. 47

Figure 4.11 – Correlation between electrochromic kinetic parameters and physical properties of individual nanorods. (a-d) Correlations between surface charge transfer rate constant k_{pseudo} and length, width, geometric surface area (GA) exposed to electrolyte, and volume. (e-h) and (i-l) Correlations between $t_{90\text{color}}$ and $t_{90\text{bleach}}$ versus length, width, geometric surface area, and volume. The black circles represent data from the 83 fitted individual nanorods and the red line represents a linear fit to show the general trend. Correlation coefficients are represented as ρ . Error bar for the Pearson’s correlation coefficient calculated according to ref.¹⁰⁵ 49

Figure 4.12 – Correlation between t_{wait} and physical properties. (a-c) Correlation between t_{wait} and width, geometric area exposed to electrolyte, and volume. Correlation coefficients are represented as ρ . d) Correlation between geometric area corrected charge injected predicted from the model versus length. Error bar for the Pearson’s correlation coefficient calculated according to ref.¹⁰⁵ 50

Figure 4.13 – Coloration and bleaching kinetics at the single particle-level. **a,** Waiting time for optical modulation versus nanorod length ($\rho = -0.11 \pm 0.07$). Inset shows the distribution of waiting times. **b,** Coloration versus bleaching kinetics; $t_{90color}$ versus $t_{90bleach}$ ($\rho = 0.65 \pm 0.04$). **c,** $t_{90color}$ versus k_{pseudo} ($\rho = -0.38 \pm 0.06$). The black circles in (a-c) represent data from single nanorods and red line is a linear fit to show the general trend..... 51

Figure 4.14 – Optical density correlations with kinetic parameters. Correlations between particle thickness corrected maximum optical density (ΔOD_{dmax}) and a) t_{wait} , b) k_{pseudo} , c) $t_{90color}$, and d) $t_{90bleach}$. Error bar for the Pearson’s correlation coefficient calculated according to ref.¹⁰⁵ 52

Figure 4.15 – Electrochromic dynamics and reversibility of nanorod clusters and thin films. a) SEM image of a particle cluster containing 3 nanorods. (b-c) $\Delta OD(t)$ trajectory of the cluster in (a, black trace) compared to the average trajectory of 102 single nanorods (blue trace). D) $\Delta OD(t)$ trajectory for the cluster in (a) during three consecutive color and bleaching cycles. The dashed horizontal line in (d) represents ΔOD at 0 s. (e-h) and (i-l) are the same as (a-d), but for a large 25-100 particle cluster and a thin film electrode, respectively. 54

Figure 4.16 – Role of particle-particle interactions on electrochromic dynamics and reversibility. a) $t_{90color}$ and $t_{90bleach}$ versus particle cluster size. Fraction of irreversible (b) bleaching and (c) color cycles versus particle cluster size. The total number of clusters analyzed for sizes 2, 3, 4, 5, and >25 were 134, 72, 41, 32, and 19, respectively. Error bars in (a-c) represent the standard error of the mean. (d-e), SEM image of a two-particle cluster with side-by-side (area contact) configuration and top-and-bottom (point contact) configuration. F) Fraction of irreversible coloration and bleaching cycles for 81 side-by-side clusters (243 total cycles) and 30 top-and-bottom clusters (90 total cycles). 55

Figure 4.17 – Comparison of conventional and electro-optical cyclic voltammetry. a) Single object optical density measurements (left axis) and ensemble-level total charge passed (right axis) plotted versus the applied potential from a CV at 10 mV / s. The OD data represents the average response from 38 objects (single particles and clusters). b) Electrochemical current (i , black line) and its derivative (di/dt , green line)

versus time during the CV measurement. The inset shows a zoomed-in region of the data to illustrate the rise of the derivative signal. c) Comparison of the optically detected current (dOD/dt , green data, left axis) and i (right axis, black line) versus the applied electrochemical potential. 57

Figure 4.18 – Electro-optical imaging of single nanoparticle voltammetry. a-c) Optically detected current, dOD/dt (green data points), versus applied electrochemical potential for three individual nanorods. The yellow line represents a 5-point smooth to show the general trend. Right panels represent SEM images of the single particles. d-f) same as (a-c), but for particle clusters. g) Single particle-averaged dOD/dt data from the three particles in (a-c) compared to the ensemble-average electrochemical current (black line) that was measured from the entire cell. h) Particle cluster-averaged dOD/dt data from 10 individual clusters compared to the ensemble-average electrochemical current. 60

Figure 4.19 – Proposed smart window device architecture for improved performance. Side and top views of isolated WO_3 NRs deposited on a high surface area transparent conductor (e.g., ITO). The ITO/ WO_3 layers could be stacked between layers of liquid or solid-state electrolyte. 63

Figure 5.1 – Synthesis and fabrication of h- WO_3 electrochromic samples. Synthesis scheme for (a) WO_3 -{120} NR and (b) WO_3 -{100} NRs. 66

Figure 5.2 – Crystal structure and morphology of h- WO_3 NRs. a) PXRD patterns for WO_3 -{120} and WO_3 -{100} samples (black data points). Red dashes indicate reference peak patterns (top: P6/mmm, JCPDS 04-007-2322 WO_3 -{120}; bottom: P6/mmm, JCPDS 00-033-1387 WO_3 -{100}). b-c) Representative SEM images of b) WO_3 -{120} and c) WO_3 -{100} films. 67

Figure 5.3 – Surface facet characterization and illustration. a) HRTEM image of a single NR from the WO_3 -{120} sample, observed via a top-down view of the {100} surface. b) HRTEM image of a different single NR in the WO_3 -{120} sample, observed via a top-down view of the {120} surface. c) HRTEM of a single NR in the WO_3 -{100} sample. Insets of (a-c) represent FFT images. d-e) Cartoon illustration of WO_3 -{120} and WO_3 -{100} samples drawn to scale (note: 3.5× for WO_3 -{120}). 68

Figure 5.4 – Illustration of symmetry related planes in the hexagonal WO_3 system. 69

Figure 5.5 – Scanning probe microscopy analysis of NR films. a-b) Representative height profiles showing the height change from the bare ITO substrate to WO₃-{120} and WO₃-{100} NR films, respectively. 70

Figure 5.6 – Facet dependent transmission spectra. Percent transmission spectra for (a) WO₃-{120} and (b) WO₃-{100} films one cycle coloring at -1.0 V and bleach at 0.5 V vs Ag/AgCl. 71

Figure 5.7 – Optical changes at 940 nm. a) ΔOD changes versus time of 474 nm \pm 170 nm WO₃-{120} films for cycles 3-5 (black filled circles) and 498-500 (red open circles). b) same as (a) but for a 1315 nm \pm 300 nm WO₃-{100} sample. Horizontal gray lines represent maximum and minimum ΔOD values in cycle 3 and serve as a visual guide for differences between ΔOD in early versus late cycles..... 71

Figure 5.8 – Facet-dependent electrochromic properties. a) Thickness corrected OD changes, ΔOD_d , versus time of 474 nm \pm 170 nm WO₃-{120} films for cycles 1-2 (black filled circles). b) same as (a) but for a 1315 nm \pm 300 nm WO₃-{100} sample. 72

Figure 5.9 – Thickness corrected optical changes at 940 nm. a) ΔOD_d changes versus time of 474 nm \pm 170 nm WO₃-{120} films for cycles 3-5 (black filled circles) and 498-500 (red open circles). b) same as (a) but for a 1315 nm \pm 300 nm WO₃-{100} sample. Horizontal gray lines represent maximum and minimum ΔOD_d in cycle 3 and serve as a visual guide for differences between ΔOD_d in early versus late cycles. Opaque areas represent error within one standard deviation. 73

Figure 5.10 – CE fitting. ΔOD versus charge inserted charge density, Q , to determine the coloration efficiency. Linear fit is in red..... 75

Figure 5.11 – Coloration efficiency of NR samples. a-b) CE (black filled circles) and relative change in ΔOD (open red circles) for WO₃-{120} and WO₃-{100} for the first 30 cycles. Solid lines are a guide for the eye. (c) CE versus cycle number for WO₃-{120} and WO₃-{100} films. 76

Figure 5.12 – Electrochemical impedance spectroscopy. a-b) Nyquist plot for the WO₃-{120} and WO₃-{100} samples before and after 500 cycles. Data acquired at -1.0 V vs Ag/AgCl over the range of 20 Hz to 150 kHz. The inset in panel (a) shows the Randle circuit used for fitting EIS data. 76

Figure 5.13 – XPS analysis. a-h) XPS data before (black, filled) and after 500 cycles (red, open) for C1s, Li 1s, O 2p, and W 4f regions for WO₃-{120} and WO₃-{100} films. W 4f data (d,h) were fit to W 4f_{7/2} and 4f_{5/2} peaks at 35.4 eV and 37.6 eV (green), corresponding to W⁶⁺. W 4f_{7/2} and 4f_{5/2} peaks at (d) 34.0 eV and 36.1 eV and (h) 34.3 eV and 36.5 eV (blue) were assigned to W⁵⁺. The composite fits are shown in gold. All peak intensities are normalized to the tungsten 4f_{7/2} peak for each sample. 78

Figure 5.14 – 2D TOF-SIMS spectra for WO₃-{120}. Top, left to right: total, C, O. Bottom, left to right: F, Cl, optical image. Brighter colors indicate larger abundance. 79

Figure 5.15 – 2D TOF-SIMS spectra for WO₃-{100}. Top, left to right: total, C, O. Bottom, left to right: F, Cl, optical image. Brighter colors indicate larger abundance. 80

Figure 5.16 – Sputter time TOF-SIMS. a) The intensity of In, Li, W, and C species as a function of sputter time into the depth of the film for WO₃-{120}. b) same as (a) but for WO₃-{100}..... 81

Figure 5.17 – Structure and binding sites in hexagonal WO₃. Top (perpendicular) eye view looking down into the (a) (001) plane showing trigonal cavity and hexagonal window ion binding sites, (b) (100) plane showing square windows, and (c) (120) plane also showing square window sites..... 82

Figure 5.18 – SEM images before (pristine) and after 150 cycles. Top-down image of WO₃-{100} before (top left) and after (top right cycling) and cross-sectional image before (bottom left) and after (bottom right) cycling. These thick films were not the same films as shown in the main text. 85

Figure 6.1 – Thermogravimetric analysis (TGA). a) The weight of the nanoparticle sample as a function of time. b) The derivative of weight with temperature plotted against temperature. 89

Figure 6.2 – Energy dispersion x-ray spectroscopy (EDS) for a cluster of nanorods. a) SEM image of nanorod cluster on nickel foil. b-e) W, O, Na, and NI element specific maps from EDS. 89

Figure 6.3 – PXRD of WO₃ nanorods on a zero-diffraction Si puck. PXRD from 10 2θ to 80 2θ..... 90

Figure 6.4 – Potential dependent single particle optical response. The particle thickness-corrected change in optical density (ΔOD_d) of the single WO₃ nanorod shown in the inset during a normal pulse voltammetry experiment. The potential was stepped from a constant anodic potential (+1.5 V) to different cathodic potentials (from -0.2 V to -1.0 V vs Ag/AgCl)..... 91

Figure 6.5 – Particle averaged $\Delta OD_d(t)$ analysis. a) $\Delta OD_d(t)$ trajectories as a function of applied cathodic step potential over the range of -0.4 V to -1.0 V vs Ag/AgCl. The red line represents fits to the data using Equation 5. Error bars on the data points represent the standard deviation between three cathodic cycles. b) Diffusion-limited (Q_{diff}) and pseudocapacitance (Q_{pseudo}) charge contributions to the total charge obtained from the fits in (a). The error bars are as the value obtained when the mean square error of the fit doubles. The red line represents a linear fit to the pseudocapacitance contribution, with an $R^2 = 0.97$ and a slope = 2.8×10^{-13} F, average capacitance is 6.4×10^{-13} F/cm² $\pm 5 \times 10^{-13}$ F/cm². 92

Figure 6.6 – Representative examples of single particle charge storage behavior. a, b) SEM images of a single WO₃ nanorods. c) The corresponding $\Delta OD_d(t)$ traces at -0.4 V, -0.5 V, and -1.0 V respectively. The red lines represent a fit to the data using Equation 5 and contributions from both ΔQ_{diff} and ΔQ_{pseudo} . d) same as (c), but for the other nanorod. The red line fit for -0.5 V data represents a fit to Equation 6-3 with contributions from ΔQ_{diff} only. The red line fit for -1.0 V data represents a fit to Equation 6-1 with contributions from ΔQ_{diff} and ΔQ_{pseudo} 94

Figure 6.7 – Classifying charge storage mechanisms of single nanoparticles. a) Distribution of single particles that exhibited a diffusion-limited (red bar), hybrid diffusion-limited and pseudocapacitive mechanism (yellow bar), and anomalous mechanism (blue bar; see main text for description). No optical changes were detected at potentials more positive than -0.4 V. b) Distribution of charge storage mechanisms for single particles at their onset potential. E_{onset} is defined as the most positive potential where the $\Delta OD_d(t)$ signal exceeds three-times the limit of detection. 96

Figure 6.8 – Correlation of potential onset of optical activity (E_{onset}) with physical parameters. a-d) show the Pearson’s correlation with E_{onset} and active particle area, length, width, and volume, respectively. The Pearson’s correlation coefficients for (a-d) are $\rho = -0.197 \pm 0.10$, $\rho = -0.024 \pm 0.11$, $\rho = -0.196 \pm 0.10$, $\rho = -0.230 \pm 0.10$, respectively. 97

Figure 6.9 – Length distributions for different charge storage fits at -0.4 V vs Ag/AgCl. a) The distribution of nanoparticle lengths that were fit with a diffusion plus pseudocapacitance component at -0.4 V. b) The distribution of nanoparticle lengths that were fit with a diffusion only procedure at -0.4 V. 98

Figure 6.10 – Quantifying surface and near surface sites that contribute to the pseudocapacitive

charge storage mechanism. a) Q_{pseudo} versus the number of surface W atoms for a particular nanorod. from 0.9× to 3× the number of W atoms on the surface of a particular nanorod. The red line is the diagonal and represents 100% Li^+ occupation of surface W sites. The color gradient represents the nanorod length. The cartoon nanorod schematically show that short and long nanorods have less and more pseudocapacitive charge storage contributions to the total charge, respectively. b) Li-ion insertion depth versus nanorod length. See Supplementary Note 2 for insertion depth calculation details. The insertion depth scales linearly with length (Pearson correlation coefficient is 0.43 ± 0.6). Error bars in Li^+ inserted represent the standard deviation from optical density propagated through the fitting procedure. The error in surface tungsten atoms was calculated using 5% relative error in SEM imaging propagated through the calculation. The error in nanorod length was calculated using 5% relative error in SEM, but the error in length was not used to calculate the Pearson correlation coefficient. 100

Figure 6.11 – Choosing a fitting routine. a,b) show a single particle ΔOD trace fit with diffusion only

(Equation 6-3) and pseudocapacitance plus diffusion (Equation 6-1), respectively at $-1.0 \text{ V vs Ag/AgCl}$. The fits are shown as red lines and the data points are black dots. Error bars represent the standard deviation between three cathodic pulses. Inset shows the single nanoparticle. c) The distributions of mean square error (MSE) between the fit and data points for diffusion fitting. d) The distributions of mean square error between the fit and data points for pseudocapacitance plus diffusion fitting. 102

Figure 6.12 – Choosing a fitting routine. a,b) show a single particle ΔOD trace fit with diffusion only

(Equation 6-3) and pseudocapacitance plus diffusion (Equation 6-1), respectively at $-0.4 \text{ V vs Ag/AgCl}$. The fits are shown as red lines and the data points are black dots. Error bars represent the standard deviation between three cathodic pulses. Inset shows the single nanoparticle. c) The distributions of mean square error (MSE) between the fit and data points for diffusion fitting. d) The distributions of mean square error between the fit and data points for pseudocapacitance plus diffusion fitting. 103

Figure 6.13 – Cross sections of a nanorod. a) By symmetry, we have $w = 2a$ (b) The situation shows that

$b + 2x = a$ 105

CHAPTER 1: INTRODUCTION

Advances in energy storage technology is integral to the development of energy intensive personal electronics and electric vehicles beyond small cars (busses and planes).¹⁻³ **Figure 1.1** shows a Ragone plot with several energy storage devices as a function of energy density and power density. Gray dashed lines indicate charge/discharge times in seconds and C-rate. Power density relates the speed that a given amount of energy can be stored or released per volume of material. Energy density is the amount of energy that can be stored per volume of material. Development of affordable devices with high power and energy density (red oval) and long lifetimes (can be cycled many times) is necessary to fulfill commercial and residential energy needs.^{4,5}

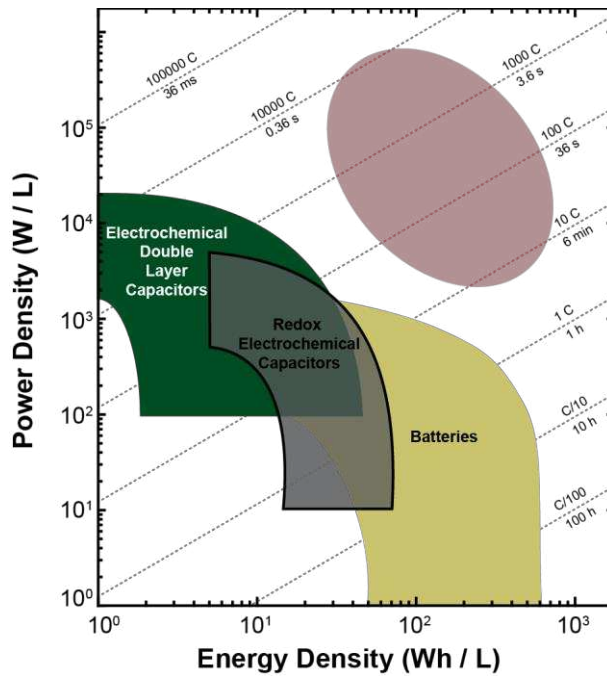


Figure 1.1 – Ragone plot. Power and energy density for representative electrochemical storage devices.⁶

Technologies based on ion insertion reactions may bridge the gap between high energy and power density devices if the total volume of the electrode material can be utilized for charge storage at fast speeds.⁷⁻⁹ Building that bridge requires research strategies spanning many approaches and disciplines. Ion

insertion reactions are faradaic in nature, allowing relatively large amounts of energy to be stored chemically at the surface and in the bulk of materials. Unfortunately, it is this slow diffusion of ions into the material that limits current electrochemical energy storage devices from operating quickly and reversibly. Reducing particle sizes to the nanoscale increases the surface area of the material in contact with the ion-containing electrolyte and is a popular strategy for improving overall charge / discharge rates¹⁰⁻¹³, though some reports show nanosizing is not necessary for high rate performance.^{7,14-16} Shape, defect density, and surface composition are all physical factors that impact charge storage dynamics and exist in both nano and micro sized materials.¹⁷⁻¹⁹ Understanding fundamental interactions between ions and their host structures will provide the tools necessary to manipulate or create new systems that meet kinetic demands.

1.1 Probing Single Particle Ion Insertion Reaction Dynamics

Characterizing the physical and chemical changes of electrode materials during device operation is one method to advance energy storage technologies. Comparing different ensemble devices provides valuable chemical insight, but performances from many particles with wide size, chemical impurity, and physical defect distributions can limit interpretation. Ensemble samples are only partially representative of the composite material.²⁰ Therefore, experimental methods that reveal the role of small chemical or physical differences by contrasting isolated particles (that are nominally the same) are particularly useful. Isolated particles allow for the study of intrinsic material properties without complication of particle-particle interactions, and it is possible to more accurately probe structure / morphology dependent performance. This section will give a broad overview of the techniques used to probe single particle ion insertion reactions and end with a brief summary of the new methodology developed for the investigations in this thesis. All techniques have advantages and disadvantages and should be viewed as complementary rather than exclusionary.

The scientific community has demonstrated great creativity in the face of challenges presented by single particle experiments. Electron, optical, vibrational, and magnetic imaging during electrochemical processes all present their own and often unique major technical hurdles when adapted to single particle studies, in spite of which scientific exploration has flourished.

In operando transmission electron microscopy (TEM) has been used to image real-time atomic-level structural changes in single nanoparticles during the ion insertion process.²¹⁻²³ This approach yields real-time dynamic process of ion insertion by monitoring the phase change accompanied by lithiation in nanorods. This “lithiation front” denoted by low contrast in the TEM serves as a handle to determine charge storage rates in both metallic and semiconducting nanorods.²¹⁻²⁴ Atomic level resolution on either side of the lithiation front indicates crystalline phase changes caused by the ion-insertion reaction.

X-ray imaging methods track oxidation state changes of elements in single-nanoparticle electrodes and have revealed how film porosity, particle shape, orientation, and composition contribute to the electrochemical response of nanoparticle film electrodes.^{25,26} Single particle X-ray experiments have shown special distribution of reduced metal sites in $\text{Li}_2\text{Mn}_2\text{O}_4$, emphasizing the impact of crystalline facets.²⁷ 3-D topographic reconstruction of K-edge spectra in a single LiFePO_4 particle showed lithiation to be uniform in all directions – the highest concentration of Li after delithiation to FePO_4 was in the center of the particle.²⁸ Surface plasmon resonance microscopy (SPRM) has been used to measure Li-ion insertion/extraction dynamics and phase changes in LiCoO_2 nanoparticles with 50 fA sensitivity and 20 ms time resolution.²⁹ SPRM measures the refractive index change associated with Li-ion insertion/extraction in single nanoparticles; the technique does not measure electrochemical currents at the single nanoparticle level. Electron and X-ray measurements typically require specialized instrumentation and synchrotron light sources and require many experiments to probe enough particles to generalize populations and detect trends. Many electron measurements have focused on rod-like morphology, as the limited field of view make other shapes more challenging to fully characterize with atomic resolution. SPRM is limited to materials that

undergo large enough refractive index changes during ion insertion which may exclude samples that do not undergo a phase change.

Fourier transform infrared (FT-IR) spectroscopy and Raman microspectroscopy have been used to characterize reactive intermediates and adsorbates on electrode surfaces^{30,31} as well as to probe lattice dynamics, crystal structure, ion flow, and/or oxidation state of an electrode material.^{32,33} Some Raman configurations can simultaneously study chemical composition, surface functionalization, and size of individual nanoparticles during chemical reactions.³⁴ Recently, Yamanaka et al. used single particle Raman microspectroscopy to contrast the structural transformation, reactivities, and mechanisms of fluorine shuttle batteries by monitoring structural deformation in BiF₃.³⁵ The spatial resolution of infrared and Raman microspectroscopy is defined by the excitation spot size and is typically limited to the investigation of micrometer-sized particles. IR microspectroscopy is limited to compatible electrode materials and probe molecules.³⁰

Finally, Solid-state NMR is a sensitive tool for real-time, quantitative 3D imaging of composition, atomic connectivity, interatomic distances, and electric field gradients under electrochemical conditions.^{36,37} Operando NMR has high spatial resolution within particles and is sensitive to local environment. Li et al. have shown specific crystallographic locations undergo ion insertion/extraction preferentially during early times.³⁷ NMR imaging is typically limited to 20–50 μm spatial resolution, but specialized pulse sequences can be used to achieve sub micrometer resolution.³⁸

The aforementioned experimental approaches have been developed to characterize ion insertion materials, each with their own advantages and disadvantages. The novel technique demonstrated in this thesis uses widefield electro-optical imaging to simultaneously measure ion insertion processes in many individual nanoparticles. This technique measures the electrochemical current response from all nanoparticles on a current collector (i.e., ensemble-level measurement) and the optical density changes due to ion insertion reactions at the single-nanoparticle level. The optical response is decoupled from the electrochemical current response. The single-particle-level imaging approach used here measures

electrochemical behavior of hundreds of single particles with diffraction-limited spatial resolution and millisecond time resolution. This approach can be generally applied to transition metal oxides³⁹, graphite^{33,40}, Ni(OH)₂ battery materials⁴¹, and MXenes⁴² whose optical properties change during ion insertion. Electro-optical imaging is nondestructive and measures properties under ambient radiation, temperature, and pressure conditions, which goes beyond competing in operando TEM and X-ray based methods. The limit of detection for particle size is about 13 nm for metal oxide nanoparticles (see 3.3.9 Limit of Detection), which goes beyond most NMR, FT-IR, and Raman studies.

One disadvantage of the proposed approach is the optical diffraction-limited spatial resolution compared to TEM and X-ray imaging approaches. Thus, correlated ex situ electron microscopy imaging is required to resolve small particles. This method also hinges on the material exhibiting electrochromic behavior. Electrochromism is defined as a material property where the system undergoes optical changes during faradaic electrochemical reactions. Additionally, the optical range of detection is limited by the detector which can narrow the types or number of optical changes that can be probed. While light scattering presents a serious challenge toward extending electro-optical imaging to nanoparticle films, though reconstruction algorithms could be applied to measure redox concentration profiles of nanoparticle film electrodes in 3D.⁴³ Like plasmonic-based imaging methods,²⁹ this electro-optical approach does not measure electrochemical current at the single-nanoparticle level. This apparent experimental limitation does not restrict the knowledge gained from the electro-optical imaging technique. Regardless of the electrochemical current flow into single nanoparticles that are deposited on the ITO electrode, Li-ion insertion single-nanoparticle level dynamics are still measured. Importantly, electro-optical imaging quantifies these processes for single particles that are attached to the same ITO electrode, immersed in the same electrolyte, and located only micrometers apart.

1.2 Hexagonal Tungsten Trioxide (h-WO₃) as a Model System

Current hypotheses predict three major traits that contribute to high-rate performance: (1) the material does not undergo a crystalline phase change, (2) the crystal should have an open, layered structure

that (3) have low energy binding sites for ions.⁷ Understanding the variation in ion insertion dynamics between individual crystalline particles that are nominally the same may reveal new materials chemistry that can help propel the field forward and is the aim of this thesis. Hexagonal tungsten trioxide (h-WO₃) is a good model system because it does not undergo a crystalline phase change during lithiation⁴⁴ or large volume expansion during lithiation,⁴⁵ minimizing the possibility that changes in bulk structure could complicate data interpretation. Not only would a phase change impact the identity of surface facets, but distinct crystalline phases also show different electrochromic properties⁴⁶⁻⁵⁰. Further, large hexagonal channels lead to better charge storage⁵¹⁻⁵³ and electrochromic behavior^{44,54}. Large optical modulation and large body of supporting literature make h-WO₃ an ideal and representative example to explore ion insertion in solids.

CHAPTER 2: BACKGROUND

This chapter serves to provide the necessary scientific background information for the electro-optical results presented in this thesis. The relationship between ion insertion induced optical changes will be discussed in terms of mechanism of optical absorption and how absorption is related to charge storage dynamics. Additionally, the use of the Beer-Lambert Law for electrochromic will be outlined.

2.1 Electrochromism

The electro-optical technique herein hinges on the use of electrochromic materials. A material is defined as electrochromic if it undergoes optical changes during faradaic electrochemical reactions. The general reaction scheme for ion-insertion based electrochromism in inorganic compounds is given in Equation 2-1 using WO_3 and Li^+ as a representative example.



Applying a cathodic potential induces a double injection of electrons and ions, reducing W^{6+} to W^{5+} with a charge balancing Li^+ yielding a deep blue “tungsten oxide bronze” (Li_xWO_3). The resulting bronze has different optical characteristics than the visibly transparent native oxide. In the case of WO_3 (and many electrochromic materials), the bronze undergoes broadband changes in the absorption spectrum sometimes resulting in a visible tint, with the largest changes in the IR.^{49,50,55} Anodic polarization of the electrode reversibly recovers the visibly transparent native oxide by oxidizing W^{5+} to W^{6+} and extracting Li^+ .

2.1.1 Electrochromic Mechanisms

The physical mechanism that causes optical changes in inorganic electrochromic materials is widely debated between (1) intervalence d-band electron transfer, (2) localized surface plasmon resonance (LSPR), (3) polaronic absorption, and (4) Drude-like free electron absorption.^{39,56-64} Generally, visible changes are attributed to intervalence effects, while polaronic and Drude-like absorption are responsible for low energy transitions; LSPR is highly tunable in both visible and NIR regions.^{39,49,50,58,64,65} The specific mechanism responsible for any given optical change can be material and size dependent.^{58,62,64-66} There

exists only a qualitative understanding on the electrochromic mechanisms in even the most widely studied electrochromic material, WO_3 , whose optical changes appear to be dependent on particle size and degree of crystallinity.^{56,57,62,67-69}

Intervalece transfer of electrons in transition metal d-orbitals lead to optical changes in many inorganic materials. For example, E_g - T_{2g} splitting in compounds or molecules composed of octahedra cause optical absorption across many wavelengths.⁷⁰ In many instances, the change in electronic structure is accompanied by a change in bond lengths, as with Jahn-Teller effects, which can further impact optical properties.⁷⁰ Intervalece electron transfer does not take into account effects from inserted ions (i.e. Li^+), and is usually used to describe the mechanism of electrochromism in materials that undergo optical transitions during oxidation, rather than ion insertion (i.e. NiO , V_2O_5 , etc.).^{58,60}

LSPR is a quantum confinement effect where incident radiation absorption causes oscillation of the electrons in a particle. Because confinement is highly dependent on material, size, and shape, the optical absorption from LSPR is highly tunable.^{50,71} Electrochromic particles absorb more light with increasing LSPR intensity as they gain electron density during ion insertion.⁵⁰ LSPR is not present for particles that are larger than their Bohr exciton radius (outside of the quantum confinement regime, usually ~ 3 nm).

Polaronic absorption and Drude-like free electron absorption are the two mechanisms of electrochromism usually used to describe optical changes in materials that change color during reduction (i.e. WO_3).⁶² Double injection of electrons and ions change the electronic structure of the host material. In the case where charge is sufficiently delocalized, photon absorption can cause the migration of charge from one reduced transition metal center to an adjacent transition metal, typically referred to as “small polaron hopping” which is contingent upon the polarizability of bonds in the solid.^{62,65} Drude-like free electron absorption is more localized than small polaron hopping and is most easily thought of as a special kind of intervalence transition present in metals⁷² and heavily doped semiconductors^{62,63} (like electrochromic bronzes). Rather than excitation of electrons in defined d-orbitals, electrons are excited to higher energy levels within the band structure of the material, typically through the absorption of low energy light.

Generally, small polaron hopping is thought to occur in only amorphous materials, and Drude-like free electron absorption is thought to occur only in crystalline materials,^{56,57,59,62} though both mechanisms are likely at play in varying degrees during ion insertion. Neither small polaron hopping or the Drude model fully explain the need for a charge balancing ion despite experimental evidence showing its necessity.⁶²

2.2 Beer-Lambert Law for Electrochromics

Fundamentally useful knowledge can be gained from electrochromic materials during ion insertion despite the incomplete understanding of the foundational mechanisms responsible for color change. The electro-optical technique presented herein can still be used to investigate the charge storage dynamics even if the mechanism is not rigorously understood if there is a clear relationship between the amount of charge stored (number of ions inserted) and degree of coloration (how much light is absorbed). The Beer-Lambert Law describes one such relationship,⁷³ and this section will be dedicated to describing its application in the realm of electrochromic materials.

The Beer-Lambert Law (Equation 2-2) describes a linear relationship between the optical density (OD) of a species and the concentration of absorbing species (c) where ϵ is the molar extinction coefficient and d is the thickness of the material.

$$OD = \epsilon cd \quad \text{Equation 2-2}$$

The time dependent OD change ($\Delta OD(t)$) of a material during the electrochromic reaction in Equation 2-1 is calculated according to Equation 2-3 for a transmission experiment.

$$\Delta OD(t) = OD(t) - OD(0) = \left(-\log_{10} \left(\frac{I(t)}{I_0(t)} \right) + \log_{10} \left(\frac{I(0)}{I_0(0)} \right) \right) \quad \text{Equation 2-3}$$

where I is the light transmitted through the electrochromic material, I_0 is the light transmitted through the background (this includes light attenuation from the substrate, electrolyte, etc.). Importantly, the change in concentration of absorbing species (Δc) is directly related to ΔOD if the thickness of the electrochromic film or individual particle is known (Equation 2-4).

$$\Delta OD/d = \epsilon \Delta c$$

Equation 2-4

Equation 2-4 implies that the concentration of ions in a solid, and therefore the faradic charge stored, can be directly calculated from an optical measurement if the constants ϵ and d are known. For the case presented in Equation 2-1, the real-time dynamics of charge storage can be probed by calculating the concentration of $[\text{Li}^+ - \text{W}^{5+}]$ color centers in Li_xWO_3 in an in operando transmission experiment.

There are four major assumptions that must be made for the Beer-Lambert law to be used quantitatively for single particle electrochromic materials: (1) ϵ is an intrinsic material property that is particle independent, (2) the magnitude of light lost to scattering is ion insertion independent, (3) every injected electron is compensated by a cation, and (4) the measurement is made in a regime where OD responds linearly with concentration of absorbing species. Assumption (1) is justified by considering that ϵ is a material property that should not differ for particles that are nominally the same. Assumption (2) can be considered a limitation for the application of the Beer-Lambert Law for electrochromics. Scattering is largely influenced by changes in volume or size which occur for many charge storage materials (e.g. Si) during the ion insertion reaction. However, scattering is not a limitation if a material is chosen that does not undergo morphology change during charge storage. Assumption (3) follows from Equation 2-1 where the reduction of the electrochromic species occurs by a double injection of electrons and charge compensating cations. That is, the number of reduced sites is equivalent to the number of cations stored in the material. Assumption (4) places another fundamental limitation for the application of the Beer-Lambert Law for electrochromic materials. Many charge storage materials undergo crystalline phase changes during ion insertion which limit the degree of ion insertion where the optical change is linear with concentration. Additionally, high values of ion insertion lead to non linear changes in OD because the material becomes so dark that modern detectors for transmission experiments fail to detect the small amounts of light that are not absorbed. Therefore, only certain values of x in Equation 2-1 can be probed through optical measurements.

2.3 A Note on Electrochromic Smart Windows

Electrochromic properties of electrochemical charge storage materials are not widely discussed within the field of energy storage. As a consequence, monitoring charge storage dynamics through color change at the single particle level is not a common practice. However, there is a separate body of work focusing on producing devices that take advantage of optical changes during ion insertion. Of those devices, “smart windows” hold the largest promise for future energy savings and are an active area of research across the world. Smart windows reduce ventilation and cooling system energy consumption by modulating the amount of IR radiation from the sun into buildings.^{50,55,62,74} The smart window absorbs IR radiation in the “charged” (colored) state but does not in the “discharged” (transparent) state (**Figure 2.1**).

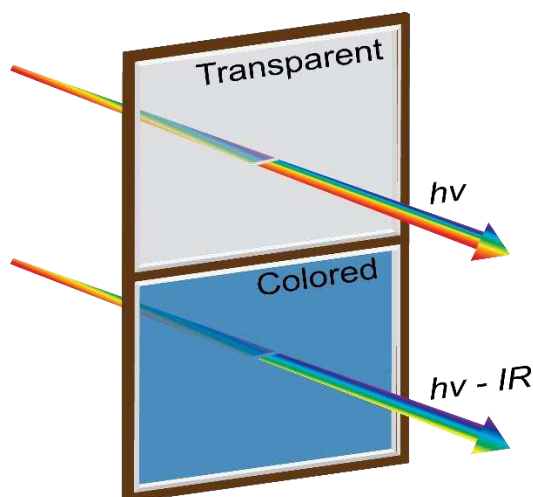


Figure 2.1 – Smart window. Electrochromic smart windows absorb IR radiation in the colored state, but do not in the transparent state.

The single particle electro-optical approach herein is established in terms of electrochromic smart windows to validate its use to monitor ion insertion dynamics in charge storage materials. Terms like “tinting magnitude” or “tinting speed” relate to total charge stored and the kinetics of the storage reaction, respectively. These studies described here work to establish a bridge between the electrochromic and energy storage literature in the hopes of advancing technologies more rapidly.

CHAPTER 3: EXPERIMENTAL DESIGNⁱ

The single particle electro-optical technique pioneered over the last few years can be generally applied to many charge storage systems to gain fundamental materials chemistry insight. This chapter aims to lay the foundations for the electro-optical experimental design used to probe the Li-ion insertion dynamics in a model system, hexagonal tungsten oxide (h-WO₃). A detailed synthesis and characterization routine for h-WO₃ is given first, followed by an outline of the experimental procedure. Finally, the bulk of this chapter will deal with the detailed nuance of the procedure and walk the reader through each step necessary to use the electro-optical technique.

3.1 Material Synthesis

Hexagonal tungsten oxide nanorods were synthesized via a hydrothermal reaction using 0.288 g NaCl (Sigma) and 0.853 g sodium tungstate dihydrate (Sigma). Precursors were dissolved in 19 mL of 18.2 MΩ-cm (MilliPore NanoPure) water following Wang et al.⁴⁶ The pH was adjusted to 2.0 using ~3 M HCl in 50 μL increments under continuous stirring (>300 rpm) and then transferred to a 23 mL Parr Instruments Acid Digestion hydrothermal reactor (model number 4979). The hydrothermal reactor was placed in an oven at 180 °C for 24 hours. The vessel was removed from the oven and allowed to cool to room temperature in a fume hood. The solid white product was filtered and washed twice with 18.2 MΩ-cm water by centrifugation and suspended in reagent grade ethanol (Fisher Scientific); particles aggregated in 200 proof ethanol. The sample remains structurally stable in ethanol for greater than one year by PXRD (not shown). The synthesis procedure is summarized as a two-step process in **Figure 3.1** below. Justifying the crystal structure and particle morphology shown in **Figure 3.1** will be the subject of section 3.2 Characterization.

ⁱ This chapter contains adaptations from Evans, R. C.; Nilsson, Z. N.; Sambur, J. B. High-Throughput Single-Nanoparticle-Level Imaging of Electrochemical Ion Insertion Reactions. *Anal. Chem.* **2019**, *91*, 14983–14991. <https://doi.org/10.1021/acs.analchem.9b03487>. citation⁽⁷⁵⁾. R.C.E. performed experiments, analyzed data, and wrote the manuscript. Z.N.N. performed SEM imaging experiments. J.B.S. and R.C.E. developed the experimental setup, analyzed data, and wrote the manuscript.

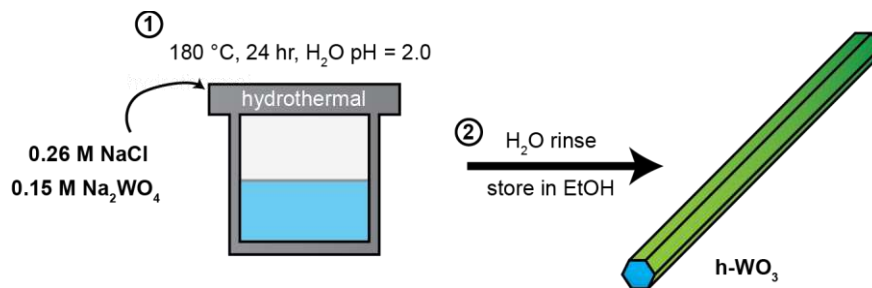


Figure 3.1 – Schematic representing the two-step process for making hexagonal WO_3 nano rods. 1) add precursors and use correct temperature, pH, and solvent. 2) clean and store nanorods.

3.2 Characterization

Several techniques were used to confirm the hexagonal crystal structure and particle morphology. In this section I will specifically discuss powder x-ray diffraction (PXRD), scanning electron microscopy (SEM), transmission electron microscopy (TEM), and atomic force microscopy (AFM). Gaining deep insights into ion insertion in solids relies on understanding how the atoms are arranged in the host; different crystal systems impact redox reactions and impact data interpretation.^{51–53,76,77} Further, quantitative comparison of optical performance between single nanoparticles and the kinetic modeling used to fit that data in 4.1 Kinetic Model rely on knowing the exact particle shape and thickness.

3.2.1 PXRD

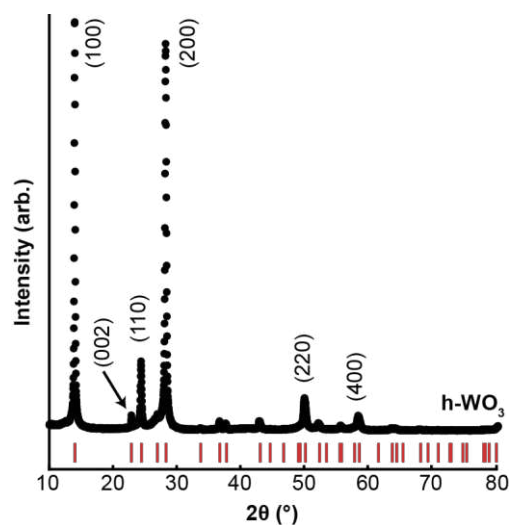


Figure 3.2 – PXRD structural characterization for WO_3 nanorods. Black circles represent data points and red lines represent the P6/mmm, JCPDS 00-033-1387 reference.

The Bruker D8 Discover series II instrument with Cu K α radiation was used to acquire PXRD patterns. The sample was rotated, and a knife edge was used to minimize background signal at low angles. Data was acquired at 0.2 s or longer. Samples were drop cast out of reagent ethanol onto Si pucks (MTI G190901). **Figure 3.2** shows the PXRD pattern for the h-WO₃ sample used for a majority of the work presented in this thesis. The pattern matched well with the P6/mmm, JCPDS 00-033-1387 reference, indicating a hexagonal crystal structure. The intensity of peaks in PXRD correspond to the constructive interference of diffracted x-rays inside the crystal structure. A high intensity peak indicates a large presence of a particular lattice plane (with a particular lattice spacing) relative to the orientation of the detector. The large signal for {100} and small signal for {001} groups of planes in the PXRD indicate preferred growth direction along the [001] crystallographic direction.⁷⁸ TEM imaging was used to confirm growth direction and will be discussed next.

3.2.2 TEM

The morphology and crystal growth direction were determined by TEM imaging. **Figure 3.3a** shows the rodlike morphology of the nanoparticles while **Figure 3.3b,inset** shows a closer image of a nanorod and a representative selected area diffraction pattern indicating a regular atomic spacing of 3.83 Å and therefore growth along the [001] direction.⁴⁶ Particles appear as dark objects against a brighter background because the atoms in the crystal block/scatter electrons before they transmit through to the detector. TEM was done on a JEOL JEM-2100F instrument at 8keV. Samples were drop cast out of reagent ethanol on to copper / carbon mesh grids (Ted Pella 0184-F) for TEM imaging.

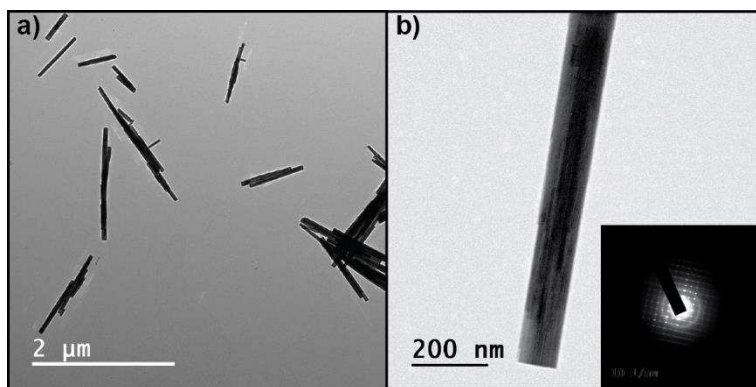


Figure 3.3 – Crystallographic characterization of $h\text{-WO}_3$. a) TEM image showing the rod-like morphology of the nanoparticles. b) High resolution TEM image showing a nanorod with regular atomic spacing. Inset is a selected area diffraction pattern for the nanorod showing a regular atomic spacing of 3.83 Å.

3.2.3 SEM and AFM

A combination of SEM and AFM was used to fully probe particle shape. While TEM provides atomic level detail, it does so from a birds-eye view. The edges of the particles appear as straight lines; no detail on the shape of end caps is easily obtained. However, by preparing films with various degrees of disorder/random particle stacking it is possible to image particle end caps in SEM. SEM samples were prepared by making a ~ 3 mg/mL solution of nanoparticles and drop casting onto ITO out of ethanol. A known weight of particles were obtained by (1) weighing a centrifuge tube before and (2) after spinning at 3000 rpm for 5 min and drying the particles at 80 C for 30 min. The difference in weight gives the mass of nanoparticles. Resuspending the nanoparticles with a known volume of ethanol yields a known mg / mL solution.

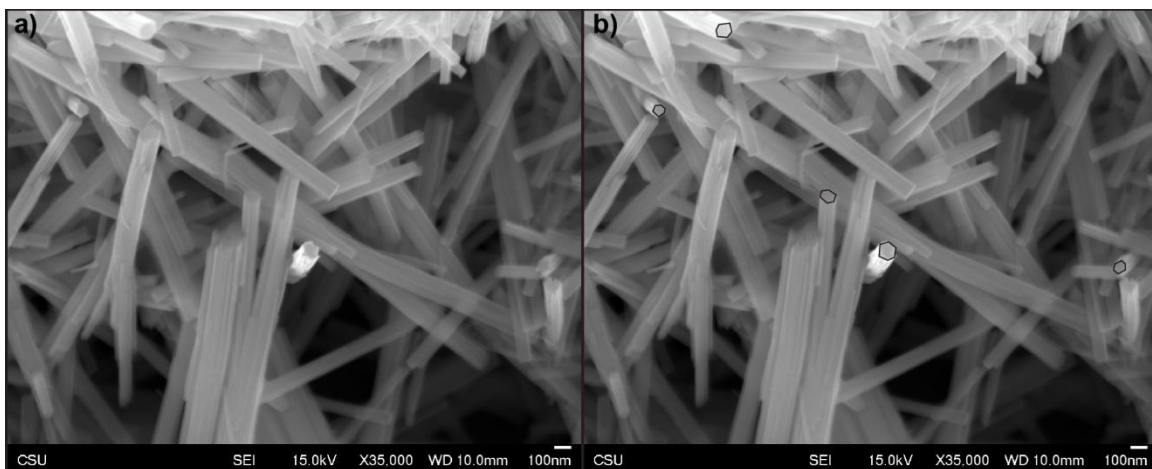


Figure 3.4 – SEM images of nanorods. a) An SEM image showing the different morphologies of nanorods. b) The same SEM image as in (a), but with the hexagonal capped nanorods pointing at the detector highlighted with black outlines.

Figure 3.4a shows an SEM image of h-WO₃ nanorods in various orientations. Random / disordered films like this were prepared by drop casting ~3 mg of sample out of ethanol and rapidly evaporating the ethanol using warm air. These disordered films expose the endcaps of nanorods. **Figure 3.4b** shows the same SEM image as in **Figure 3.4a** with the capped nanorods pointing at the detector outlined in black and are roughly hexagonal, implying a hexagonal prism morphology.

SEM was done on a JEOL 6500 FE-SEM instrument at accelerating voltages of either 8 keV for single particles or 15 keV for films. A lower accelerating voltage was used for single particle studies to better visualize surface details and more easily tell singles apart from pairs or clusters of nanoparticles.

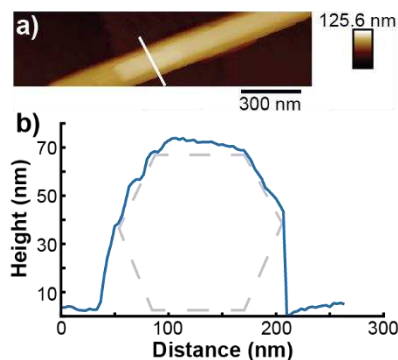


Figure 3.5 – Atomic force microscopy (AFM) of a hexagonal nanorod. a) AFM image of a nanorod. The white line indicates where the line profile was drawn to obtain (b). b) The height profile obtained from the white line drawn in (a). The gray dashed lines illustrate how the high profile can originate from a particle with a hexagonal prism morphology.

AFM was used as an additional technique to verify the hexagonal prism particle morphology.

Figure 3.5a shows a representative AFM image of a h-WO₃ nanorod. **Figure 3.5b** shows the height profile with two sloping edges on either side of a relatively flat plateau which can be thought of as representing a hexagonal prism (illustrated with gray dashed lines). The AFM measurements were performed at 1 Hz scan rate in the Scanasyt mode using a Bruker SCANASYST-AIR cantilever (silicon nitride with tip radius of 2 nm). AFM image analysis was performed using NanoScope Analysis software (version 1.8).

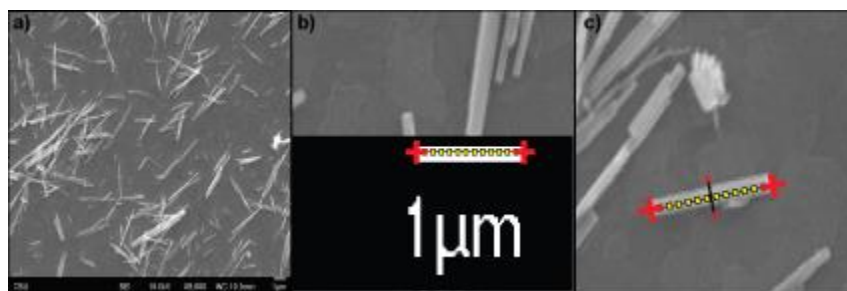


Figure 3.6 – Determine particle length and width from SEM. a) Representative SEM image. b) Length of scale bar determined by user clicks (red cross) cut in from (a). c) Length and width of nanorods selected by user clicks (red cross).

The average nanoparticle length and width were $1.02 \pm 0.54 \mu\text{m}$ and $0.10 \pm 0.04 \mu\text{m}$, respectively.

Particle sizes were measured by analyzing the major and minor axis lengths (which correspond to length and width for these nanorods) from SEM images. A custom MATLAB code computed the mean the

standard deviation of 258 particles from images like that shown in **Figure 3.6a**. The code works by first determining the number of pixels in a known length (the image scale bar) from user indicated clicks denoted with red crosses (**Figure 3.6b**). Next, the user clicks each edge of the nanorod along its length (major axis) and then again along its width (minor axis) as in **Figure 3.6c**. This is repeated for all particles whose boundaries can be determined for as many images as necessary. The output of the code is a column of major axis lengths and a column of minor axis lengths. The mean and standard deviation are computed using the built-in `mean` and `std` functions in MATLAB.

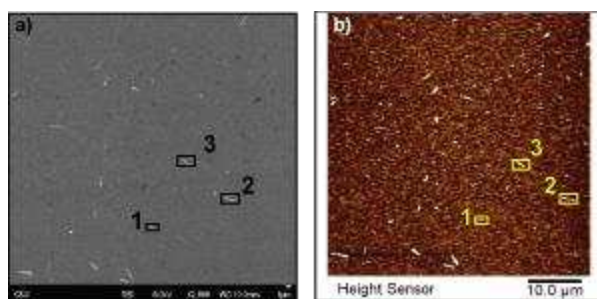


Figure 3.7 – Correlated SEM and AFM. a) SEM image with 3 individual nanorods marked. b) AFM image with the same individual nanorods marked.

Note that correlated SEM and AFM reveal particle widths and heights closely approximate each other. The widths for objects 1, 2, and 3 are 138 nm, 138 nm, and 105 nm, respectively from SEM (**Figure 3.7a**). The height from AFM for the same objects was 129 nm, 131 nm, and 111 nm, respectively (**Figure 3.7b**). These measurements are no more than 7% different, showing that the assumption is valid and is integral to the kinetic model and fitting procedure given in 4.1 Kinetic Model.

3.2.4 Characterization Summary

Hexagonal tungsten oxide was hydrothermally synthesized with NaCl and sodium tungstate dihydrate in acidic media. The hexagonal crystal structure was determined with PXRD and matched with the P6/mmm, JCPDS 00-033-1387. Growth direction was confirmed to be in the [001] direction by TEM. Particle morphology is determined to be a hexagonal prism by SEM and AFM. SEM revealed nanoparticle lengths and widths were $1.02 \pm 0.54 \mu\text{m}$ and $0.10 \pm 0.04 \mu\text{m}$, respectively.

3.3 Experimental Design

3.3.1 Overview

The purpose of this section is to give a broad overview of the electro-optical technique before diving into the detailed nuance of each of its components and outputs. A simple, but representative, example is used to introduce the imaging apparatus followed by the key outputs. The following sections will describe how custom parts are made, the choice of specific equipment and parameters, and image processing steps that lead to spatially resolved optical measurements during electrochemistry that generally relate to all chapters of this thesis. Highly specific image processing will be reserved for the appropriate chapter and section.

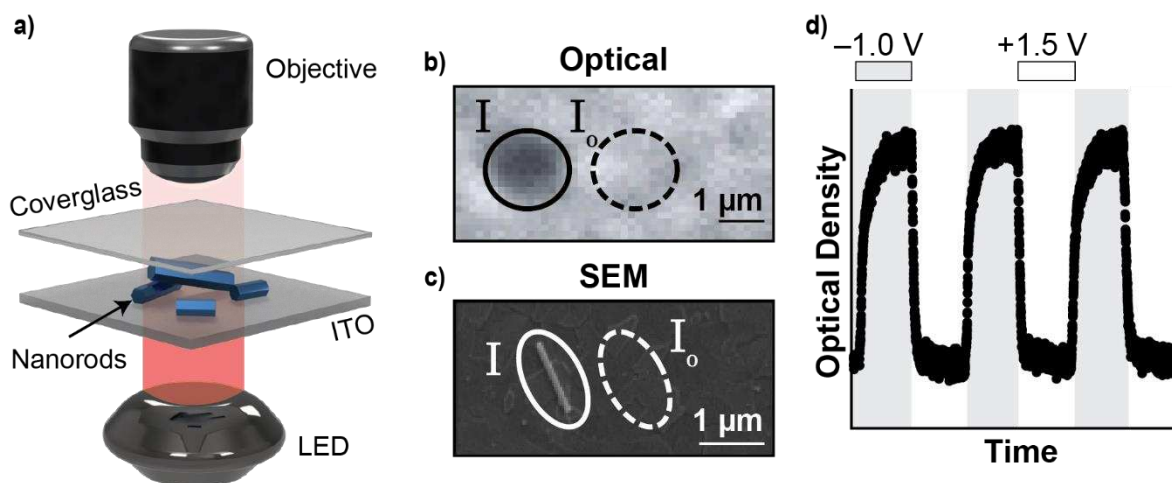


Figure 3.8 – Electro-optical overview a) An optically transparent electrochemical cell is mounted on a microscope and an LED or lamp illuminates the sample. The light transmitted through the sample is collected by a microscope objective and imaged on an EM-CCD camera (not shown). b) optical image of an object. c) SEM image correlated with the optical image in (b) of the same object. d) Representative potential dependent optical density changes with time.

Figure 3.8 shows an overview for the electro-optical imaging technique and output. An electrochemical cell containing nanorods is mounted in between an illumination source and microscope objective (**Figure 3.8a**). The light transmitting through the sample to the detector results in an optical image (**Figure 3.8b**). Nanorods appear as dark objects on a bright background because the nanorods absorb and scatter more light than the substrate. The pixels that compose the nanorods are signal I , and an equal area

of pixels composed of only the substrate is the incident light signal I_0 . The objects found in optical images are found again in the SEM to ensure the number of singles is known (single particles vs clusters of particles) (**Figure 3.8c**). As described in Equation 2-3, signals I and I_0 are used to determine optical density. **Figure 3.8d** shows a representative example of potential dependent optical density changes with time that could result from a nanoparticle like that shown in **Figure 3.8b,c**. Optical density increases as the amount of Li^+ injected into the h-WO_3 increases, and decreases as Li^+ is extracted. Cathodic and anodic potentials of -1.0 V and 1.5 V vs Ag/AgCl are used in this example (**Figure 3.8c**). These optical density changes form the basis for the investigation of Li-ion dynamics in WO_3 described throughout this thesis.

3.3.2 Choosing A Light Source

Choosing a light source, while sounding superficially trivial, is an important aspect of the electro-optical technique. The wavelength chosen will determine the type of chemistry or physical processes probed for any given system. Some processes happen over many wavelengths due to broad band changes in the material, as is the case for h-WO_3 . In these cases, the quantum efficiency of the detector must be considered to maximize signal-to-noise.

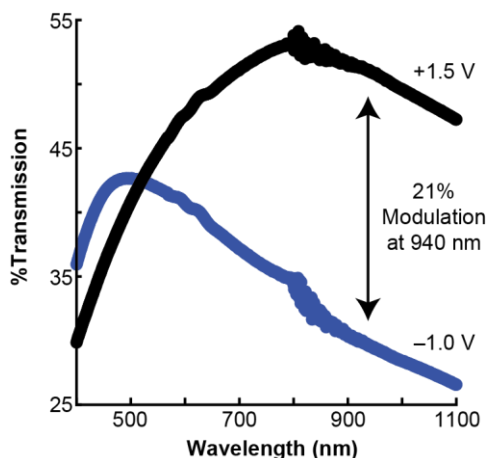


Figure 3.9 – Transmission spectra of h-WO_3 on ITO under electrochemical bias. The film is in the colored/tinted state at -1.0 V and bleached/transparent at 1.5 V vs Ag/AgCl . Optical modulation increases with increasing wavelength.

Figure 3.9 shows the percent transmission spectra for h-WO₃ on ITO in the visible and NIR regions under electrochemical bias. The film was colored (-1.0 V) or bleached (1.5 V) in 1 M LiClO₄ for 1 minute. The film shows a shift and increase in transmission below 500 nm, but a broad band decrease in transmission above ~550 nm. The percent modulation (difference in bleach and color spectra) increases with increasing wavelength. Spectra were taken on a Cary 5000 UV-Vis-NIR spectrometer with a diffuse reflectance accessory. A 940 nm LED light source (Thor Labs) was chosen because it is roughly the wavelength of maximum optical modulation and is compatible with both available detectors (Andor iXon EMCCD and Prime 95b CMOS cameras).

3.3.3 Electrochemical Flow Cell

The electrochemical flow cell is a key component of the electro-optical experimental design. It allows the user to image materials surrounded by electrolyte during electrochemical processes for many experiments over several months if constructed properly. However, the design for the electrochemical flow cell used is complex and takes several days to build. While several new designs have been tested, and improving the flow cell is an active effort in the Sambur lab, at the time of writing the design presented in this section is the version used for all experiments presented in chapters 4-6.

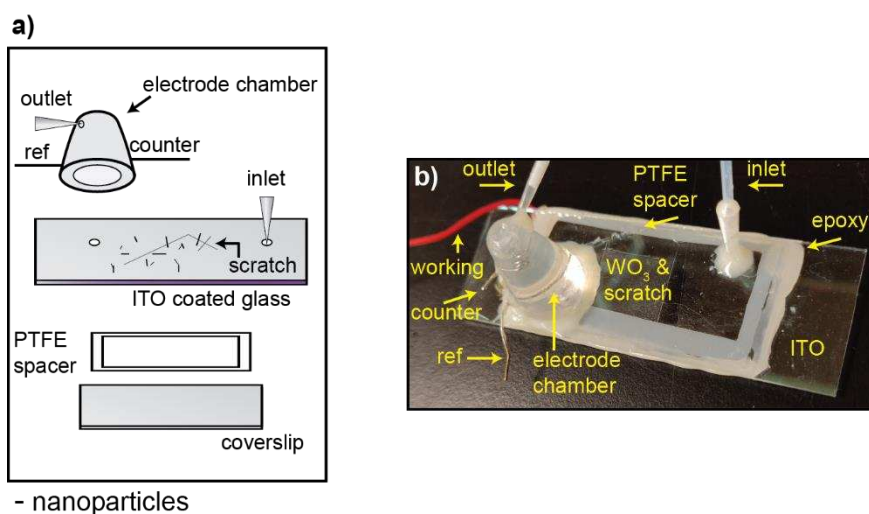


Figure 3.10 – Electrochemical flow cell. a) Cartoon of the electrochemical flow cell with all necessary components labeled. b) photograph of the electrochemical flow cell with all necessary components labeled.

Figure 3.10a shows a break-out view cartoon for the construction of a complete electrochemical flow cell with all necessary components labeled. Each part of the flow cell required its own preparation before construction of the flow cell begins. Specific materials were chosen due to their chemical resistance to propylene carbonate, the supporting solvent for the 1 M LiClO₄ electrolyte used in all studies. First, the ITO coated glass microscope slides (4-10 Ω, 25 × 75 × 1.1 mm, Delta Technologies) were gently placed on a wooden block with the ITO side facing down. Two holes are drilled 35 mm to 40 mm apart using a diamond coated Dremel drill bit. One hole serves as a location for the inlet for injection of electrolyte while the other serves as an exit for that electrolyte into the electrode chamber. Next, a diamond tip pen was used to scratch an asymmetric shape on the ITO side of the microscope slide. This scratch serves as an important landmark for correlated optical and SEM imaging discussed in 3.3.5 Optical / SEM image correlation. The drilled ITO slides were cleaned by sonicating the substrates for 10 minutes each in several solutions: Liquinox soap, 18.2 MΩ-cm water, reagent acetone, reagent ethanol, 1M KOH, and 18.2 MΩ-cm water once more. The clean ITO slides were then soaked in a 17:3:1 18.2 MΩ-cm water: concentrated ammonium hydroxide: 30% hydrogen peroxide solution to make the ITO surface more hydrophilic,⁷⁹ which provided better wettability of the nanoparticle solution to the substrate during spin coating deposition of nanoparticles. Spin coating was done with ~0.1 mg/ml solutions of WO₃ nanorods in ethanol at 3000 rpm (VTC-100 vacuum spin coater) onto the ITO electrode. Note that the WO₃ nanorod solution concentration was varied to reach the desired dilute nanorod surface coverage. The surface was quickly surveyed using reflection microscope at 100× magnification to ensure nanoparticles were on the ITO surface. Next, a 25 mm by 40 mm rectangle polytetrafluorethylene (PTFE) sheet was cut from a large roll using a razorblade and straight edge. An interior window of 20 mm by 35 mm was cut out so that the PTFE would only serve as a spacer between the ITO and coverslip. The nanoparticle-coated ITO working electrode was assembled into the base of the electrochemical flow cell by sandwiching a 50 micron-thick PTFE spacer between the glass coverslip (No.1 Thermo Fisher) and the ITO substrate. The coverslip was permanently held to the

ITO slide using the chemically resistant Loctite E-120HP Hysol epoxy. At this point the cell is left to dry for one day.

Next the electrode chamber was prepared using polypropylene plastic (obtained by sawing the end off a 15 mL centrifuge tube). Three vertical holes are drilled in the electrode chamber: one for the reference (ref) electrode, one for the counter electrode, and one for the electrolyte outlet. A 2 cm – 3 cm section of platinum wire is cut using ceramic scissors and curled to fit into the electrode chamber. Curling the wire increase the surface area of the electrode that can fit in the small chamber. A Ag/AgCl wire is placed in another hole in the electrode chamber. The outlet is fashioned from a plastic pipet tip and is placed in the top-most hole in the electrode chamber. All components are sealed in place using Loctite E-120HP Hysol epoxy and allowed one day to dry. The electrode chamber is placed over the outlet hole of the drilled ITO electrode while a plastic pipet is fashioned into the inlet hole using Loctite E-120HP Hysol epoxy and allowed one day to dry.

Finally, PTFE tubing (Cole Parmer) is placed in both the inlet and outlet pipet tips and sealed using Loctite E-120HP Hysol epoxy and allowed one day to dry. A 10 cm section of insulated copper wire was cut from a spool (Conwire); 1 cm of insulation was stripped from both ends. One end of the wire is secured to the ITO surface using conductive epoxy (MG Chemicals) and serves as a working electrode contact. Once all epoxy is dry, the flow cell was checked for leaks using a syringe pump (Genie). Any leaks are sealed with Loctite E-120HP Hysol epoxy and allowed to dry for one day before any electro-optical experiments were performed. **Figure 3.10b** shows a photograph of a complete electrochemical flow cell.

3.3.4 Experimental Set Up

The electro-optical experimental design relies on many disparate components working together harmoniously. Electro-optical gets its name from the use of optical microscopy in combination with electrochemical techniques. In this case, bright field transmission microscopy was combined with either chronoamperometry or cyclic voltammetry to probe spatially resolved ion insertion dynamics at a particular

wavelength. General operating circumstances are discussed in this section. First, the layout of the equipment is given with attention on which instruments must be connected to one another (and what settings to keep in mind). How images are acquired and saved is discussed second.

Figure 3.11 shows a cartoon block diagram for electro-optical imaging. To begin, the appropriate objectives (20× (Olympus UPlanFL N), and 60× objective, Olympus UPLANSAPO60x/W) are fixed to the nose piece of an Olympus IX73 inverted optical microscope. Next, the completed (and leak-free) electrochemical cell is placed on the microscope stage. Two light sources are needed in this case: a white light lamp, and the 940 nm LED. The white light lamp is installed first to position the flow cell and focus on the particles because the human eye cannot detect 940 nm light. Leads from the potentiostat are connected to the electrochemical flow cell in a 3-electrode fashion – the counter electrode is platinum wire, the reference is Ag/AgCl, and the working is the wire attached to the ITO electrode (see 3.3.3 Electrochemical Flow Cell). The analog signals for current (i) and potential (E) are connected to separate analog channels in a data acquisition card (DAQ) via BNC cables. The camera shutter signal from the EMCCD or CMOS is connected to the digital signal port in the DAQ. The function of the DAQ card is to record the outputs from separate devices and place them on a shared time axis. Thus, current, potential, and camera activity are all known at each point in time which is requisite to the success of the electro-optical imaging technique (see 3.3.6 Image Processing).

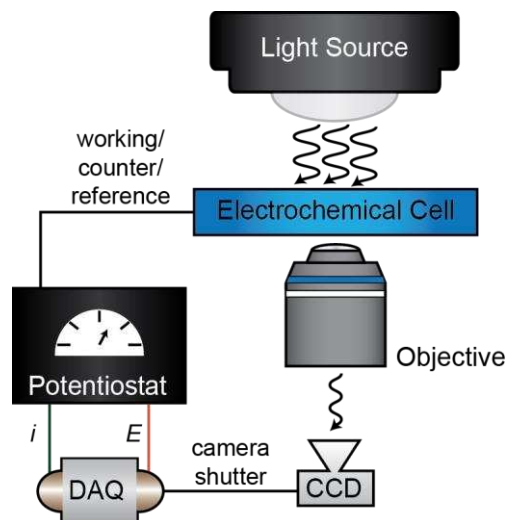


Figure 3.11 – Cartoon overview of the electro-optical microscope set up. An optically transparent 3-electrode electrochemical cell is mounted on an inverted microscope and an LED or lamp illuminates the sample from above. The light transmitted through the sample is collected by a microscope objective and imaged on an EM-CCD camera. The CCD camera and potentiostat are connected to a data acquisition card (DAQ).

The sample is brought into focus by slowly raising the nose piece and objective toward the sample under 20× magnification under white light illumination. The macroscopic scratch etched onto the ITO provides a useful target to obtain course focus. At this point, the iris on the diaphragm between the light source and sample is adjusted to the minimum size. Kohler illumination is achieved by adjusting the position of the diaphragm until the blades of the iris appear sharp and in focus. This process insures an even illumination of the sample. Note that Kohler illumination is wavelength dependent, so switching from a white light source to 940 nm does induce some unevenness, but because the human eye cannot detect 940 nm light and the smallest iris size is still too large for detection on the camera, this is the best way get close to Kohler illumination. Next, the 60× objective is used to locate areas where particle coverage is high, but objects are spatially separated. A 2× lens is placed between the objective and camera to achieve 120× magnification.

The light transmitted through the sample and collected by the objective is directed to the camera by a series of mirrors. MircoManager 1.4 software is used to control the acquisition settings for the camera. Once the image is in focus on the camera, the white light is swapped for the 940 nm LED and an appropriate

imaging rate is chosen. The DAQ card should sample 5× - 10× faster than the imaging rate to minimize the risk of under sampling. Electrochromic reactions, like that given in Equation 2-1, occur on the time scale of seconds so 5 – 10 fps is adequate in most cases. To ensure the complete collection of all data, the experiment should be executed in the following order: 1) begin recording with the DAQ card 2) begin image acquisition into the appropriate folder 3) start the appropriate electrochemical experiment file (e.g. chronoamperometry or cyclic voltammetry). This process is repeated for as many distinct areas around the macroscopic scratch that is necessary to obtain a data set with enough single particles.

3.3.5 Optical / SEM image correlation

High resolution images of individual nanoparticles are needed to correlate structural properties to optical changes, and therefore ion dynamics. The diffraction limit for optical microscopy roughly follows the below Equation 3-1⁸⁰:

$$l = \frac{\lambda}{2nNA} \quad \text{Equation 3-1}$$

Where l is the resolvable feature size, n , is the refractive index, and NA is the numerical aperture of the objective lens. Thus, $l = 280$ nm with 940 nm light in propylene carbonate with a NA = 1.2 (for the 60× objective) under ideal conditions. With an average particle width of 100 nm (3.2 Characterization) and increased scattering introduced at longer wavelengths, an alternative imaging method is needed to identify which objects from electro-optical imaging are single nanoparticle. Correlating optical images with SEM images allows for the identification of single nanoparticles, their length and width, and the number of nanoparticles in small clusters.

Obtaining optical images near a macroscopic scratch is pertinent. The scratch acts as a landmark in the SEM so the same area and particles can be found. **Figure 3.12** shows correlated optical and SEM images on the 10s of microns, and micron scale. **Figure 3.12a** shows an optical image of a scratch on an ITO surface at 20× magnification. The red dashed box indicates the area shown in **Figure 3.12b**. Areas near the intersection of the scratch were used for electro-optical experiments due to the ease of finding this shape in

the SEM. **Figure 3.12**c,d show one such area using 940 nm light and SEM, respectively. The shape and arrangement of objects in the optical image help identify the same areas in SEM. Single particles (**Figure 3.12**c-e, red oval) and small clusters of particles can easily be differentiated at this stage. Additionally, accurate measurements of single nanorod length and width (and consequently height, see 3.2.3 SEM and AFM) are known and serve as the basis for correlating structure to optical performance.

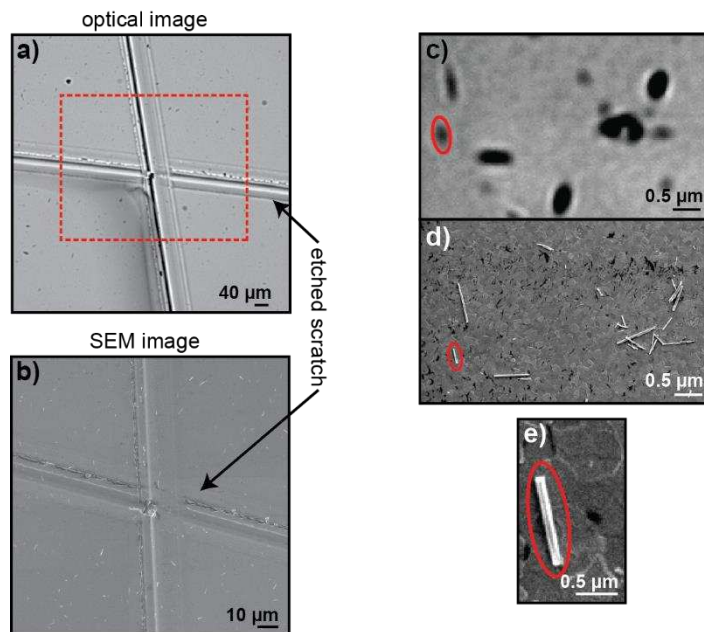


Figure 3.12 – Optical and SEM correlation and identification of single nanorods. a) optical image of the scratch area. b) SEM image of the same area as indicated in (a) by the red dashed square. c) optical image of h-WO₃ nanorods. d) corresponding SEM image of the same particles. e) identification of a single nanorod. (c-e) red ovals indicate the same object.

3.3.6 Image Processing

The electro-optical technique outputs only a file full of individual images and a DAQ spread sheet with time, potential, current, and camera trigger signal (TTL). Gaining information from raw data requires extensive data and image processing. This section will present the major steps performed in the custom MATLAB code to go from raw data to visualization of ion insertion dynamics.

It is imperative to know the time, potential, and current for each image. The DAQ data samples much faster than the imaging rate of the camera and therefore has a higher resolution of time. So, first, each

image must be assigned a time point. **Figure 3.13a** shows the square wave camera TTL signal with time. The shutter of the camera is either open (1) while the detector is exposing for an image, or closed (0) and no light is hitting the detector. **Figure 3.13b** shows the derivative signal of the camera shutter TTL signal. The “on” and “off” points for camera exposure are determined by finding the index in the data that corresponds to the inflection points in the derivative and comparing it to the time of that index (**Figure 3.13c**, blue lines). Each inflection point is determined by using the `find` function in MATLAB. The time point of the image is defined as the midpoint of the exposure, between the on and off points (**Figure 3.13c**, red diamond).

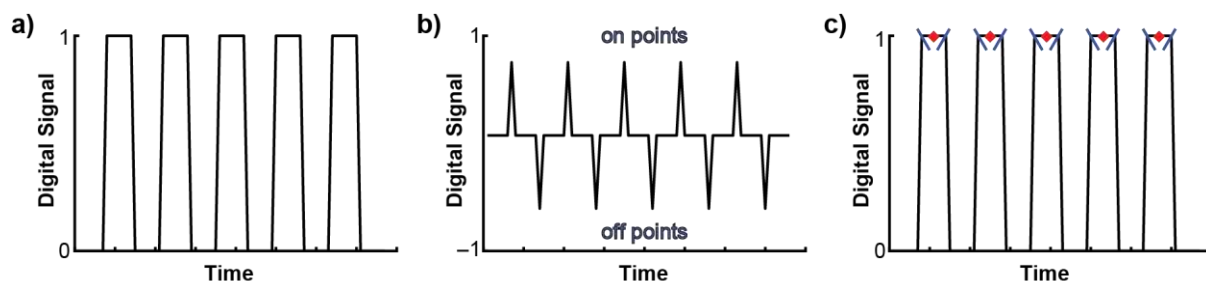


Figure 3.13 – Assigning time to camera TTL signal. a) Digital camera shutter TTL signal. b) Derivative of digital camera shutter TTL signal in (a). c) Digital camera shutter TTL signal with blue lines marking “on” and “off” points for camera exposure.

Potential and current can be assigned to any stack of images once the frames have been assigned a time. **Figure 3.14** shows a stack of images taken at various time points during an electro-optical experiment. The top of **Figure 3.14b** shows the corresponding camera shutter signal with a red diamond depicting the time defined for that image. These red diamonds are shown in the potential and current traces to illustrate how those values can be assigned to a particular image when they share the same time axis. In this example for the four images in **Figure 3.14a**, it is known that the first image was taken during a color pulse of -1.0 V and the latter three during a bleach pulse of 1.5 V, and what the global current was for the electrochemical flow cell.

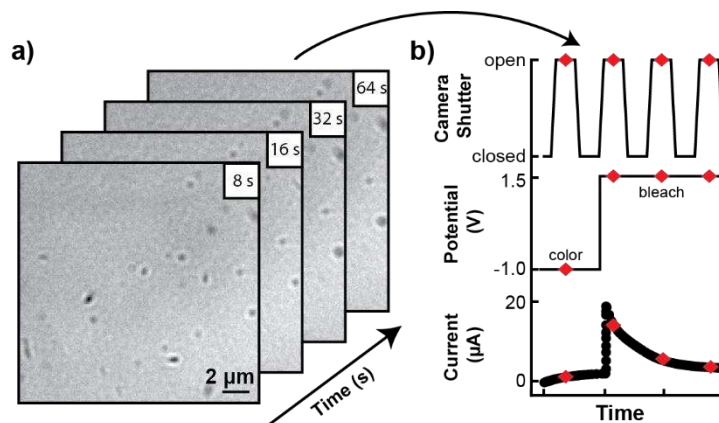


Figure 3.14 – Image processing to assign potential and current. a) Representative transmission image stack during a cathodic polarization pulse. b) Camera shutter and potentiostat signals measured by the DAQ. Top: camera shutter, middle: applied potential, bottom: electrochemical current. The red symbols represent the camera shutter open time points.

Change in pixel intensity relative to the background inform on ion insertion dynamics for each nanoparticle / object in a series of optical images. Accurately evaluating the correct pixels is therefore important. There are many strategies to define the boundaries for objects in an optical image; a series of image averaging, subtracting, and thresholding are used here. **Figure 3.15** shows the process used to obtain a binary image for determining object boundaries. First, all images from the lithiation/coloring step and delithiation/bleaching step are respectively averaged by summing all pixel values and dividing by the number of images summed. The result is two images, one that represents pixel intensities on average during lithiation (**Figure 3.15a**) and one during delithiation (**Figure 3.15b**). Subtracting the delithiated image from the lithiated image results in a difference image (**Figure 3.15c**) where all particles that absorbed light to become colored during lithiation appear as dark objects against a flat grey background. A gaussian is fit to pixel values for the background and a threshold is set at six times the standard deviation for the fit (6σ). **Figure 3.15d** shows the binary image that results from the thresholding process; white pixels represent particles whose difference image values were less than 6σ of the background values. Outer edges for each object in **Figure 3.15d** are used as boundaries for the next step in image processing: assigning masks. Note that only particles that are electrochromically active (become darker during lithiation) are detected this way because objects whose pixels intensities do not differ between the lithiated and delithiated images do

not appear in the difference image. SEM images are used to double check for inactive particles and masks are drawn manually. Additionally, artifacts introduced by the macroscopic scratch must be ignored (see the top right corner for each image in **Figure 3.15**).

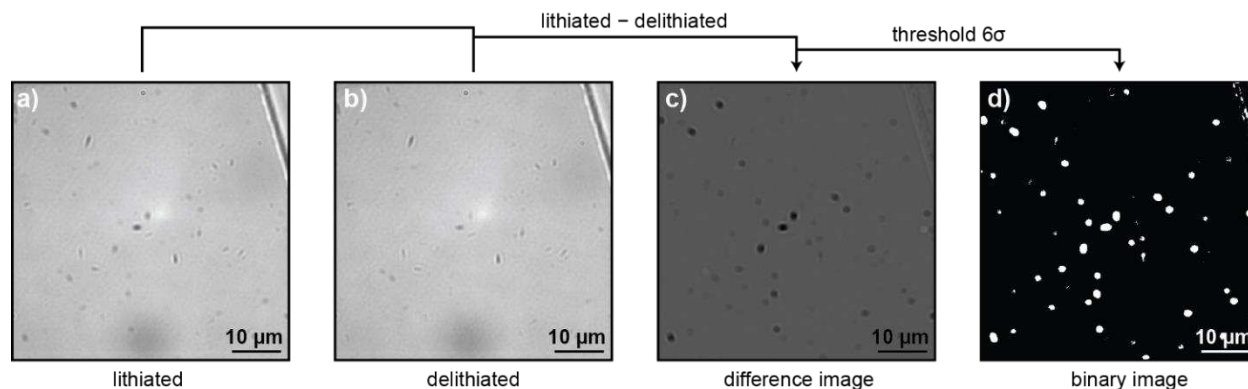


Figure 3.15 – Image processing for object boundaries in optical images. a) Average optical transmission image of lithiated WO₃ nanoparticles (NPs) on the ITO electrode. b) same as in (a), but for WO₃ NPs in the delithiated state. c) Difference image obtained from (a) and (b). d) Thresholded binary image of (c). White pixels indicate lithiated particles and black pixels represent ITO pixels or inactive particles.

The integrated intensity of the pixel values from the particle and background are used to calculate optical density. Pixel intensity is proportional to the amount of transmitted light hitting the detector. Particle signal, I , and background signal, I_0 , as defined in Equation 2-3 is used to calculate optical density for each particle at each frame. Figure 3.16 shows an optical image with masks I and I_0 in blue and green for particle and background masks, respectively. Particle masks are made by using the `poly2mask` function in MATLAB with the particle boundaries determined by the binary image (**Figure 3.15d**) as the input polygon. Background masks of equal size are created by translating the particle mask to a nearby area where there are no particles (Fig3.16b). Figure 3.16c shows I_0 and I plotted with time. The background signal is potential independent. The particle signal is potential dependent and lower in intensity relative to the background. Figure 3.16d shows a representative potential dependent OD response used to probe ion insertion dynamics.

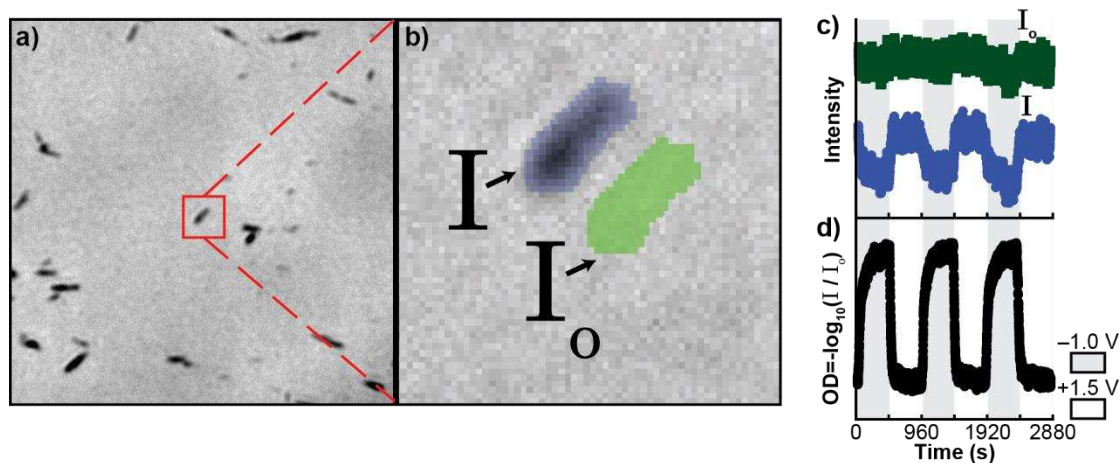


Figure 3.16 – Image analysis procedure for single particle $\Delta OD(t)$ trajectories. a) Representative bright field transmission image of a h-WO₃ NR/ITO electrode. b) Cropped transmission image from the red square in (a). The blue and green pixel areas represent equal-sized pixel areas from a WO₃ NR and ITO substrate, respectively, and therefore the light transmitted through a single nanorod (I) and the ITO substrate (I₀). c, I (blue circles) and I₀ (green squares) trajectories from the regions in (b). d) OD(t) trajectory calculated according to $-\log_{10}(I/I_0)$ in (c).

3.3.7 X-Y Stage Drift

The sample stage can drift in the x-y plane over time which must be accounted for when using the masking method in 3.3.6 Image Processing. During long movies (usually > 2 hours) the sample stage moves due to environmental impacts like temperature fluctuations and mechanical vibrations in the room. The affect is a series of images that have some shift relative to one another resulting in masks that do not fit on all particles at all frames. If ignored, then the integrated pixel intensity in that mask would no longer reflect the ion insertion dynamics for that object at long times. To circumvent this issue, a custom code in MATLAB is used to shift the relative position of all masks by tracking the centroid of several objects as they drift with time. First, a binary image is produced by thresholding against the background like in **Figure 3.15d** but for each image rather than a difference image. **Figure 3.17a** shows a binary image for an individual object at some frame, n . The function `centroid` is used in MATLAB for find the centroid of the binary object. **Figure 3.17b** shows the same binary object at frame $n + 1$ that has drifted some distance in the x-y plane. The centroid position in frame $n + 1$ is compared to frame n and that distance traveled is

calculated and applied to the particle and background masks before the integrated pixel intensity is calculated.

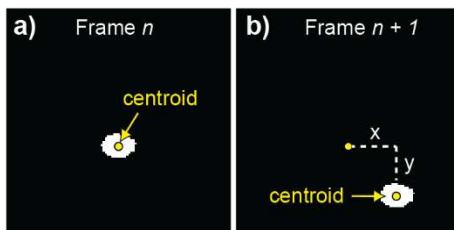


Figure 3.17 – Illustration of x-y drift. a) Binary image containing one object with the centroid (yellow circle) at some frame, n . b) Binary image of the same object as in (a) but shifted in the x-y plane.

3.3.8 Calculating the Optical Density Profile Along a Single Nanorod

Figure 3.18 shows the experimental procedure that was used to calculate the optical density gradient for all nanorods longer than $1.5 \mu\text{m}$. First, the centroid position, end points, and edge pixels (or nanorod contour) in SEM and optical images of the same nanorod (**Figure 3.18a-b**) were determined. The nanorod structural contour from the SEM image was overlaid onto the optical image by (1) determining the centroid positions of the same near diffraction-limited objects in SEM and optical images, (2) fitting the geometric transformation using the `fitgeotrans` function in MATLAB, and (3) overlaying the nanorod contour pixels on the optical image using the `transformPointsForward` function. Next, the nanorod was divided into ~ 200 nm bins extending from the nanorod centroid position (blue squares in **Figure 3.18c**). $\Delta\text{OD}(t)$ trajectories were extracted from each bin and the $\Delta\text{OD}^{\text{max}}$ values were calculated from the average of three consecutive coloration/bleaching cycles. To ensure that the OD data stems from equal-sized 200 nm bins only, nanorod end caps in the last bins are ignored.

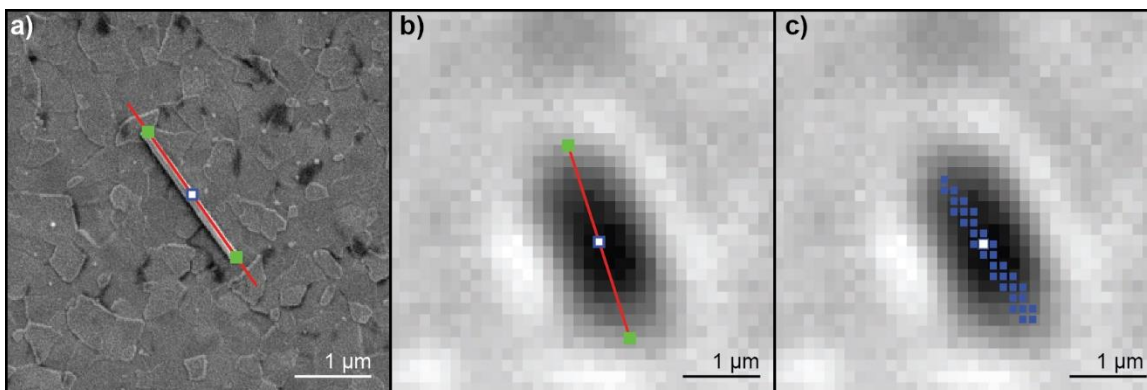


Figure 3.18 – Experimental procedure to calculate the optical density profile along a single nanorod. a) SEM image of a nanorod. The nanorod major axis, end points, and centroid are extracted. The red line represents a linear fit to the nanorod pixels and therefore the major axis. The green squares represent the nanorod end points. The blue square represents the centroid position. b) Optical image of the same nanorod in (a). The red line, green squares and blue hollow square represents the nanorod major axis, end points, and centroid position, respectively. c) Same transmission as in (b) but the blue squares represent 200 nm segments for ΔOD versus distance to centroid analysis.

3.3.9 Limit of Detection

Limit of detection (LOD) was calculated to estimate the minimum h-WO₃ nanoparticle size that can be measured by this electro-optical imaging approach. ΔOD trajectories were extracted from single pixels in the bare regions of the ITO electrode to calculate the noise in the optical density measurement. **Figure 3.19a** shows a single pixel ΔOD trajectory from two background pixels during a potential step experiment. The trajectory shows no OD change, indicating that the ITO electrode does not undergo an electrochromic lithiation reaction at these cathodic potentials. The distribution in **Figure 3.19b** was fit with a Gaussian function to obtain the population mean (μ) and the standard deviation (σ) and calculated the limit of detection at a single particle level, defined the LOD as $\mu+3\sigma$. The analysis in Figure 6a-b was repeated for 58 single pixels and determined that the average single pixel LOD is 1.08×10^{-2} (**Figure 3.19c**).

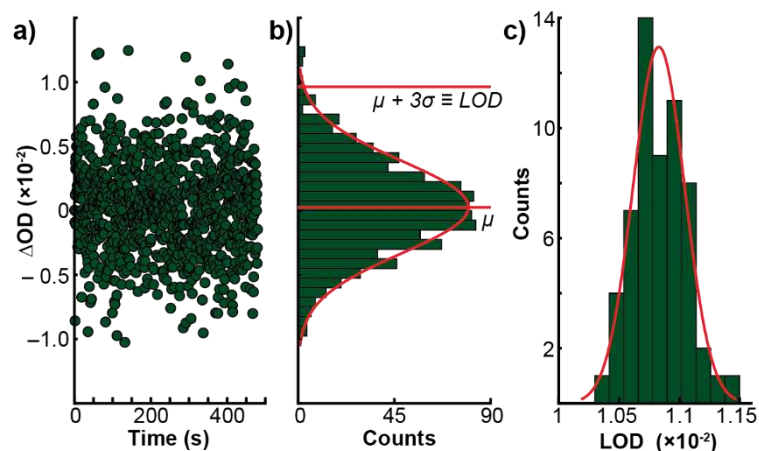


Figure 3.19 – Determination of the limit of detection. (a) Single background pixel $\Delta OD(t)$ trajectory during a cathodic potential pulse (-1.0 V vs Ag/AgCl). The data points represent the average response of three pulses. (b) Histogram of the data in (a). The data was fit with a Gaussian function to obtain the population mean $\mu = 2.75 \times 10^{-4}$, the standard deviation σ (3.70×10^{-3}), and the single pixel limit of detection ($LOD = \mu + 3\sigma = 1.11 \times 10^{-2}$). (c) The distribution of 58 single pixel LOD values. The single pixel average $LOD = 1.08 \times 10^{-2}$.

The smallest WO_3 nanoparticle that could produce a larger OD response than the LOD was calculated using the single pixel LOD. To do so, Equation 2-4 was rearranged to solve for d when $d = LOD/\epsilon(940 \text{ nm})\Delta c$. Important assumptions include (1) a spherical geometry where d is the particle diameter, (2) all W^{5+} sites in the particle volume contribute to coloration (i.e., we calculate Δc for a given particle diameter assuming that $x = 1$ in Equation 2-1), and Equation 2-2 $\epsilon = 10^6 \text{ cm}^2/\text{mol}$ at 940nm .⁸¹ The smallest particle that can be detected using this electro-optical approach was calculated to be about 13 nm. Note that the diffraction-limited electro-optical imaging method cannot directly resolve the morphology of nanoparticles. Ex situ SEM or TEM measurements are necessary to correlate OD changes with particle morphology.

CHAPTER 4: INVESTIGATION OF STRUCTURE-PROPERTY RELATIONSHIPS IN HEXAGONAL WO₃ NANORODSⁱⁱ

Nanomaterials have tremendous potential to increase electrochromic smart window efficiency, speed, and durability.⁸² However, nanoparticles vary in size, shape, and surface defects, and it is unknown how nanoparticle heterogeneity contributes to particle-dependent electrochromic properties (i.e. coloration/bleaching kinetics and optical density magnitude). Structure-property relationships in h-WO₃ nanorods were explored by quantifying the impact of particle size, morphology, and particle-particle interactions on electrochromic dynamics. Measurements during chronoamperometry revealed two distinct kinetic regimes for ion insertion observed via an optical handle. One that scales exponentially with time, and one that scales with the square root of time. The exponential and square root relationships are termed pseudocapacitance and diffusion-limited, respectively. Both are the result of the same physical phenomena – ion insertion into a solid. Additional results include a particle-dependent waiting time for coloration due to Li-ion insertion at optically inactive surface sites. Further, longer nanorods tend to tint darker because they store more Li-ion color centers at surface step sites. The particle-dependent waiting time, coloration rates, and magnitudes contribute to unwanted spatial and temporal tinting performance across large area electrochromic windows. Particle-particle interactions were quantified and showed to impact tinting dynamics and reversibility. Interestingly, single particles tint 4× faster and cycle 20× more reversibly than thin films made of the same particles. A nanostructured electrode architecture that optimizes optical modulation rates and reversibility across large area smart windows is proposed. Lastly, heterogeneity in optical response during cyclic voltammetry is discussed.

ⁱⁱ This chapter contains adaptations from Evans, R. C.; Ellingworth, A.; Cashen, C. J.; Weinberger, C. R.; Sambur, J. B. Influence of Single-Nanoparticle Electrochromic Dynamics on the Durability and Speed of Smart Windows. *Proc. Natl. Acad. Sci.* **2019**, *116* (26), 201822007. <https://doi.org/10.1073/pnas.1822007116>, citation⁽⁶⁹⁾ and Evans, R. C.; Nilsson, Z. N.; Sambur, J. B. High-Throughput Single-Nanoparticle-Level Imaging of Electrochemical Ion Insertion Reactions. *Anal. Chem.* **2019**, *91*, 14983–14991. <https://doi.org/10.1021/acs.analchem.9b03487>. citation⁽⁷⁵⁾ R.C.E. and J.B.S. designed research; R.C.E. performed research; R.C.E., A.E., C.J.C., C.R.W., and J.B.S. analyzed data; and R.C.E., C.R.W., and J.B.S. wrote the paper.

Results in this section lead to two publications^{69,75} and formed the basis for the hypotheses explored in CHAPTER 5: and CHAPTER 6:. Briefly, enhanced coloration of long nanoparticles was attributed to step edge defects. These defects expose new crystalline facets implying the surface arrangement of atoms impacts ion insertion dynamics into h-WO₃ – a result present in battery literature, but nearly nonexistent in the electrochromics literature. CHAPTER 5: explores the influence of crystalline facets on electrochromic performance. Next, the stark heterogeneity in electrochemical performance for nominally identical particles in addition to two distinct kinetic regimes motivated the potential dependent study in CHAPTER 6:.

4.1 Kinetic Model

A major result in this study revolves around the optically detected ion insertion reaction (Equation 2-1) occurring both exponentially and with the square root of time. To reiterate, the exponential and square root relationships during chronoamperometry are termed pseudocapacitance and diffusion-limited, respectively. Both are the result of the same physical phenomena – ion insertion into a solid. The exponential relationship is of particular importance for highspeed electrochromic smart windows and energy storage devices. This section will lay the foundation for the kinetic model used to fit the single particle optical response during chronoamperometry throughout this document.

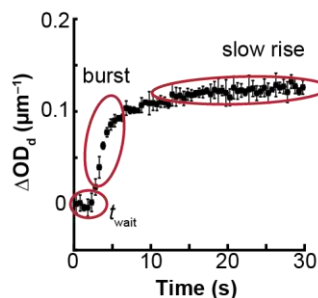


Figure 4.1 – Single particle electro-optical kinetics. A cathodic chronoamperometric pulse (-1.0 V vs Ag/AgCl) induces an optical response with three distinct regions in h-WO₃: 1) a period with no optical change (t_{wait}), 2) a burst, and 3) a slow rise.

Figure 4.1 shows the thickness corrected optical density change, ΔOD_d , with time during a cathodic pulse. Recall from Equation 2-4 that thickness correction for single particles depicts the change in concentration of absorbing species (and therefore inserted ions). The ΔOD_d trajectory is composed of three

distinct regions: 1) a period with no optical change (t_{wait}), 2) a burst, and 3) a slow rise. Each region reveals fundamental insight into ion dynamics in solids and must be accounted for in the kinetic model.

Electrochemical models by Bohnke and Vullimin⁸³, and Faughnan, Crandall and Lampert^{84,85}, and others⁸⁶⁻⁸⁹ that all consider the total flux of current, $J(t)$, consist of: (1) a non-faradaic double layer charging current (J_{DL}) that decays exponentially with time t , (2) a pseudocapacitive current (J_{pseudo}) due to Li-ion insertion at surface sites that decays exponentially with t , and (3) a diffusion-limited current (J_{diff}) due to Li-ion insertion at bulk sites that decays with $t^{-1/2}$ as in the Cottrell equation^{86,87}, were adapted to quantitatively model single nanorod $\Delta OD_d(t)$ trajectories. These contributions are summarized in Equation 4-1 below:

$$\begin{aligned}
 J(t) &= J_{DL}(t) + J_{pseudo}(t) + J_{diff}(t) && \text{Equation 4-1} \\
 &= \frac{\Delta E}{R} \exp\left(\frac{-t}{RC}\right) + A \exp(-k_{pseudo}t) + \frac{Q_{max}\sqrt{D_{Li}}}{d\sqrt{\pi t}}
 \end{aligned}$$

Where ΔE is the change in cell potential, R is the cell resistance, C is the capacitance (therefore RC is the time constant of the cell), A is a preexponential factor, Q_{max} is the maximum charge injected, D_{Li} is the lithium diffusion constant, and d is the thicknesses of the film.

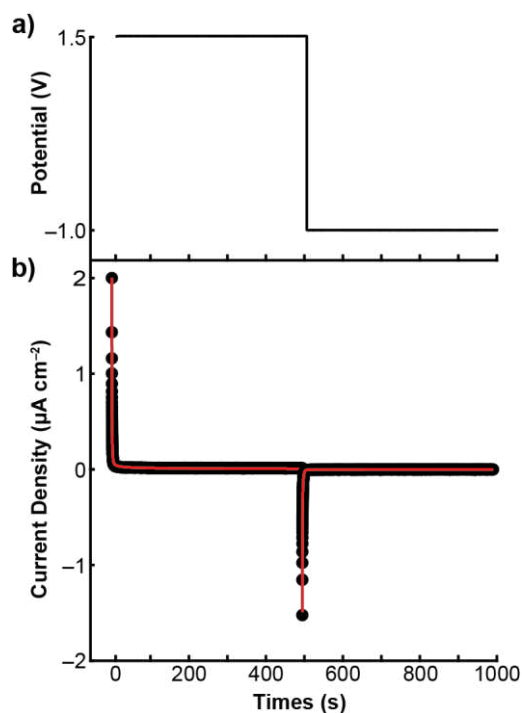


Figure 4.2 – Current-time response of these h-WO₃ NR/ITO electrodes. a) Potential versus time waveform and (b), corresponding current versus time response (black dots). The red line represents a fit to the current versus time response using Equation 4-1. Fitting current-time data with Equation 4-1 yields $A = 5.1 \times 10^{-6} \text{ C/s-cm}^2$, $k_{\text{pseudo}} = 0.58 \text{ s}^{-1}$, and $D' = 1.5 \times 10^{-6} \text{ C/s}^{3/2}\text{-cm}^2$ for the bleach and $A = 4.6 \times 10^{-6} \text{ C/s-cm}^2$, $k_{\text{pseudo}} = 0.85 \text{ s}^{-1}$, and $D' = 1.4 \times 10^{-5} \text{ C/s}^{3/2}\text{-cm}^2$ for coloring. Ag / AgCl was used as a reference electrode.

Figure 4.2 shows the current-time response of the single particel h-WO₃ electrochemical flow cell during the bleach (1.5 V) and coloration (−1.0 V) potential steps. Equation 4-1 fit the current response in **Figure 4.2b** well and qualifies this approach as a foundation for building a kinetic model.

Similar to the aforementioned studies, this model assumes the change in optical density in the WO₃ material is proportional to the change in color centers Δc , and the time-dependent change in color centers, $\Delta c(t)$, can be calculated by integrating the experimentally measured current density $J(t)$. That is, $\Delta \text{OD}(t)$ is proportional to the time-dependent charge inserted into the electrode, $\Delta Q(t)$, whoes only contributors are faridaic. Double layer charging does not induce an electrochromic response. Thus $\Delta c(t)$ is a sum of pseudocapactive and diffusion limited copmenents ($\Delta c_{\text{pseudo}}(t)$ and $\Delta c_{\text{dif}}(t)$, respectively). Equation 2-4 can be expanded to Equation 4-2:

$$\frac{\Delta OD(t)_d}{\varepsilon} = \Delta c(t) = \Delta c_{\text{pseudo}}(t) + \Delta c_{\text{diff}}(t) \quad \text{Equation 4-2}$$

Which implies only charge contributions from pseudocapacitance and diffusion limited reactions (ΔQ_{pseudo} and ΔQ_{diff}) should be considered in a model that fits an optical response due to faradaic ion insertion (Equation 4-3).

$$\Delta Q_{\text{pseudo}}(t) + \Delta Q_{\text{diff}}(t) = \int_{t_{\text{wait}}}^t J_{\text{pseudo}}(t) dt + \int_0^t J_{\text{diff}}(t) dt \quad \text{Equation 4-3}$$

The existence of t_{wait} was unexpected and is not discussed in the literature. No optical change is observed for a period of time after a cathodic potential is applied to the cell even though current is measured. For this to be true, ions must be injected into the material which implies that not all ion insertion results in a color change. Note t_{wait} is an order of magnitude longer than double layer charging and must involve faradaic charging. J_{DL} is not responsible for t_{wait} . The physical justification for t_{wait} is given in in section 4.2.1. For now, only the mathematical treatment of t_{wait} will be considered. There are two important features of t_{wait} that must be considered for the fit: 1) it must be variable fit because t_{wait} is particle dependent, and 2) the magnitude of ΔOD_d must not increase during t_{wait} . Both of these criteria are met with use of the Heaviside function. Combining Equation 4-1 and Equation 4-3, incorporating a Heaviside function, $H(t-t_{\text{wait}})$, and integrating yields the kinetic model used to fit optical changes under chronoamperometric conditions, Equation 4-4:

$$H(t - t_{\text{wait}}) \left(-\frac{A}{k_{\text{pseudo}}} [\exp(-k_{\text{pseudo}}t) - \exp(k_{\text{pseudo}}t_{\text{wait}})] \right) + 2D'\sqrt{t} \quad \text{Equation 4-4}$$

Where A , k_{pseudo} , t_{wait} , and D' are fitting parameters. D' is given by Equation 4-5 below

$$D' = \frac{Q_{max}\sqrt{D_{Li}}}{d\sqrt{\pi}} \quad \text{Equation 4-5}$$

Fitting is done using a custom code in MATLAB. Fitting the data in **Figure 4.1** using Equation 4-4 gives **Figure 4.3**.

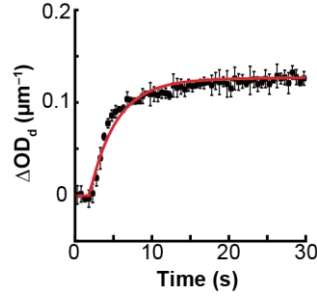


Figure 4.3 – Thickness corrected optical density response at -1.0 V vs Ag/AgCl fit with kinetic model. A cathodic chronoamperometric pulse induces an optical response with three distinct regions in h-WO₃: 1) a period with no optical change (t_{wait}), 2) a burst, and 3) a slow rise all fit with Equation 4-4 (red line). Error bars are standard deviation between three cycles.

4.2 Results and Discussion

4.2.1 Coloration and Bleaching Dynamics in Single h-WO₃ Nanorods

Figure 4.4 shows representative $\Delta OD(t)_d$ trajectories for three isolated nanorods with similar widths (0.11 μm , 0.16 μm , and 0.10 μm) and different lengths (1.64 μm , 0.52 μm , and 0.67 μm). The $\Delta OD(t)_d$ trajectories exhibit three distinct features: (1) a particle-dependent waiting time for a change in OD (t_{wait} , see **Figure 4.4c,f,i**), (2) an abrupt OD burst at short times, and (3) a steady OD increase at long times (**Figure 4.4b,e,h**).

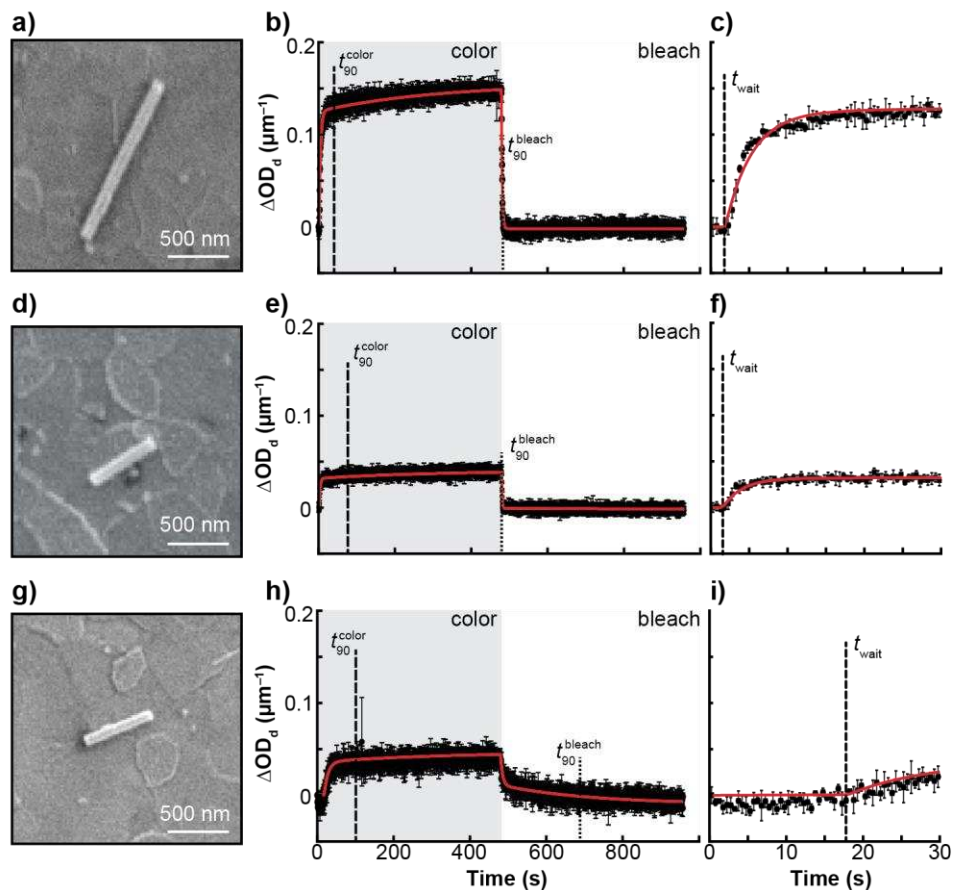


Figure 4.4 – Quantitative analysis of single nanoparticle optical density trajectories. a) SEM image of a single WO_3 nanorod (length = 1.64 μm , width = 0.11 μm). b) $\Delta\text{OD}(t)_d$ trajectory of the same nanorod in (a). The $\Delta\text{OD}(t)_d$ data points and error bars represent the mean and standard deviation of 3 consecutive cathodic (-1.0 V vs Ag/AgCl) and anodic ($+1.5$ V vs Ag/AgCl) potential cycles. The dashed vertical lines represent t_{90}^{color} (67.78 s) and t_{90}^{bleach} (4.33 s). The solid red line represents the fit to the data using equation (2) in Methods. c) $\Delta\text{OD}(t)_d$ trajectory in (b) from $t = 0$ to 30 s, showing $t_{\text{wait}} = 1.78$ s. (d-f) same data as (a-c), but for a shorter WO_3 nanorod (length = 0.52 μm , width = 0.16 μm) with longer t_{90}^{color} (115.53 s), t_{90}^{bleach} (3.33 s), and slightly longer t_{wait} (2.78 s). (g-i) same data as (a-c), but for a shorter WO_3 nanorod (length = 0.67 μm , width = 0.10 μm) with longer t_{90}^{color} (96.78 s), t_{90}^{bleach} (209.33 s), and much longer t_{wait} (18.03 s).

The waiting time is rationalized through binding dynamics in the crystal – consider that $h\text{-WO}_3$ has three Li-ion binding sites: hexagonal windows (HW), square windows (SW), and trigonal cavities (TC) (**Figure 4.5**).^{52–54,81} Balaji et al. showed that Li ions fill TC sites first, but only HW and SW sites contribute to coloration in porous hexagonal WO_3 films⁵⁴, in agreement with electronic structure calculations.⁵² Thus, we attribute the waiting time to Li-ion insertion at optically inactive TC sites.

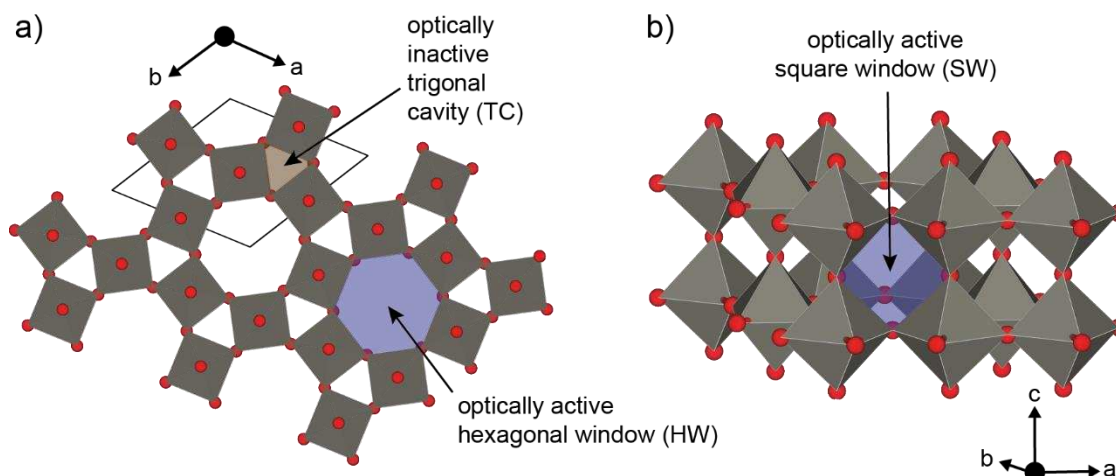


Figure 4.5 – Li-ion binding sites in hexagonal WO_3 . Structure of $h\text{-WO}_3$ with c -axis a) perpendicular and b) parallel to the plane. The TC site is optically inactive. The HW and SW sites are optically active.

The OD burst behavior can be described as pseudocapacitance. Cyclic voltammetry data verifies an electrochemical signature for pseudocapacitive behavior in these $h\text{-WO}_3$ nanorods (**Figure 4.6**).⁹⁰ Pseudocapacitance is a faradaic capacitive charging process that is associated with rapid charge transfer reactions at or near the electrode surface.¹ The OD burst behavior can be attributed to Li ion insertion at optically active HW and SW surface sites because we observed that $\Delta\text{OD}(t)_d$ scales exponentially with t , consistent with a capacitive surface charging process. Intercalation pseudocapacitance throughout the nanorod bulk is not expected in these $h\text{-WO}_3$ nanorods because bulk pseudocapacitance requires a unique crystalline network.⁷ The slow OD rise behavior can be attributed to a diffusion-limited Li-ion insertion process at bulk HW and SW sites because we observed that $\Delta\text{OD}(t)_d$ scales with $t^{1/2}$ at long times, in agreement with the Cottrell equation.⁸⁶ While we do not directly image Li-ion insertion at bulk versus surface sites, we distinguish the rapid surface Li-ion insertion reaction (i.e., pseudocapacitance) from the slow bulk Li-ion insertion process, respectively, in agreement with the literature.^{91–95}

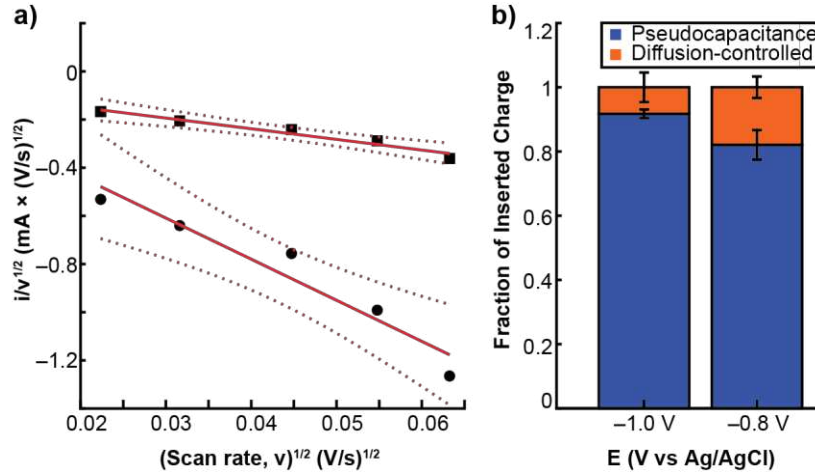


Figure 4.6 – Electrochemical characterization of ensemble WO_3 nanorod film. a) Electrochemical response versus scan rate according to equation (S1). The circles and squares represent currents measured at -1.0 V (circles) and -0.08 V (squares) vs Ag/AgCl, respectively. The solid red line represents a linear fit and the dashed lines represent the 95% confidence intervals. b) Fraction of injected charge using the constants k_1 and k_2 from the fit in (a) according to Equation 4-6. The blue and orange bars represent the fractions of pseudocapacitive surface charge and diffusion-controlled bulk charge, respectively. Error bars represent the standard error of the mean.

Following Dunn and co-workers⁹⁰, we plotted current at a fixed potential versus the square root of the scan rate and observed that $i(E)/\sqrt{v}$ scales linearly with \sqrt{v} (**Figure 4.6a**). This scaling relation is consistent with Equation 4-6, indicating that the current response stems from a fast surface charge transfer reaction (pseudocapacitance) with a rate constant k_1 and a slow bulk Li-ion diffusion reaction with a rate constant k_2 . **Figure 4.6b** shows that the majority of charge injected into these WO_3 NRs stems from the pseudocapacitive process.

$$\frac{i(E)}{\sqrt{v}} = k_1\sqrt{v} + k_2 \quad \text{Equation 4-6}$$

To quantitatively analyze the $\Delta\text{OD}(t)_d$ trajectories of 102 individual h - WO_3 NRs, we developed a time-dependent electrochromism model that accounts for (1) t_{wait} , (2) the pseudocapacitive OD burst, and (3) the slow OD rise (see 4.1 Kinetic Model). In this model, Li-ion insertion at reduced W^{5+} sites are responsible for coloration as we observe no W^{4+} species in X-ray photoelectron spectroscopy measurements (XPS, **Figure 4.7**). Fitting Equation 4-4 to the $\Delta\text{OD}(t)_d$ data (see solid red lines in **Figure 4.4b,e,h**) yields t_{wait} , a rate constant for the surface charge transfer reaction (k_{pseudo}), and the total charge inserted into

optically active HW and SW sites ($Q_{\text{diff}}^{\text{active}}$ and $Q_{\text{pseudo}}^{\text{active}}$). In addition, we extract smart window performance metrics such as the particle thickness-corrected maximum change in OD ($\Delta\text{OD}_d^{\text{max}}$), the time required to reach 90% of $\Delta\text{OD}_d^{\text{max}}$ (t_{90}^{color}), and the time required to decay from $\Delta\text{OD}_d^{\text{max}}$ by 90% (t_{90}^{bleach}).

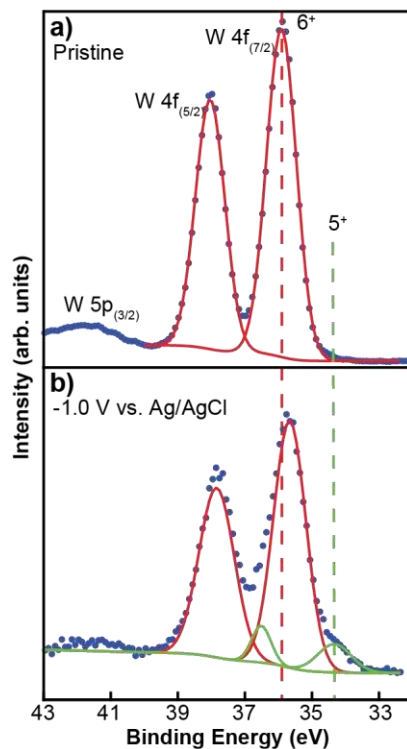


Figure 4.7 – X-ray photoelectron spectroscopy of a h-WO₃ NR film. a) before and b) after coloration for 600 s at -1.0 V vs Ag / AgCl. The blue dots represent the data and the solid red lines represent fits from Multipack (v. 9.3) software. The red and green dashed vertical lines represent expected peak positions of W 4f core level binding energies that are consistent with W⁶⁺ and W⁵⁺ oxidation states, respectively. The chamber pressure was 10^{-8} mbar.

Figure 4.7 shows X-ray photoelectron (XPS) spectra of pristine and colored WO₃ nanorod films. The XPS spectrum of the pristine film shows W 4f_(7/2) and W 4f_(5/2) peaks at 36.2 eV and 38.3 eV that are consistent with W⁶⁺. Upon coloring the film at -1.0 V for 600 s, a new peak appears at 34.7 eV that indicates the formation of W⁵⁺ sites.⁹⁶ The colored film does not show peaks at $\sim 33 - 32$ eV that would indicate the formation of W⁴⁺.⁹⁷

The widefield imaging approach measures hundreds of nanoparticles in a single experiment. We observed that 9% (9/102) of single particles showed no optical modulation and 6% (6/102) of single

particles showed anomalous tinting behavior during cathodic polarization cycles. **Figure 4.8** shows several types of anomalous optical behavior, define here as a deviation from the average of all single particles. The potential significance of the inactive and anomalous particles will be discussed below.

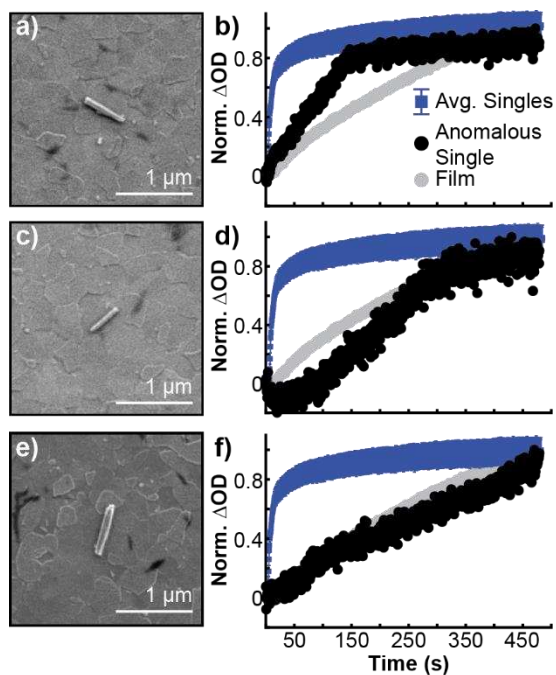


Figure 4.8 – Examples of anomalous optical modulation behavior. a, c, e) SEM image of a single WO_3 nanorod. b, d, f) Normalized OD trajectory for the pictured nanoparticle (black circles) compared to the normalized trace for the average of all single nanoparticles (blue squares) and film (grey circles). The error bars for the average of singles represent the standard error of the mean. Error bars for abnormal OD trajectories are omitted for clarity.

This small anomalous nanoparticle population did not show a clear ΔOD burst followed by a slow ΔOD rise that could be reproducibly fit by Equation 4-4. The anomalous particles also exhibit pulse-dependent optical modulation dynamics and magnitudes. Anomalous and dead particles were not fit with equations 2-3 in Methods; therefore 83/98 particles were fit with Equation 4-4. It is notable that the $\Delta\text{OD}(t)$ dynamics of anomalous particles are qualitatively similar to that of the thin film electrode. However, it is unclear to what extent anomalous particles affect ΔOD dynamics of large nanoparticle clusters and the thin film electrode.

4.2.2 Effect of Particle Size and Surface Structure on Optical Density Magnitude and Dynamics

Figure 4.9a shows a positive Pearson correlation coefficient between ΔOD_d^{\max} and nanorod length; on average, longer nanorods tint darker than shorter nanorods. However, particles with identical lengths can exhibit an order of magnitude difference in ΔOD_d^{\max} under identical experimental conditions. The trajectory analysis revealed that longer nanorods store more surface charge per geometric area (**Figure 4.9b**) and more bulk charge per volume than shorter nanorods (**Figure 4.9c**). These trends are hidden in ensemble-level electro-optical measurements and unexpected because the number density of Li-ion binding sites does not scale with surface area and volume in perfect crystals.

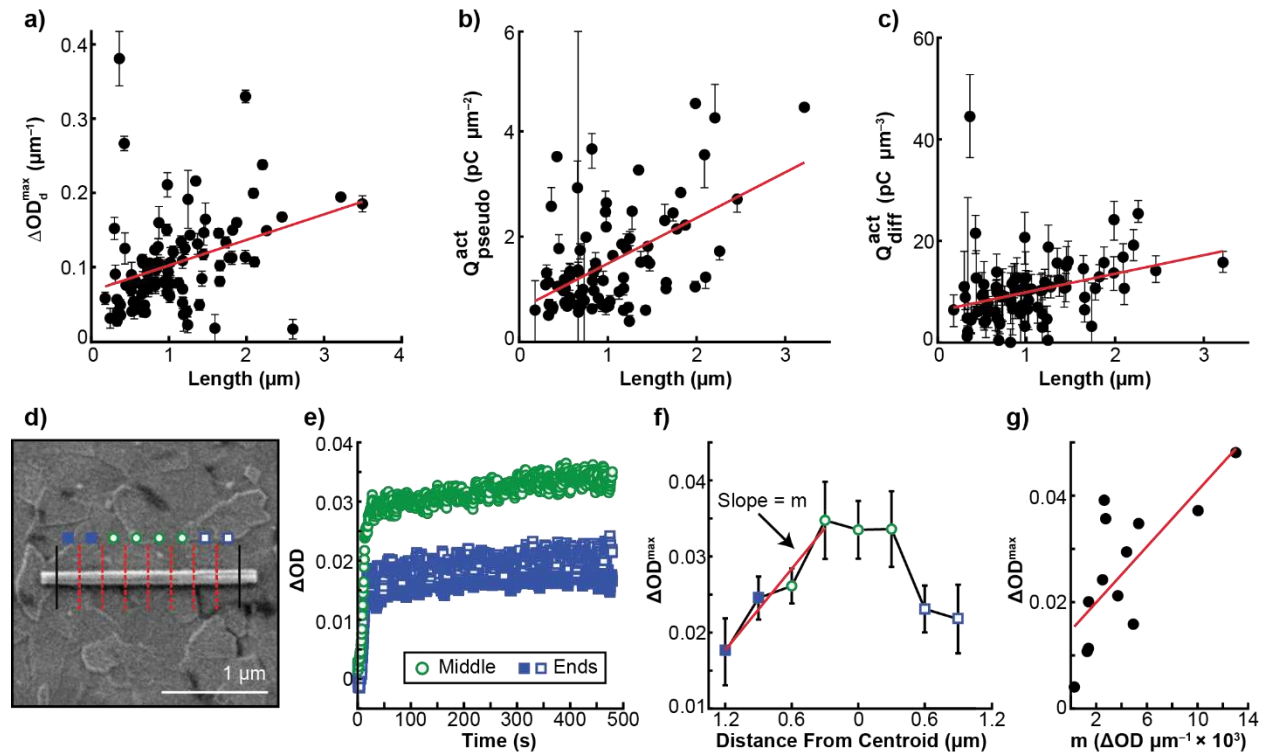


Figure 4.9 – Correlation between optical density magnitude and nanorod structural properties. a) The particle thickness-corrected change in optical density ΔOD_d^{\max} versus nanorod length (Pearson correlation coefficient $\rho = 0.34 \pm 0.06$, $N = 98$ particles). b) Charge inserted into optically active surface sites per electrochemically active surface area of the nanorod $Q_{\text{pseudo}}^{\text{active}}$ versus length ($\rho = 0.52 \pm 0.05$, $N = 83$ particles) and c) bulk charge per unit volume $Q_{\text{diff}}^{\text{active}}$ versus length ($\rho = 0.33 \pm 0.07$, $N = 83$ particles). The black circles in (a-c) represent data from individual nanorods and the solid red line is a linear fit to show the general trend. d) SEM image of a single nanorod. The distance between all vertical black and red lines represent 200 nm segments for sub-particle-level trajectory analyses. Small nanorod segments extending beyond the vertical black lines were not analyzed. e) Representative $\Delta OD(t)$ trajectories for 'Middle' (green circles) and 'Ends' (blue squares) segments. f) Plot of ΔOD^{\max} vs Distance From Centroid (μm) showing a linear fit with slope m . g) Plot of ΔOD^{\max} vs m ($\Delta OD \mu\text{m}^{-1} \times 10^3$).

measured from the middle (hollow green circles) and end segments (hollow and solid blue squares) on the single nanorod in in (d). f) Maximum ΔOD versus distance from nanorod centroid calculated from the trajectory analyses in (e). The red line represents a linear fit to the segmented data. Error bars are the standard deviation of the ΔOD within the 200 nm segment. g) ΔOD^{\max} of 13 single particles versus its slope parameter defined in (f). The red line is a linear fit to show the general trend ($\rho = 0.73 \pm 0.31$).

The $\Delta OD(t)$ along the length of single nanorods was evaluated to probe bulk and surface charge storage trends (**Figure 4.9a-c**). The $\Delta OD(t)$ kinetics are independent of position along the nanorod (**Figure 4.9e**), but the maximum OD increases from the nanorod ends towards its middle (**Figure 4.9f**). The OD trend in **Figure 4.9f** indicates that more ($\text{Li}^+ \text{-W}^{5+}$) color centers accumulate in the middle of the nanorod than at its ends even though there are no observable structural gradients along the nanorod in SEM images (**Figure 4.9d**). Interestingly, the slope of the color center gradient is larger for nanorods with larger ΔOD^{\max} values (**Figure 4.9g**). One explanation for the ($\text{Li}^+ \text{-W}^{5+}$) color center gradient is a surface step edge gradient that propagates from the nanorod middle to the ends, as evidenced by transmission electron microscopy (TEM) imaging of separate nanorods from the same sample (**Figure 4.10**).

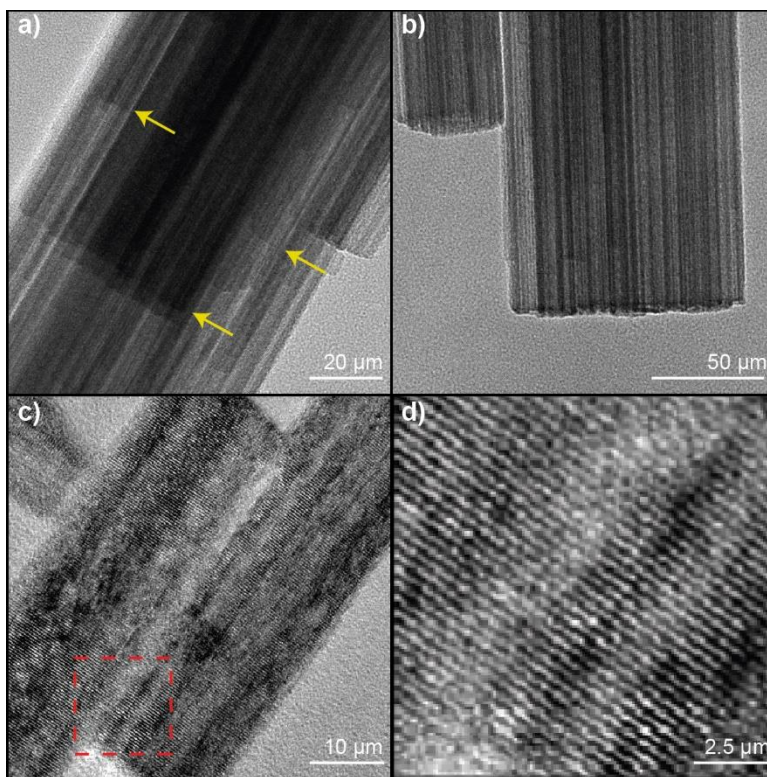


Figure 4.10 – High resolution TEM imaging of the h-WO₃ nanorod sample. a-b) Representative TEM images showing perpendicular (indicated by yellow arrows) and parallel step edge features along single

nanorods. c) TEM image showing two physically coupled nanorods and d) a zoom-in view of the interfacial region in (c) that shows a heterogeneous interfacial structure at the particle-particle interface.

Figure 4.10 shows TEM images of nanorods that were synthesized in the same batch as the 98 particles in our single-particle imaging study. **Figure 4.10a-b** shows representative TEM images of single nanorods that exhibit a particle-dependent surface step structure. The particles show a step edge gradient parallel to the nanorod length that increases Li-ion access to the nanorod interior along the *a* and *b* crystal axes. In addition, the particles show a step edge gradient perpendicular to the nanorod length (indicated by yellow arrows in **Figure 4.10a-b**) that increases Li-ion access to optically active hexagonal channels along the *c* axis.⁵⁴ **Figure 4.10c** shows a TEM image of physically connected WO₃ nanoparticles. **Figure 4.10d** shows a heterogeneous surface structure at the particle-particle interface that could account for cluster-dependent Li-ion trapping kinetics at particle-particle interfaces.

Highly stepped surfaces have more Li-ion insertion sites than smooth surfaces and therefore more optically active surface sites per geometric area than a perfect crystal. Since the nanorods grow outward from a pre-formed core^{46,98} and the growth rate of different crystal planes varies⁴⁶, then a defect gradient could develop along the nanorod side facets⁹⁹ with the highest defect density at the nanorod center and the lowest defect density at the ends¹⁰⁰. Another possibility for the trend in **Figure 4.9c** is that electric fields at step edges facilitate Li-ion transport from the nanorod ends toward the middle along the large hexagonal channels of *h*-WO₃ nanorods.^{101–103}

Having determined the correlation between nanorod structure and optical density magnitude, we then explored optical modulation kinetics at the single nanorod-level. Interestingly, we observed no strong correlations between OD kinetic parameters (e.g., t_{90}^{color} , t_{90}^{bleach} , t_{wait} , and k_{pseudo}) and particle length (**Figure 4.11**), width, geometric surface area, or volume (see the following figures). The fact that t_{90}^{color} , t_{90}^{bleach} , t_{wait} , and k_{pseudo} are not correlated with bulk structural properties implies that electrochromic kinetics are dominated by particle-dependent properties such as defect sites. The presence of impurity atoms and defects are unavoidable for nanomaterial samples that even share the same side facets (they also occur in

bulk WO_3^{104}). Our single-particle approach circumvents the issue of particle-to-particle heterogeneity, a challenge for conventional ensemble measurements that average differences among particles.

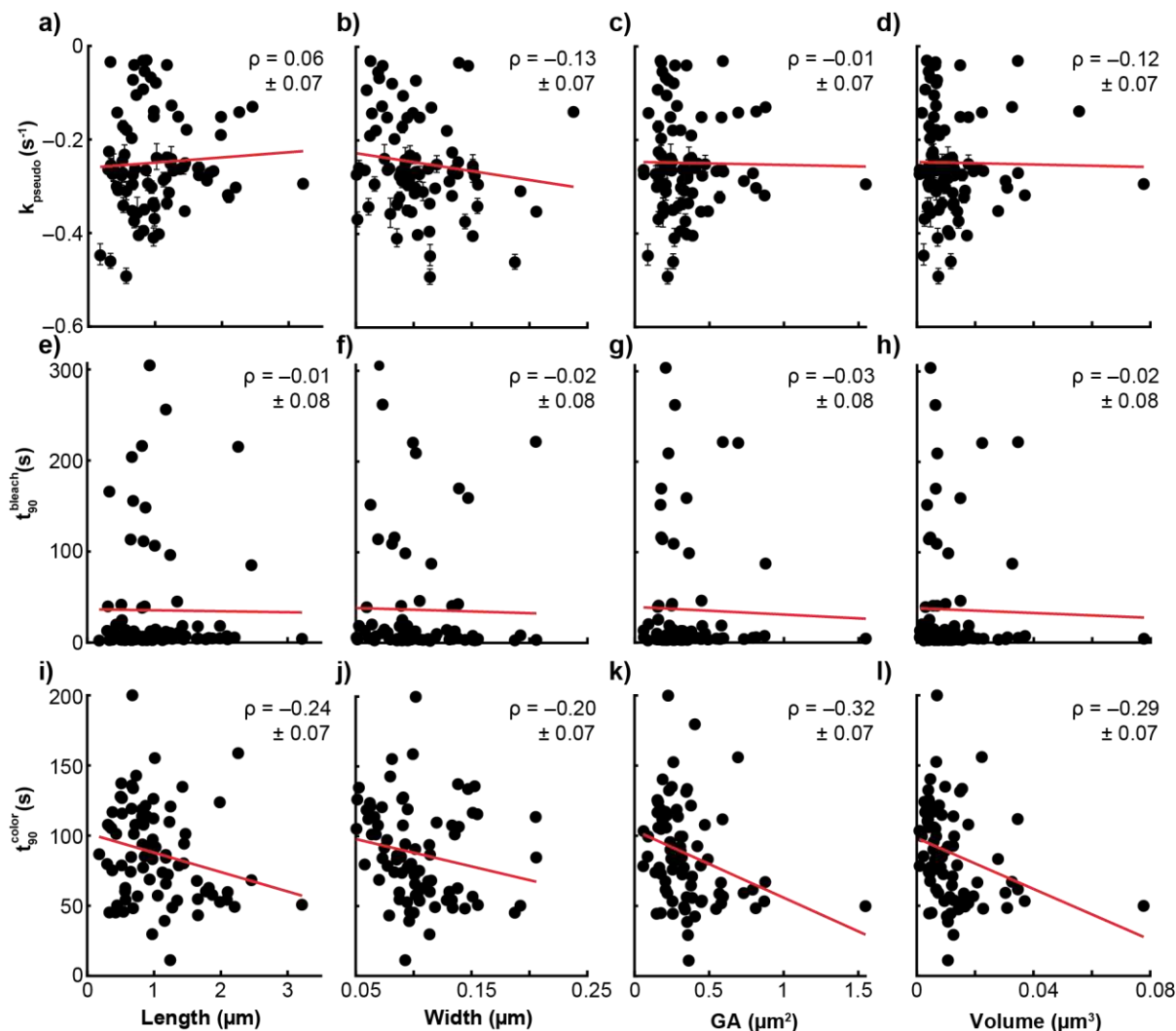


Figure 4.11 – Correlation between electrochromic kinetic parameters and physical properties of individual nanorods. (a-d) Correlations between surface charge transfer rate constant k_{pseudo} and length, width, geometric surface area (GA) exposed to electrolyte, and volume. (e-h) and (i-l) Correlations between t_{90}^{color} and t_{90}^{bleach} versus length, width, geometric surface area, and volume. The black circles represent data from the 83 fitted individual nanorods and the red line represents a linear fit to show the general trend. Correlation coefficients are represented as ρ . Error bar for the Pearson’s correlation coefficient calculated according to ref.¹⁰⁵

Figure 4.11 shows correlations between electrochromic kinetics and physical parameters (length, width, geometric surface area (all nanorod sidewalls in contact with the electrolyte and the end caps), and volume. No strong correlations between optical modulation kinetics and physical properties were observed

(Figure 4.11). The waiting time, t_{wait} , does not correlate strongly with any nanorod physical parameters (Figure 4.12). The fact that k_{surf} , t_{90}^{color} , t_{90}^{bleach} , and t_{wait} are not correlated with bulk structural properties implies that electrochromic kinetics are dominated by particle-dependent properties such as defect sites and the step edge gradient.

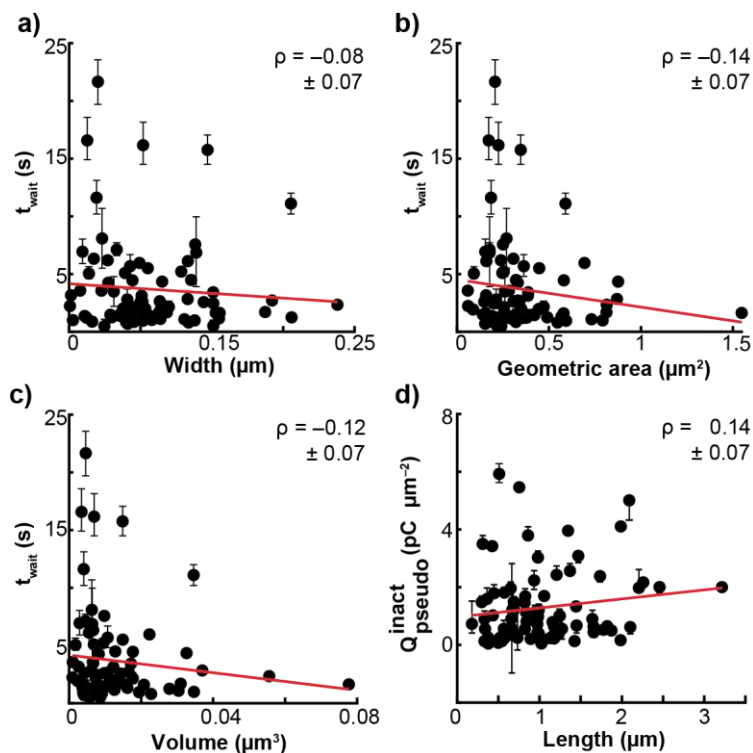


Figure 4.12 – Correlation between t_{wait} and physical properties. (a-c) Correlation between t_{wait} and width, geometric area exposed to electrolyte, and volume. Correlation coefficients are represented as ρ . d) Correlation between geometric area corrected charge injected predicted from the model versus length. Error bar for the Pearson’s correlation coefficient calculated according to ref.¹⁰⁵

We expected to observe a correlation between t_{wait} and nanorod length because longer nanorods with more step edges would have more optically inactive TC sites that contribute to a longer t_{wait} . However, the waiting time is independent of nanorod length (Figure 4.13a) and other structural properties (Figure 4.12). Optically active surface charge density is more strongly correlated with nanorod length than optically inactive charge density (Pearson correlation coefficient $\rho = 0.52 \pm 0.06$ in Figure 4.9b versus $\rho = 0.14 \pm 0.07$ in Figure 4.12d). The optically active surface charge density is more strongly correlated with nanorod length than the inactive charge density presumably because (1) the large hexagonal tunnels accommodate

more Li-ions than the small trigonal cavity tunnels¹⁰⁶, and (2) Li-ion transport is more efficient in the large, open hexagonal tunnels than in the smaller trigonal tunnels.¹⁰² Regardless of the underlying reason why t_{wait} and optically inactive surface charge is independent of length, the large variation in waiting times, from 100 ms to 20 s (**Figure 4.13a**, inset), is significant because particles with longer waiting times decrease coloration efficiency; no OD change occurs even though charge is inserted into the nanorods.

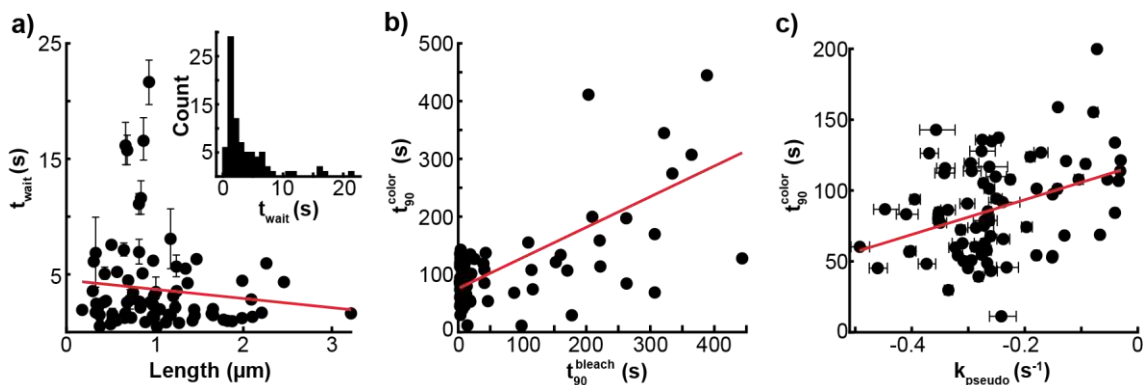


Figure 4.13 – Coloration and bleaching kinetics at the single particle-level. **a**, Waiting time for optical modulation versus nanorod length ($\rho = -0.11 \pm 0.07$). Inset shows the distribution of waiting times. **b**, Coloration versus bleaching kinetics; t_{90}^{color} versus t_{90}^{bleach} ($\rho = 0.65 \pm 0.04$). **c**, t_{90}^{color} versus k_{pseudo} ($\rho = -0.38 \pm 0.06$). The black circles in (a-c) represent data from single nanorods and red line is a linear fit to show the general trend.

A particle's maximum optical density is not correlated with its coloration and bleaching kinetics; particles that tint faster do not necessarily tint darker (**Figure 4.14**). Instead, **Figure 4.13b** shows that coloration and bleaching kinetics are strongly correlated (i.e., positive Pearson correlation coefficient), indicating that particles that color faster also bleach faster. The optical modulation times are extremely heterogeneous; some nanoparticles achieve 90% OD modulation in 12 s whereas other nanoparticles require 275 s. The strongest predictor of fast coloration in these *h*-WO₃ NRs is fast pseudocapacitive charge transfer kinetics (**Figure 4.13c**). The trend in **Figure 4.13c** suggests that Li-ion insertion at the WO₃/electrolyte interface, rather than Li-ion diffusion in the WO₃ interior, accounts for large heterogeneities in coloration/bleaching kinetics at the single particle-level, likely due to the particle-dependent stepped surface structure (e.g., **Figure 4.10**).

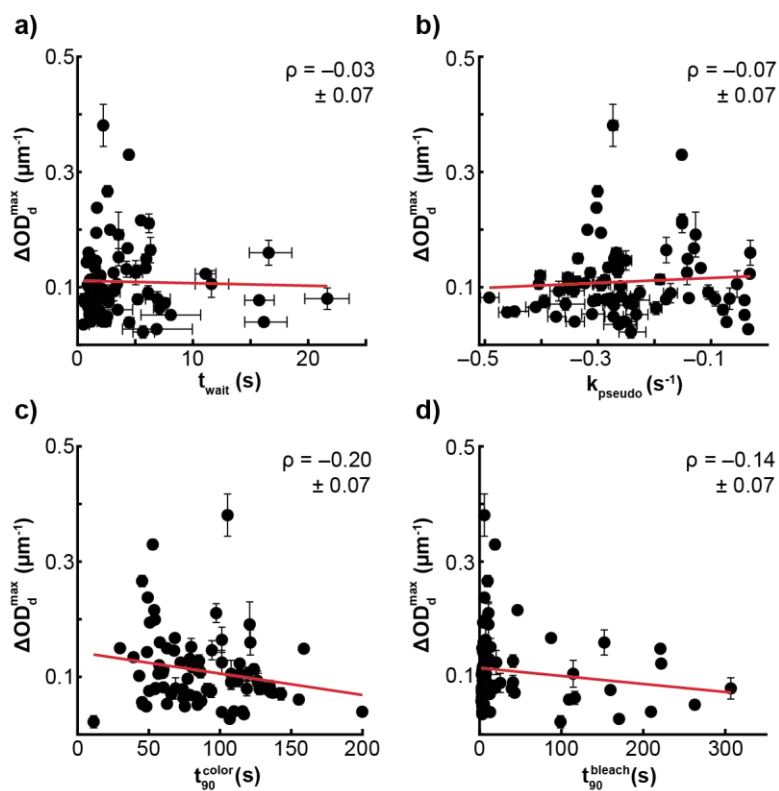


Figure 4.14 – Optical density correlations with kinetic parameters. Correlations between particle thickness corrected maximum optical density (ΔOD_d^{\max}) and a) t_{wait} , b) k_{pseudo} , c) t_{90}^{color} , and d) t_{90}^{bleach} . Error bar for the Pearson’s correlation coefficient calculated according to ref.¹⁰⁵

Figure 4.14 shows correlations between the optical change and various kinetic parameters. Optical modulation is not a strong indicator for kinetic performance indicated by poor correlation coefficients.

While the electro-optical approach does not measure electrochemical current at the single nanoparticle-level, this apparent experimental limitation does not restrict the conclusions regarding the structure function relationships of our study. Regardless of the electrochemical current flow into single particles, measurements show that longer nanorods tint darker than shorter nanorods and longer nanorods exhibit a color center gradient. These structure/property relationships hold regardless of the electrochemical current into the nanoparticles. Importantly, all the above observations were made from single particles that are attached to the same ITO electrode, immersed in the same electrolyte, and located only microns apart.

4.2.3 Role of Particle-Particle Interfaces on Electrochromic Dynamics and Reversibility

Electrochromic dynamics and reversibility were used as a proxy to evaluate whether the electrochromic properties of nanoparticle building blocks are maintained in thin film. In other words, does performance scale as a function of particle-particle interaction? Single particle $\Delta OD(t)$ trajectories were compared to those measured from particle clusters containing two, three, four, or five *h*-WO₃ nanorods. In addition, $\Delta OD(t)$ trajectories of large clusters (25-100 particles) and a thin film electrode were measured. For example, **Figure 4.15a** shows an SEM image of a cluster containing three *h*-WO₃ nanorods and **Figure 4.15b-c** shows its $\Delta OD(t)$ response (black trace) compared to the average trajectory of 98 isolated *h*-WO₃ nanorods (blue trace). The three-particle cluster showed similar $\Delta OD(t)$ dynamics compared to single particles (**Figure 4.15b-c**) and qualitatively reversible electrochromic behavior (**Figure 4.15d**). For large nanoparticle clusters (**Figure 4.15e-h**) and the thin film electrode (**Figure 4.15i-l**), the $\Delta OD(t)$ kinetics and reversibility deviate from the single particle building blocks.

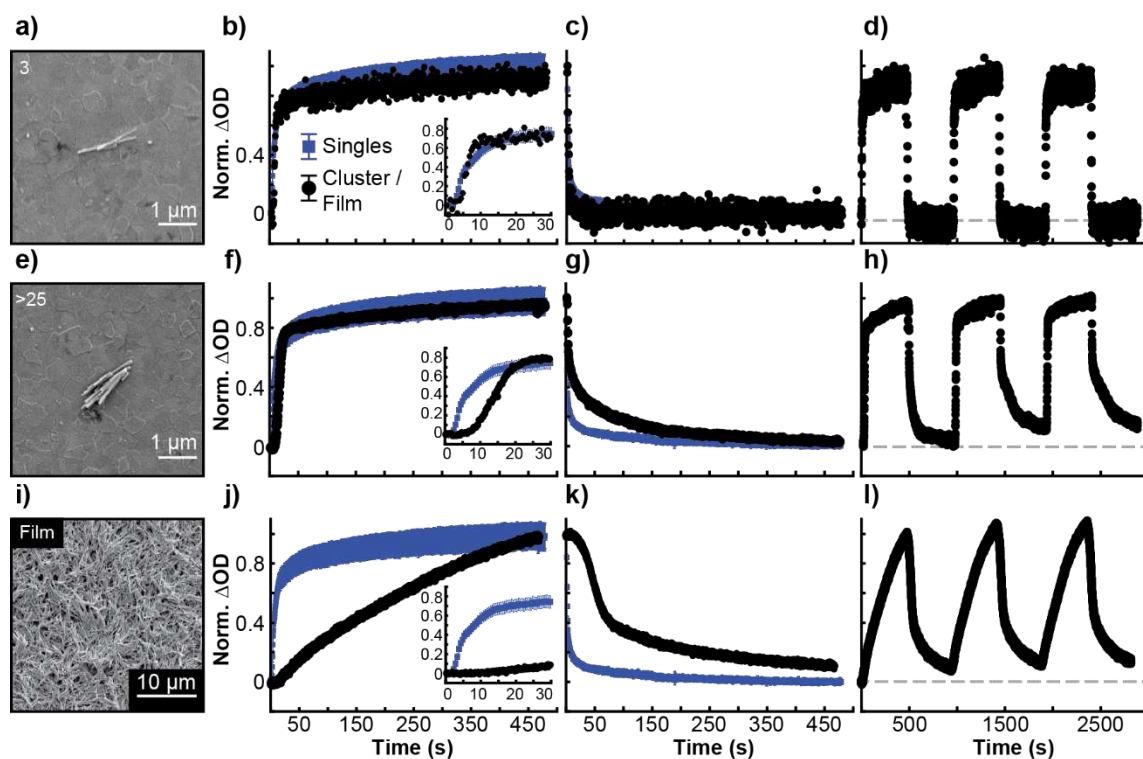


Figure 4.15 – Electrochromic dynamics and reversibility of nanorod clusters and thin films. a) SEM image of a particle cluster containing 3 nanorods. (b-c) $\Delta OD(t)$ trajectory of the cluster in (a, black trace) compared to the average trajectory of 102 single nanorods (blue trace). D) $\Delta OD(t)$ trajectory for the cluster in (a) during three consecutive color and bleaching cycles. The dashed horizontal line in (d) represents ΔOD at 0 s. (e-h) and (i-l) are the same as (a-d), but for a large 25-100 particle cluster and a thin film electrode, respectively.

To quantify the role of particle-particle interactions on tinting dynamics and reversibility, t_{90}^{color} , t_{90}^{bleach} , and the fraction of electrochromic cycles that do not return to the original transparent state for 298 clusters and 894 cycle were evaluated. Cluster size-dependent coloration magnitude was not analyzed because OD depends on cluster thickness and it was difficult to measure cluster thickness via SEM and atomic force microscopy imaging. **Figure 4.16a** shows that t_{90}^{color} and t_{90}^{bleach} are independent of particle-particle interactions in the small cluster limit (2 to 5 particles), but then both parameters increase for large clusters and the thin film electrode. The electrochromic dynamics of small particle clusters are unaffected presumably because each particle within the cluster remains in contact with the ITO electrode and the liquid electrolyte. As the number of particle-particle interactions increases (i.e., for 25-100 particle clusters and the thin film electrode), the optical modulation kinetics decrease because electrons and Li-ions must

traverse multiple particle-particle interfaces. An alternative possibility is that one anomalous single particle in one large nanoparticle cluster dominates the $OD(t)$ response because we observed that the $OD(t)$ kinetics of anomalous particles are strikingly similar to large clusters and the thin film electrode (**Figure 4.8**). However, it remains unclear to what extent a single anomalous particle impacts the kinetics and reversibility of an entire cluster.

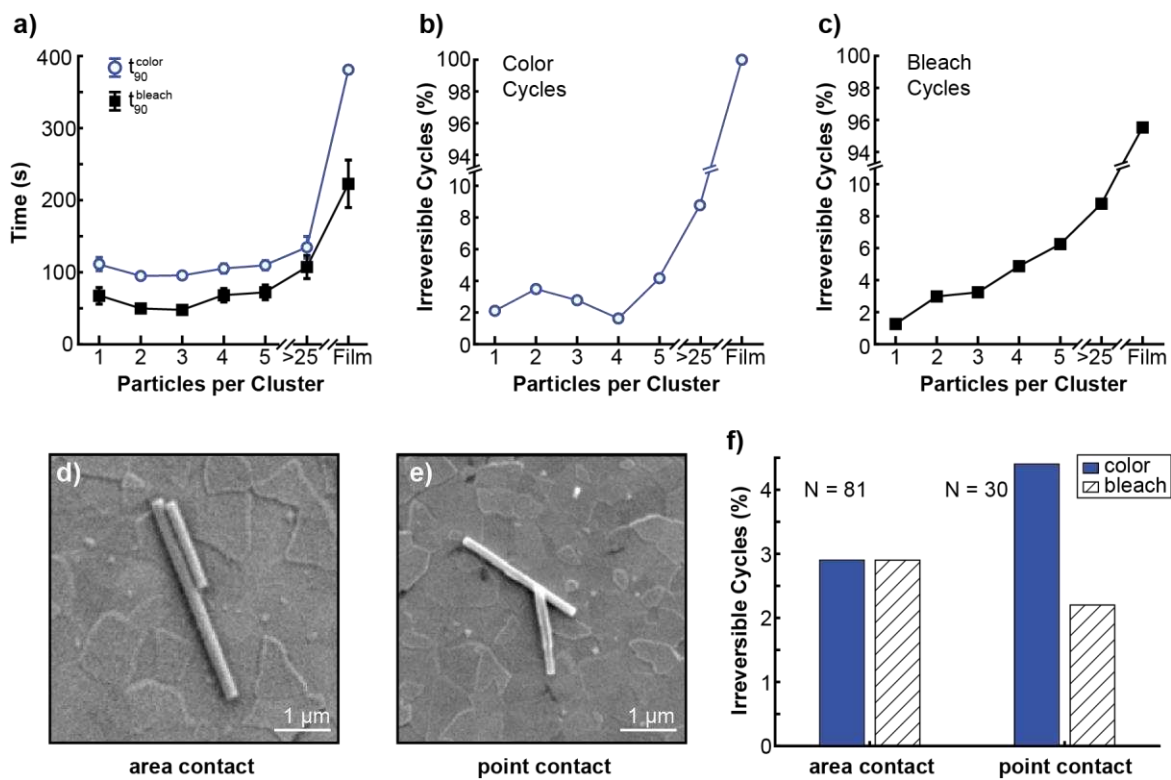


Figure 4.16 – Role of particle-particle interactions on electrochromic dynamics and reversibility. a) t_{90}^{color} and t_{90}^{bleach} versus particle cluster size. Fraction of irreversible (b) bleaching and (c) color cycles versus particle cluster size. The total number of clusters analyzed for sizes 2, 3, 4, 5, and >25 were 134, 72, 41, 32, and 19, respectively. Error bars in (a-c) represent the standard error of the mean. (d-e), SEM image of a two-particle cluster with side-by-side (area contact) configuration and top-and-bottom (point contact) configuration. F) Fraction of irreversible coloration and bleaching cycles for 81 side-by-side clusters (243 total cycles) and 30 top-and-bottom clusters (90 total cycles).

While tinting rates are independent of particle cluster size in the few particle regimes, the frequency of irreversible bleaching cycles increases monotonically with particle-particle interactions (**Figure 4.16b**). In other words, large particle clusters remain tinted following an anodic polarization treatment. This persistent tinting effect has been attributed to ion trapping in WO_3 thin films.¹⁰⁷ For these h- WO_3 nanorods,

the irreversible bleaching effect onsets for two particle-sized clusters due to (Li-W^{5+}) color centers that remain trapped at the nanorod-nanorod interface. The interfacial trapping sites could be due to Li-ion insertion at W=O surface sites on neighboring particles¹⁰⁸, leading to a more stable LiO_x -type interaction. While the exact trapping site is currently unknown, the results show that extrinsic ion trapping sites are introduced at particle-particle interfaces; the trapping site is not intrinsic to the nanorod. On the other hand, electrochromic coloring reversibility is independent of particle-particle interactions in the single and few particle cluster regimes and then abruptly increases for large clusters and the thin film electrode (**Figure 4.16c**). This trend could be due to the trapped (Li-W^{5+}) color centers at particle-particle interfaces that decrease the number of available Li-ion binding sites in consecutive cycles.

To explore how interfacial contact area between nanorods influences electrochromic reversibility, electrochromic reversibility of two-particle clusters with area versus point contact configurations were considered. **Figure 4.16d** shows a representative SEM image of a two-particle cluster where the nanorods align in a side-by-side configuration. **Figure 4.16e** shows a two-particle cluster in a top-and-bottom configuration where one nanorod lays on top of another particle. The side-by-side configuration has a larger particle-particle contact area than the top-and-bottom configuration. Two-particle clusters with side-by-side contacts exhibit less irreversible coloration and more irreversible bleaching behavior than clusters with point contacts (see blue bars versus patterned white bars in **Figure 4.16f**). We attribute the increase in irreversible electrochromic behavior to the large interfacial contact area that introduces more extrinsic ion trapping sites between two nanorods. The coloration reversibility difference between the different cluster configurations is likely due to differences in the electron injection pathway. The electron injection pathway for the side-by-side configuration is similar to isolated nanorods; the ITO electrode contacts each nanorod in the cluster along the entire nanorod sidewall (**Figure 4.16a**). The pathway for the top-and-bottom configuration occurs at the nanorod end points (either at the nanorod-nanorod interface or the ITO-nanorod interface). It is possible that electron injection efficiency at the nanorod-nanorod interface decreases with cycle number due to the accumulation of trapped ions solid-solid interface.

Two-particle clusters with large area contacts modulate from the bleached state to the colored state more reversibly than from the colored state to the bleached state (**Figure 4.16f**). The opposite effect for two-particle clusters with point contacts was observed; the cluster modulates from the colored state to the bleached state more reversibly than from the bleached state to the colored state. The exact origin of these trends is currently unknown since the ion trapping sites and mechanisms are likely different in the coloring and bleaching processes.¹⁰⁹ It is possible that the different particle-ITO and particle-particle contacts for each cluster configuration influence the coloration and bleaching reversibility differently.

4.2.4 Material Insight from Cyclic Voltammetry

In a typical CV experiment, the EM-CCD camera acquires images at 10 frames per second while the potentiostat applies a potential sweep at 10 mV/s. First, we compared the OD response of 38 objects on the ITO electrode to the total charge passed by all WO₃ nanoparticles on the ITO electrode (**Figure 4.17a**). The OD data reports on the cumulative sum of color centers in single nanorods and nanorod clusters. Upon sweeping the electrode potential from 0.0 V to the switching potential $E_{\lambda} = -1.0$ V, the total charge passed increases sharply at about -0.6 V (black line in **Figure 4.17a**). Since control experiments with bare ITO electrodes showed no significant charge accumulation over the same range, the charge passed during the potential sweep can be attributed to Li-ion insertion in WO₃ particles (Equation 2-1). On the other hand, the OD response increases sharply at about -0.4 V. Thus, the onset for (W⁵⁺-Li⁺) color center formation occurs 200 mV more positive than the sharpest increase in total charge passed in the cell.

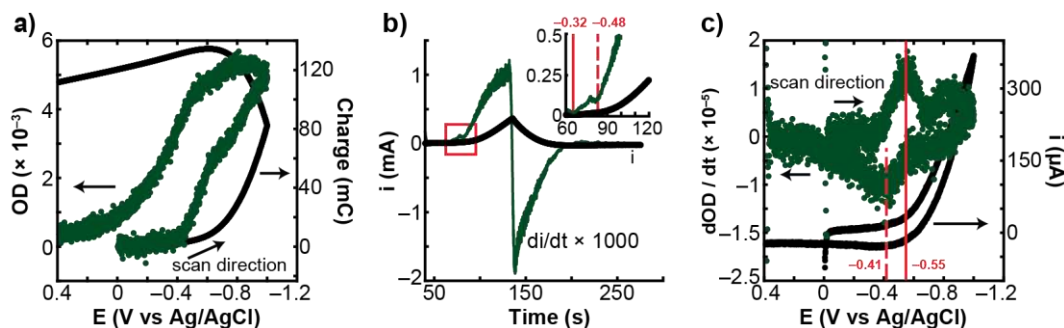


Figure 4.17 – Comparison of conventional and electro-optical cyclic voltammetry. a) Single object optical density measurements (left axis) and ensemble-level total charge passed (right axis) plotted versus

the applied potential from a CV at 10 mV / s. The OD data represents the average response from 38 objects (single particles and clusters). b) Electrochemical current (i , black line) and its derivative (di/dt , green line) versus time during the CV measurement. The inset shows a zoomed-in region of the data to illustrate the rise of the derivative signal. c) Comparison of the optically detected current (dOD/dt , green data, left axis) and i (right axis, black line) versus the applied electrochemical potential.

To confirm that the OD response stems from a faradaic process, the change in the electrochemical current versus time data was examined. **Figure 4.17b** shows the electrochemical-time response ($i-t$) (black circles) and its derivative (di/dt) (green line) during the CV measurement. The di/dt data is approximately 0 until $t = 60$ s because the non-Faradaic double layer charging current in a CV experiment quickly reaches a steady state value. Then, at 63 s (-0.32 V), the di/dt data shows a small, positive onset feature followed by another large positive onset feature at 82 s (-0.48 V, **Figure 4.17b**, inset). Since the OD onset in **Figure 4.17a** occurs between those potentials, the OD increase is attributed to a faradic charge transfer reaction that produces an optically active color center in the WO_3 material ($W^{5+}-Li^+$). On average, additional cathodic charging of the WO_3 nanorods at potentials more negative than -0.6 V does not cause additional optical density changes. Since more charge is inserted into the WO_3 particles without a corresponding increase in OD, then that charge is likely inserted into optically inactive trigonal cavity (TC) sites in the $h-WO_3$ particles, or reduced W^{5+} sites that do not produce a color change.^{52,54} A similar trend is observed upon sweeping anodically from E_λ to $+0.4$ V. The total charge passed increases to a maximum value of 135 mC at -0.62 V and then decreases monotonically. In contrast, the OD response shows a small peak-like feature at -0.8 V before decreasing rapidly for $E > -0.48$ V. These data indicate that the total number of ($W^{5+}-Li^+$) color centers decreases before the majority of charge in the WO_3 particles decreases. This effect is likely due to Li-ion extraction from optically active hexagonal window (HW) and square window (SW) sites before the optically inactive TC sites.^{52,54}

Figure 4.17c compares the electrochemical current-potential curve (black trace) to the particle-averaged optically-detected current (dOD/dt) data (green trace). The dOD/dt data during the cathodic and anodic potential sweeps represents the rate of ($W^{5+}-Li^+$) color center formation. In the cathodic scan of the CV experiment, the electrochemical current change occurs 90 mV more positive (**Figure 4.17a**) than the

electro-optical change. The positive onset is likely due to Li-ion insertion at TC sites.^{52,54} Thus, the dOD/dt data revealed underlying processes that are hidden in electrochemical data alone: the initial charge injection process in these $h\text{-WO}_3$ nanorods does not contribute to electrochromism.

The electro-optical response of single particles and particle clusters were analyzed separately to deconvolute their contributions to the ensemble-level responses in **Figure 4.17**. Correlated SEM imaging is necessary to distinguish single particles from particle clusters. **Figure 4.18a-c** shows the dOD/dt responses of three single particles and their corresponding SEM images (**Figure 4.18a-c**, right panels). Two particles exhibit cathodic and anodic dOD/dt peaks that are separated by 57 mV and 36 mV, respectively (**Figure 4.18a-b**). The $(i_{OD,c}/i_{OD,a})$ ratio for the same two particles are 1.3 and 1.4, which are lower than the ensemble-average value in **Figure 4.17c** ($i_{OD,c}/i_{OD,a} = 1.5$). Peak ratios greater than one indicate that (Li- W^{5+}) color centers remain in the particles after the anodic scan.

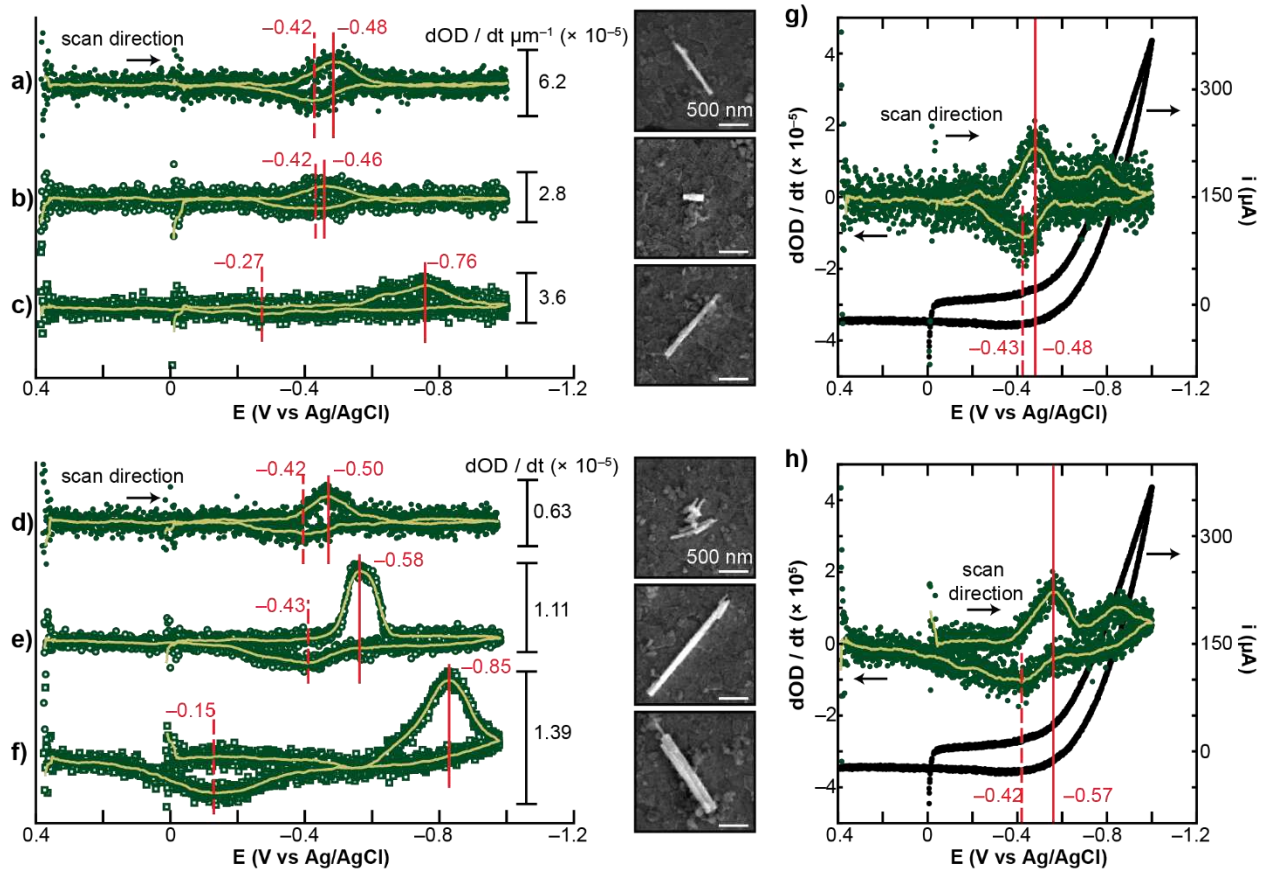


Figure 4.18 – Electro-optical imaging of single nanoparticle voltammetry. a-c) Optically detected current, dOD/dt (green data points), versus applied electrochemical potential for three individual nanorods. The yellow line represents a 5-point smooth to show the general trend. Right panels represent SEM images of the single particles. d-f) same as (a-c), but for particle clusters. g) Single particle-averaged dOD/dt data from the three particles in (a-c) compared to the ensemble-average electrochemical current (black line) that was measured from the entire cell. h) Particle cluster-averaged dOD/dt data from 10 individual clusters compared to the ensemble-average electrochemical current.

The particle in **Figure 4.18c** exhibits significantly different dOD/dt behavior than the other single particles. The cathodic dOD/dt peak appears at significantly more negative potentials (by 350 mV), the peak splitting is approximately 480 mV, and $i_{OD,c}/i_{OD,a} = 2.5$. The significant peak shift on the cathodic scan suggests that there is a large overpotential for the formation of $(W^{5+}-Li)$ color centers. The significantly larger peak splitting and $i_{OD,c}/i_{OD,a}$ values indicate that the nanorod in **Figure 4.18c** exhibits significantly more irreversible electrochemical behavior than the other particles. The irreversible behavior could be due to atomic-scale features on the particle surface that are hidden in the SEM images. High resolution TEM images (**Figure 4.10**) reveal the surface structural heterogeneity of these $h-WO_3$ nanorods. The irregular

surface structure exposes more and more HW and TC sites (OD active and inactive sites, respectively) that could lead to significant particle-to-particle OD heterogeneity. Another possible explanation for the irreversible electrochemical behavior is that there is a particle-dependent contact resistance at the particle/ITO interface that could induce a larger potential drop for some particles. In this scenario, an additional driving force is needed to drive the electrochemical reaction in Equation 2-1 because some fraction of the applied potential drops across the particle/ITO interface. The OD onset could occur at more negative potentials for those particles with a significant contact resistance. In summary, single nanoparticle-level measurements reveal the influence of particle-averaging effects on the apparent onset potential and peak currents in optically detected CVs. Particle-dependent behaviors cause optically detected CV peaks to broaden and shift; these behaviors are hidden in ensemble-average measurements.

Comparing the electro-optical response of single particles to particle clusters reveals particle-particle impact on ion insertion dynamics. **Figure 4.18d-f** shows dOD/dt responses of three particle clusters and their corresponding SEM images. Their dOD/dt responses represent three different behaviors that were observed from 10 total particle clusters. The dOD/dt response in **Figure 4.18d** exhibits a symmetric peak shape, small peak separation, and peak potentials that are consistent with single particles. This single particle-like behavior was observed for 2 of 10 particle clusters. On the other hand, the dOD/dt response of the particle cluster in **Figure 4.18e** shows widely separated asymmetric peaks and a large $i_{OD,c}/i_{OD,a}$ ratio (2.9). This irreversible behavior was observed most often for particle clusters (6 of 10). The third type of dOD/dt behavior is shown in **Figure 4.18c** and is characterized by significant irreversible behavior (i.e., $i_{OD,c}$ occurs at significantly more negative potentials than the ensemble-average value and the peak splitting is 500 mV, $i_{OD,c}/i_{OD,a}$ of 2.2). In summary, the electro-optical behavior of nanoparticle clusters can mimic that of single particles. However, on average, the peak potentials and peak separations of particle clusters are more heterogeneous than that of single particles.

Figure 4.18g-h illustrates the impact of particle-averaging on the electro-optical response by comparing the single particle-average and cluster-averaged dOD/dt . The single particle-average dOD/dt

response exhibits a quasi-reversible wave with an $E_{1/2}$ of -0.46 V and a small second peak with a peak potential of -0.81 V. The quasi-reversible wave occurs 90 mV more positive than that of the particle-average response in **Figure 4.18e** (-0.48 V vs -0.57 V). The more positive peak position indicates that, on average, a lower driving force is required to drive the electrochromic reaction in single particles than in particle clusters. The second peak in the single particle-average data is due to particle averaging effects (i.e., the particle in **Figure 4.18c**) rather than a second electrochromic reaction. The same multi-peak effect appears in the electro-optical response of the cluster-averaged data (**Figure 4.18h**). In general, the electro-optical behavior of particle clusters is more irreversible than single particles (larger peak separation, $E_{1/2}$ of -0.49 V and larger $i_{OD,c}/i_{OD,a}$ ratio 1.75). The irreversible behavior is likely due to particle-particle interfaces that trap Li-ions and impede electron/ion transport. The broad waves for the particle clusters could be due to surface sites at particle-particle interfaces that have different redox potentials than intrinsic surface sites.

4.3 Conclusion

In summary, measurements reveal underlying electro-optical processes that contribute to performance heterogeneity across large area electrochromic nanoparticle films. Importantly, the electro-optical signal is de-coupled from the electrochemical signal and allows for elucidation of underlying electrochemical processes that are hidden in ensemble-level measurements. First, the particle-dependent waiting time for coloration contributes to a delay time for window tinting and diminishes electrochromic coloration efficiency. The overall performance effect is that the window tints gradually in space and time as particles stochastically switch one-by-one from the transparent to colored state. Second, individual nanoparticle building blocks can tint up to 400% faster than a nanoparticle film assembled from the same building blocks. Finally, ion trapping sites are introduced at particle-particle interfaces that cause long-term optical performance degradation. A mesoporous thin film architecture is proposed, where fast-switching electrochromic nanoparticles are deposited onto a high surface area transparent conductor (**Figure 4.19**).

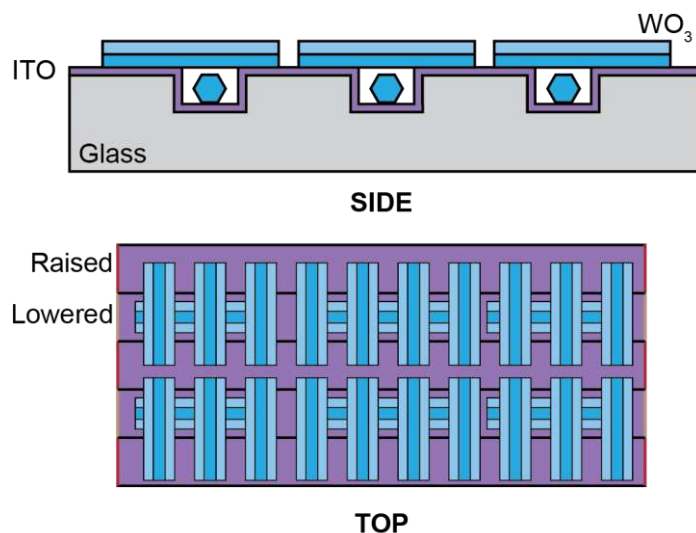


Figure 4.19 – Proposed smart window device architecture for improved performance. Side and top views of isolated WO_3 NRs deposited on a high surface area transparent conductor (e.g., ITO). The ITO/ WO_3 layers could be stacked between layers of liquid or solid-state electrolyte.

Figure 4.19 shows a proposed thin film architecture where fast-switching electrochromic $h\text{-WO}_3$ NRs are deposited onto a high surface area transparent conductor. The ITO/ WO_3 layers could be stacked between layers of liquid or solid-state electrolyte to maximize optical density. The layer stacking procedure should be optimized to avoid particle-particle interactions, thereby increasing electrochemical ion insertion/extraction reversibility. This strategy would enable high light absorption with well separated WO_3 particles, thereby avoiding deleterious particle-particle interactions. This strategy would enable total light absorption with single layers of WO_3 particles, thereby avoiding deleterious particle-particle interactions. Single particle electrochromism imaging approach can be generally applied to transition metal oxides^{39,110}, graphite^{33,40} and $\text{Ni}(\text{OH})_2$ battery materials⁴¹ whose optical properties change during ion insertion. Single particle electro-optical imaging of ion insertion/extraction processes can guide applied research related to batteries, fuel cells, electrochemical capacitors, and sensors.

CHAPTER 5: SURFACE FACET-DEPENDENT ELECTROCHROMIC PROPERTIES OF WO₃ NANOROD THIN FILMSⁱⁱⁱ

The influence of nanoparticle surface facets on electrochromic properties remains largely unexplored in nanostructured “smart” materials. The particle length dependent optical change is a major result discussed in CHAPTER 4: INVESTIGATION OF STRUCTURE-PROPERTY RELATIONSHIPS IN HEXAGONAL WO₃ NANORODS. Long nanorods tended to have more step edge defects which would expose a different crystalline facet on the surface, leading to the hypothesis that facets have an impact on electrochromic performance.

Facet-dependent electrochromism has been studied in nickel oxide because the coloration mechanism is thought to occur through redox chemistry at the NiO surface^{29,30}; changing the surface facet should directly impact tinting and bleaching. The facet orientation alters ion insertion rates because it determines the activation energy for ion diffusion across the interface, which could differ from the bulk.³¹ However, surface facet-dependent electrochromic properties of WO₃ nanoparticles are lacking. In a h-WO₃ battery that also relies on Li-ion insertion, Lian et al. observed that h-WO₃ nanoribbons with an exposed ($\bar{1}20$) plane exhibited superior electrochemical stability relative to particles with (100) planes.³² High resolution electron microscopy analysis suggested that a surface step edge gradient on the long NRs exposed more {001} facets along the length and { $\bar{1}20$ } facets along the width.

Motivated by single particle-level studies^{33,34} and WO₃ battery literature^{24,32,35}, the hypothesis that exposing more { $\bar{1}20$ } facets will improve electrochromic properties and stability of electrochromic h-WO₃ nanorod (NR) thin films is tested. h-WO₃ is a good model system for this study because it does not undergo

ⁱⁱⁱ This chapter contains adaptations from Evans, R. C.; Austin, R.; Miller, R. C.; Preston, A.; Nilsson, Z. N.; Ma, K.; Sambur, J. B. Surface-Facet-Dependent Electrochromic Properties of WO₃ Nanorod Thin Films: Implications for Smart Windows. *ACS Appl. Nano Mater.* **2021**, *4* (4), 3750–3759. <https://doi.org/10.1021/acsnm.1c00215>. citation⁽¹¹⁾. R.C.E. performed experiments, analyzed data, and wrote the manuscript. R.A. synthesized materials and performed experiments. R.C.M. analyzed TEM data and provided valuable insight into the facet assignments. Z.N.N. performed SEM and TEM imaging experiments. A.P. performed SPM experiments. A.P. and K.M. analyzed SPM data. J.B.S. and R.C.E. developed the experimental setup, analyzed data, and wrote the manuscript.

a phase transition⁴⁴ or large volume expansion during lithiation⁴⁵, minimizing the possibility that changes in bulk structure could complicate data interpretation. Two WO₃ NR samples with the same hexagonal crystal structure were synthesized, but one sample exhibited $\{\bar{1}20\}$ facets. In situ electro-optical measurements of ensemble thin films showed that h-WO₃ NR samples with $\{\bar{1}20\}$ facets exhibited lower coloration efficiency (CE), but higher optical modulation stability compared to NR samples with $\{100\}$ and $\{001\}$ facets. The reduced optical density changes in the $\{\bar{1}20\}$ -dominant sample could be due to a greater fraction of optically inactive trigonal cavity sites on the $\{001\}$ end caps. The results indicate surface facet and particle morphology engineering are viable strategies to enhance CE and long-term stability / lifetime in electrochromic thin films for smart window applications and resulted in a publication.¹¹¹

5.1 Results

Nanorods with $\{\bar{1}20\}$, $\{100\}$, and $\{001\}$ facets (**Figure 5.1a**) were prepared via a hydrothermal reaction as modified from Ding et al.¹¹² First, 0.415 g ammonium tungstate (Sigma) were dissolved in 13.8 mL of 18.2 MΩ-cm (MilliPore NanoPure) water and the pH adjusted to 1.5 with dropwise addition of ~3M HCl under continuous stirring (>300 rpm). The solution was then transferred to a 23 mL Parr Instruments Acid Digestion hydrothermal reactor (model number 4979) and placed in an oven at 180 °C for 24 hours, then removed and cooled to room temperature in a fume hood. The slightly yellow product was filtered and washed twice with 18.2 MΩ-cm water and twice with reagent grade ethanol (Fisher Scientific). The solid product was then dried at 80 °C under vacuum overnight followed by heating at 300 °C in air for 5 hours before being stored in reagent grade ethanol. The sample undergoes structural changes after two months; unidentified peaks in PXRD appear at this stage. The median and median variance of particle lengths and widths were 120 ± 50 nm and $20 \text{ nm} \pm 5$ nm, respectively, as measured from SEM images. Nanorods with $\{100\}$ and $\{001\}$ facets were prepared as in 3.1 Material Synthesis (and were the same as used in used for the study in CHAPTER 4: and CHAPTER 6:). Briefly, heating an aqueous solution of 0.15 M sodium tungstate precursor in the presence 0.26 M NaCl produced h-WO₃ NRs with $\{100\}$ and $\{001\}$ facets. **Figure**

3.1 is shown again in **Figure 5.1b** for facile comparison. Samples are referred to as $\text{WO}_3\text{-}\{\bar{1}20\}$ and $\text{WO}_3\text{-}\{100\}$, according to the unique or dominant surface facet for each sample.

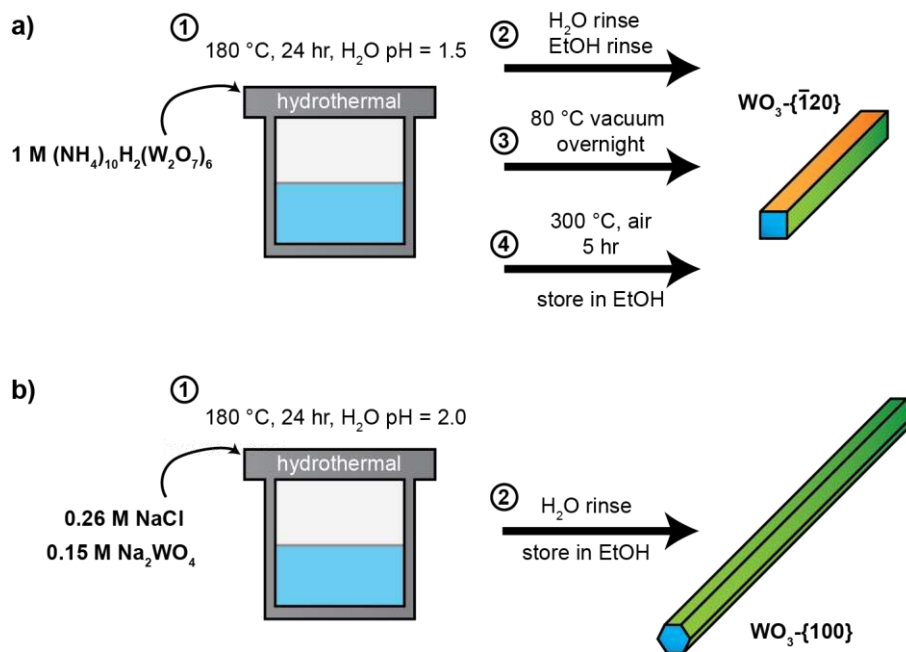


Figure 5.1 – Synthesis and fabrication of h- WO_3 electrochromic samples. Synthesis scheme for (a) $\text{WO}_3\text{-}\{\bar{1}20\}$ NR and (b) $\text{WO}_3\text{-}\{100\}$ NRs.

Figure 5.2a shows the powder X-ray diffraction (PXRD) pattern for the $\text{WO}_3\text{-}\{\bar{1}20\}$ and $\text{WO}_3\text{-}\{100\}$ samples. The diffraction pattern for $\text{WO}_3\text{-}\{\bar{1}20\}$ and $\text{WO}_3\text{-}\{100\}$ were indexed to hexagonal WO_3 ($P6_3/mcm$, JCPDS 04-007-2322 and $P6/mmm$, JCPDS 00-033-1387, respectively). The PXRD peak heights and widths differ between the two samples, suggesting preferred facet orientation among the particles in each sample. The high intensity (100) and low intensity (002) peak for $\text{WO}_3\text{-}\{100\}$ indicate particle growth along the [001] direction with exposed $\{100\}$ symmetry related planes.⁴⁶ However, the PXRD data alone is insufficient to reveal the exposed planes and growth direction of $\text{WO}_3\text{-}\{\bar{1}20\}$.

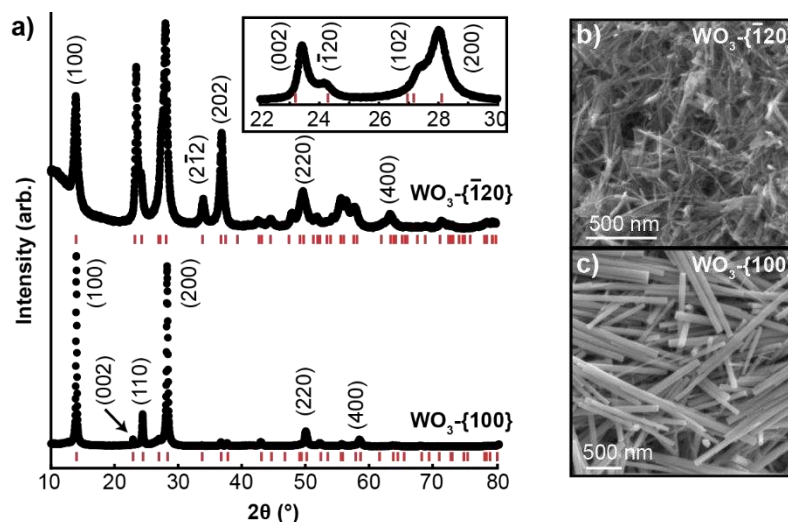


Figure 5.2 – Crystal structure and morphology of h-WO₃ NRs. a) PXRD patterns for WO₃-{ $\bar{1}20$ } and WO₃-{100} samples (black data points). Red dashes indicate reference peak patterns (top: P6/mmm, JCPDS 04-007-2322 WO₃-{ $\bar{1}20$ }; bottom: P6/mmm, JCPDS 00-033-1387 WO₃-{100}). b-c) Representative SEM images of b) WO₃-{ $\bar{1}20$ } and c) WO₃-{100} films.

Scanning electron microscopy (SEM) images of the WO₃-{ $\bar{1}20$ } and WO₃-{100} samples exhibit a one-dimensional particle morphology (**Figure 5.2b,c**). The median and variance length (l) and width (w) values for the WO₃-{ $\bar{1}20$ } and WO₃-{100} samples were $l = 120 \text{ nm} \pm 50 \text{ nm}$ and $w = 20 \text{ nm} \pm 5 \text{ nm}$ and $l = 980 \text{ nm} \pm 480 \text{ nm}$ and $w = 71 \text{ nm} \pm 15 \text{ nm}$, respectively. The smaller WO₃-{ $\bar{1}20$ } NRs contribute to peak broadening in the PXRD data in **Figure 5.1a**. The aspect ratio of both samples were >1 and <20 and, therefore, the particles can be categorized as NRs.¹¹³

The NR growth direction and surface facets were determined using high resolution transmission electron microscopy (HRTEM). **Figure 5.3a,b** show HRTEM images for two different NRs from the WO₃-{ $\bar{1}20$ } sample. Each NR in the film is a single crystal. The lattice spacings in the HRTEM image produce bright spots in the fast Fourier transform (FFT) image (**Figure 5.3a,b**-inset). The distance between the bright spots in the FFT image correlates to a lattice spacing of 3.73 Å, which can be assigned to planes of atoms along the [001] growth direction. Lattice spacings of 6.31 Å (**Figure 5.3a**) or 3.64 Å (**Figure 5.3b**) perpendicular to the growth direction each appear roughly half the time and imply rectangular prism geometry; rotating the particle 90° changes the plane of atoms perpendicular to the TEM grid.

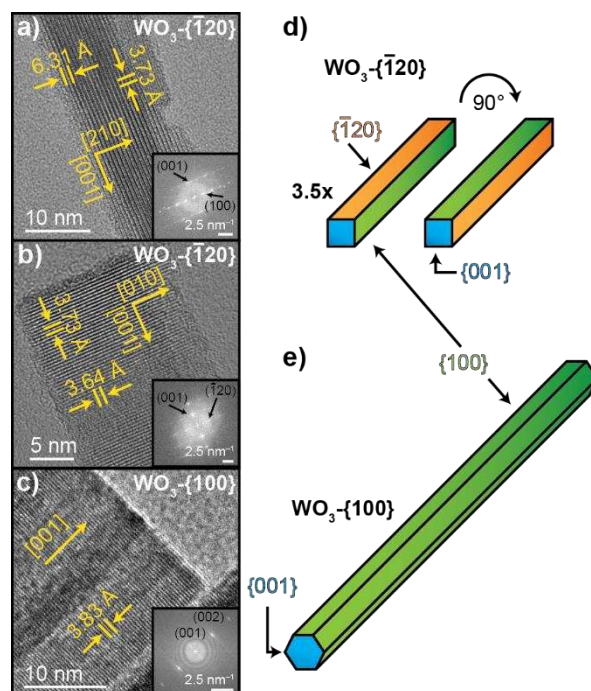


Figure 5.3 – Surface facet characterization and illustration. a) HRTEM image of a single NR from the WO_3 - $\{\bar{1}20\}$ sample, observed via a top-down view of the $\{100\}$ surface. b) HRTEM image of a different single NR in the WO_3 - $\{\bar{1}20\}$ sample, observed via a top-down view of the $\{\bar{1}20\}$ surface. c) HRTEM of a single NR in the WO_3 - $\{100\}$ sample. Insets of (a-c) represent FFT images. d-e) Cartoon illustration of WO_3 - $\{\bar{1}20\}$ and WO_3 - $\{100\}$ samples drawn to scale (note: 3.5x for WO_3 - $\{\bar{1}20\}$).

Figure 5.3c shows a HRTEM image of a single NR in the WO_3 - $\{100\}$ sample. The FFT analysis revealed a lattice spacing of 3.83 Å with no distinct perpendicular spacing, indicating growth along the $[001]$ direction, which is in agreement with literature for WO_3 NRs grown as hexagonal prisms.⁴⁶ In summary, these hydrothermal reactions produce 1D hexagonal WO_3 NRs with different length, width, and exposed surface facet orientation.

The cartoon illustrations in **Figure 5.3d,e** compare the particle morphology and surface facets of the WO_3 - $\{\bar{1}20\}$ and WO_3 - $\{100\}$ samples. The NRs in the WO_3 - $\{\bar{1}20\}$ sample have a square rectangle morphology. The end caps are made from $\{001\}$ planes and the sidewalls are made from $\{100\}$ and $\{\bar{1}20\}$ planes. The $\{\bar{1}20\}$ planes account for 45% of the total NR surface area and the particles likely lay with the long axis parallel to the transparent electrode surface. In this configuration, either the $\{\bar{1}20\}$ or $\{100\}$ facet contacts the ITO electrode and the majority of the NR surface area exposed to the electrolyte is from the

remaining facets (either $\{\bar{1}20\}$ or $\{100\}$). This configuration is potentially significant for electrochromic thin film electrodes because the facet in contact with the ITO electrode participates in electron transfer whereas those facets in contact with electrolyte undergo interfacial ion insertion processes; the contact resistance and activation energies of these processes could be facet-dependent.^{114,115} On the other hand, single NRs in the WO_3 - $\{100\}$ sample exhibit a hexagonal prism morphology, in agreement with literature reports.⁴⁶ The sidewalls are composed of symmetrically equivalent (100) , (010) , and $(1\bar{1}0)$ planes (i.e., $\{100\}$ planes) and the end caps are composed of $\{001\}$ planes. These particles also likely lay with the long axis parallel to the ITO electrode. However, the $\{100\}$ facets are always in contact with the substrate and the electrolyte. Hence, the exposed facets of these two NR samples enables us to study the influence of the $\{\bar{1}20\}$ facet on electrochromic performance of h- WO_3 NRs.

Note that these facet assignments can be denoted using several different Miller Indices due to the symmetry of a hexagonal crystal system. **Figure 5.4** and **Table 1** describe the alternative symmetry related planes for a hexagonal system using WO_3 corner sharing octahedra as an example.

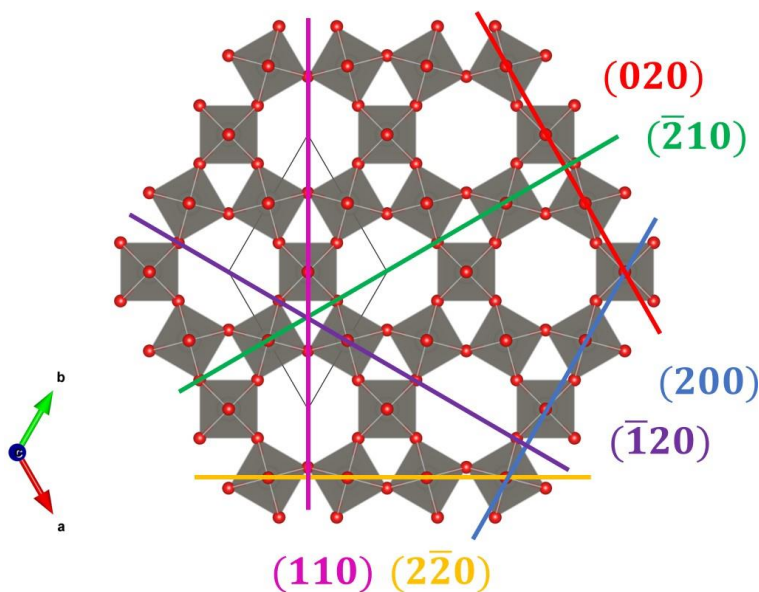


Figure 5.4 – Illustration of symmetry related planes in the hexagonal WO_3 system.

Hexagonal systems contain many symmetry related planes. Though these planes can be referred to differently (e.g. (010) vs (100), see **Table 1**) they contain the same atoms in the same arrangement (**Figure 5.4**). In this manuscript we group all planes (010), (100) and ($1\bar{1}0$) all into the notation $\{100\}$. Similarly, we group all planes that could be identified as ($\bar{2}10$), ($\bar{1}20$), (110) into the notation $\{\bar{1}20\}$.

Table 1 – Table of the lattice planes that exist in parallel or perpendicular to the hexagonal sidewalls of the nanorod.

Planes to hexagon sides	Planes \perp to hexagon sides
(010)	($\bar{2}10$)
(100)	($\bar{1}20$)
($1\bar{1}0$)	(110)

Each row contains the planes that are perpendicular to one another. The left column contains planes that expose hexagonal faces while the corresponding pairs in the right column contains the corresponding planes that have the hexagonal vertices

$\text{WO}_3\text{-}\{\bar{1}20\}$ and $\text{WO}_3\text{-}\{100\}$ NR thin films were prepared by drop casting 3 mg of sample on ITO substrates. Scanning probe microscopy measurements revealed the film thicknesses were 474 ± 170 nm and 1315 ± 300 nm for $\text{WO}_3\text{-}\{\bar{1}20\}$ and $\text{WO}_3\text{-}\{100\}$, respectively (**Figure 5.5**). Thin films of equal thickness were not prepared on ITO substrates, likely due to the different wettability of the NRs on the ITO surface. **Figure 5.2b,c** shows representative SEM images of the film morphology, where the 1D NRs lie with their long axes parallel to the ITO substrate.

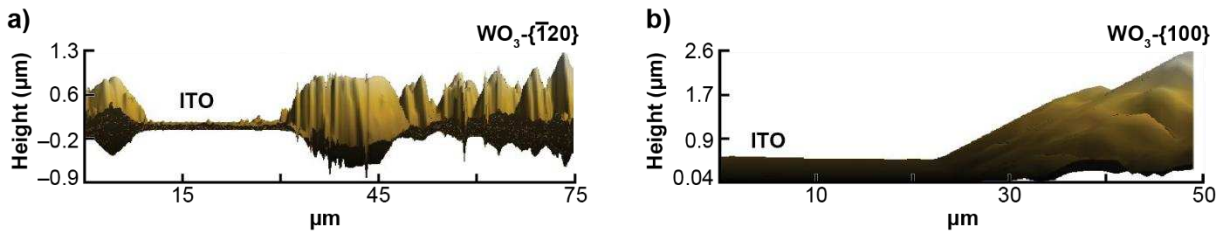


Figure 5.5 – Scanning probe microscopy analysis of NR films. a-b) Representative height profiles showing the height change from the bare ITO substrate to $\text{WO}_3\text{-}\{\bar{1}20\}$ and $\text{WO}_3\text{-}\{100\}$ NR films, respectively.

Next, we evaluated the electrochromic and electrochemical properties of the thin film electrodes. The optical density (OD) at 940 nm was measured while cycling the films between -1.0 V for 30 s and 0.5 V for 30 s in 1 M LiClO_4 (all potential values refer to the Ag/AgCl reference electrode). **Figure 5.6** shows transmission spectra before and after cycling. Optical density at 940 nm was measured as described in Equation 2-3.

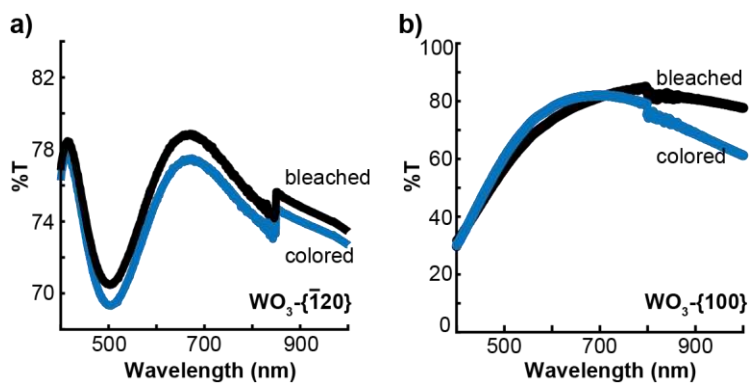


Figure 5.6 – Facet dependent transmission spectra. Percent transmission spectra for (a) $\text{WO}_3\text{-}\{\bar{1}20\}$ and (b) $\text{WO}_3\text{-}\{100\}$ films one cycle coloring at -1.0 V and bleach at 0.5 V vs Ag/AgCl .

Figure 5.7a,b shows the $\Delta\text{OD}(t)$ behavior for $\text{WO}_3\text{-}\{\bar{1}20\}$ and $\text{WO}_3\text{-}\{100\}$ films for cycles 3-5 and 498-500. The initial electrochromic response was not surface facet-dependent and, therefore, cycle 1-2 data was omitted from **Figure 5.7a,b** to emphasize the electrochromic behavior after repetitive, long-term cycling.

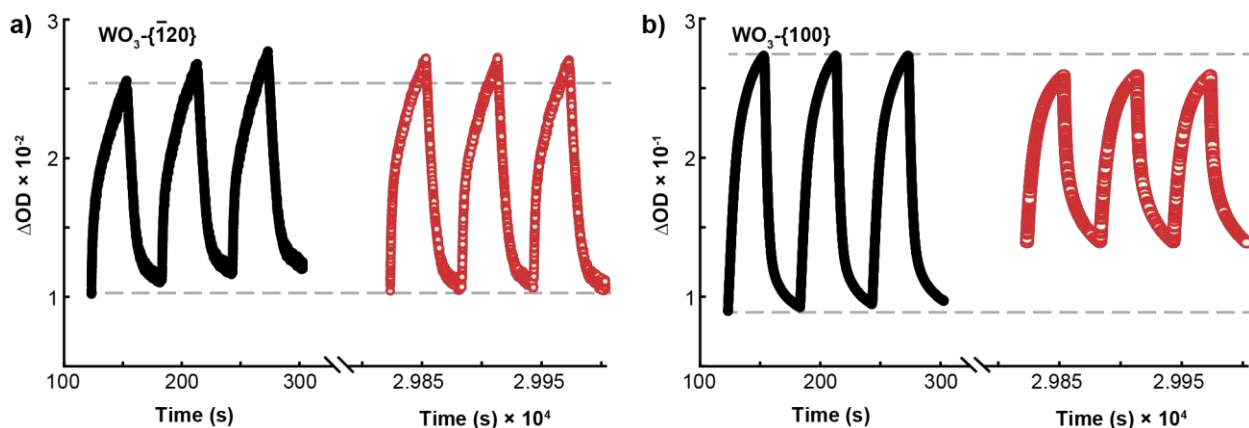


Figure 5.7 – Optical changes at 940 nm. a) ΔOD changes versus time of $474 \text{ nm} \pm 170 \text{ nm}$ $\text{WO}_3\text{-}\{\bar{1}20\}$ films for cycles 3-5 (black filled circles) and 498-500 (red open circles). b) same as (a) but for a 1315 nm

± 300 nm $\text{WO}_3\text{-}\{100\}$ sample. Horizontal gray lines represent maximum and minimum ΔOD values in cycle 3 and serve as a visual guide for differences between ΔOD in early versus late cycles.

Initial (de)lithiation of both samples produced irreversible electrochromic behavior (**Figure 5.8**) that could be attributed to ion trapping inside the WO_3 bulk, as discussed and quantified below.^{18,39,40}

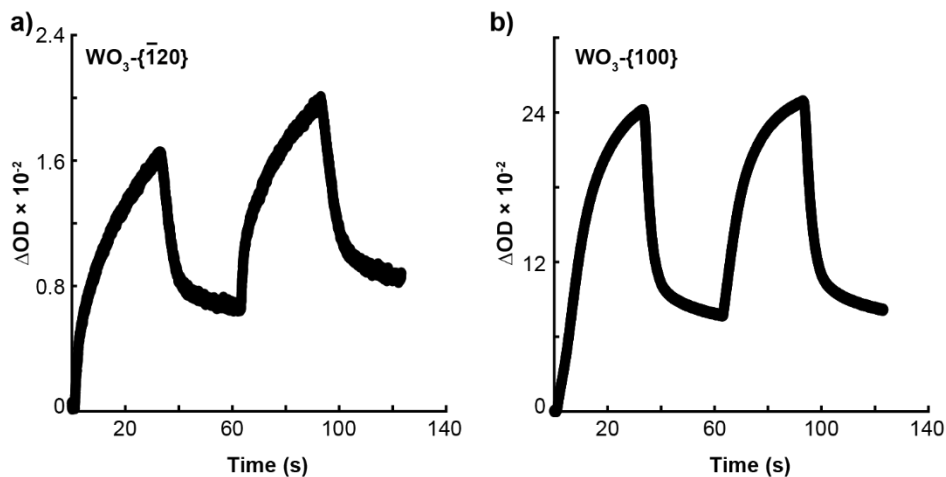


Figure 5.8 – Facet-dependent electrochromic properties. a) Thickness corrected OD changes, ΔOD_d , versus time of $474 \text{ nm} \pm 170 \text{ nm}$ $\text{WO}_3\text{-}\{120\}$ films for cycles 1-2 (black filled circles). b) same as (a) but for a $1315 \text{ nm} \pm 300 \text{ nm}$ $\text{WO}_3\text{-}\{100\}$ sample.

The h- WO_3 samples exhibit different OD magnitudes and cycling behaviors. The ΔOD magnitude of the $\text{WO}_3\text{-}\{120\}$ sample is an order of magnitude lower than the $\text{WO}_3\text{-}\{100\}$ sample. One factor that contributes to the large ΔOD magnitude difference is film thickness. The ΔOD magnitude differs by a factor of 3.0-4.5 after correcting for film thickness (**Figure 5.9**).

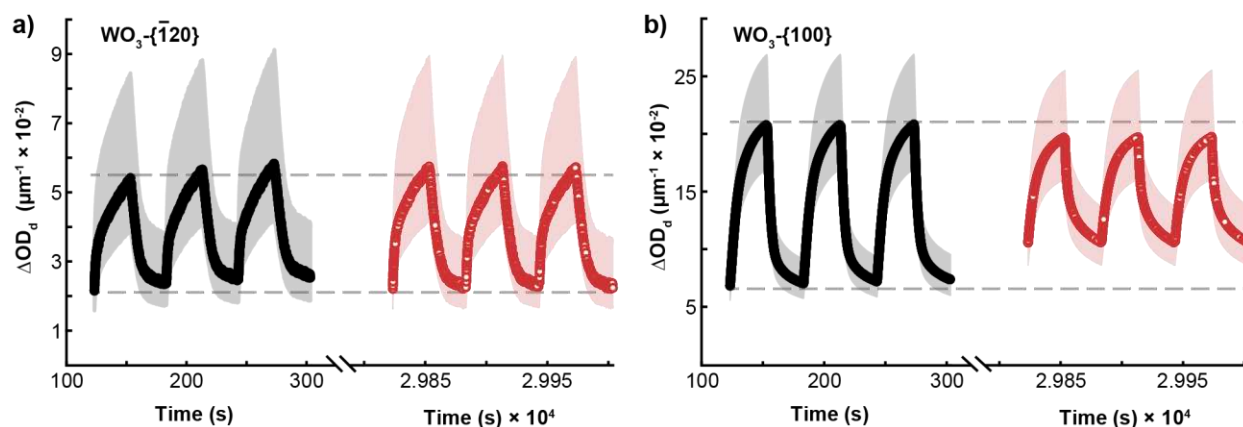


Figure 5.9 – Thickness corrected optical changes at 940 nm. a) ΔOD_d changes versus time of $474 \text{ nm} \pm 170 \text{ nm}$ $\text{WO}_3\text{-}\{\bar{1}20\}$ films for cycles 3-5 (black filled circles) and 498-500 (red open circles). b) same as (a) but for a $1315 \text{ nm} \pm 300 \text{ nm}$ $\text{WO}_3\text{-}\{100\}$ sample. Horizontal gray lines represent maximum and minimum ΔOD_d in cycle 3 and serve as a visual guide for differences between ΔOD_d in early versus late cycles. Opaque areas represent error within one standard deviation.

The time required to reach 90% of maximum ΔOD during the cathodic coloration pulse (t_{90}^{color}) is $\sim 20 \text{ s}$ for both films and the time required to decay by 90% from maximum ΔOD during the anodic bleach pulse (t_{90}^{bleach}) is $\sim 15 \text{ s}$ for both films (**Table 2**).

Table 2 – Response times of WO_3 NR films. t_{90}^{color} is the time required to reach 90% of maximum ΔOD during the cathodic coloration pulse. t_{90}^{bleach} is the time required to decay by 90% from maximum ΔOD during the anodic bleach pulse.

	t_{90}^{color}	t_{90}^{bleach}
$\text{WO}_3\text{-}\{100\}$	$18 \text{ s} \pm 0.3 \text{ s}$	$17 \text{ s} \pm 1.0 \text{ s}$
$\text{WO}_3\text{-}\{\bar{1}20\}$	$23 \text{ s} \pm 0.5 \text{ s}$	$13 \text{ s} \pm 0.6 \text{ s}$

Hence, the surface facets do not appear to play a major role in ΔOD kinetics. The tinting behavior of the $\text{WO}_3\text{-}\{\bar{1}20\}$ sample does not change after the initial cycle. On the other hand, the maximum ΔOD achieved by the $\text{WO}_3\text{-}\{100\}$ sample during the tinting pulse decreases by 5% after 500 cycles. Then, upon de-lithiation, the $\text{WO}_3\text{-}\{100\}$ sample does not return to the same transparent state (see gray dashed lines in **Figure 5.8**). Specifically, the minimum OD achieved during the bleaching pulse increases by 30% after the

initial cycle. The irreversible behavior of $\text{WO}_3\text{-}\{100\}$ during the bleaching process suggests that more (Li- W^{5+}) color centers remain trapped in the material after anodic polarization cycles.

The difference between the charge inserted during the cathodic coloration pulse and the charge extracted during the anodic bleaching pulse for cycle 3 was calculated to quantify the ion trapping in both films. The difference in charge was -9.63×10^{-3} C and -2.71×10^{-2} C for $\text{WO}_3\text{-}\{\bar{1}20\}$ and $\text{WO}_3\text{-}\{100\}$, respectively. The negative sign indicates more charge was inserted in the films during the cathodic pulse than extracted during the anodic pulse. Under the assumption that 1 Li-ion inserts in the film per injected electron, then the mole fractions of trapped Li-ions in the films are 0.0015 and 0.0028 for $\text{WO}_3\text{-}\{\bar{1}20\}$ and $\text{WO}_3\text{-}\{100\}$, respectively. Ion trapping is more significant in the $\text{WO}_3\text{-}\{100\}$ sample.

The coloration efficiency (CE) was calculated according to Equation 5-1 to explore the origin of the ΔOD magnitude difference between the two samples.

$$\text{CE} = \Delta\text{OD}/Q \quad \text{Equation 5-1}$$

where Q is the total charge density passed as a function of cathodic polarization time (in units of C/cm^2 ; the area is the geometric area of the film). A large, positive CE value indicates a large optical modulation at 940 nm per number of electrons inserted into the oxide.⁶⁵ CE was determined for each cathodic polarization cycle by fitting ΔOD versus Q with a linear function (**Figure 5.10**).

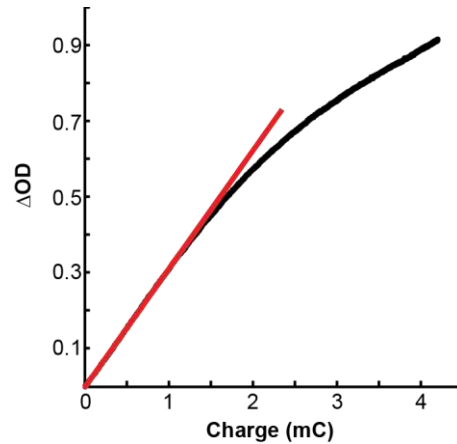


Figure 5.10 – CE fitting. ΔOD versus charge inserted charge density, Q , to determine the coloration efficiency. Linear fit is in red.

Figure 5.11a-b shows CE versus cycle number for the first 30 cycles of each NR film. The CE values of the $WO_3\{-\bar{1}20\}$ and $WO_3\{100\}$ films during the first cycle were $24\text{ cm}^2\text{ C}^{-1}$ and $25\text{ cm}^2\text{ C}^{-1}$, respectively. Upon cycling, the CE of the $WO_3\{100\}$ sample increases steadily with cycle number and plateaus at $80\text{ cm}^2\text{ C}^{-1}$ after 45 cycles (**Figure 5.11c**). This trend indicates that a significant fraction of charge inserted in $WO_3\{100\}$ does not contribute to OD modulation at early cycles. The CE of the $WO_3\{-\bar{1}20\}$ sample increases slowly with cycle number and the relative ΔOD change (optical modulation relative to the first cycle) stays constant after the first cycle. After 500 cycles, the CE value of the $WO_3\{100\}$ sample increased by a factor of 233% whereas the CE value of the $WO_3\{-\bar{1}20\}$ sample only increased by 40%. The large CE increase of the $WO_3\{100\}$ film is accompanied by a continuous decrease in ΔOD (**Figure 5.11b**). Hence, after 500 cycles, the efficiency of optical modulation increased but the film tinted less. The CE of these NR films differ by a factor of 3, but are within the range reported by Besnardiere et al for h- WO_3 nanoparticle films ($11\text{ cm}^2\text{ C}^{-1}$) and Kondalkar et al for a conformal nanostructured h- WO_3 film ($87.23\text{ cm}^2\text{ C}^{-1}$).^{74,116}

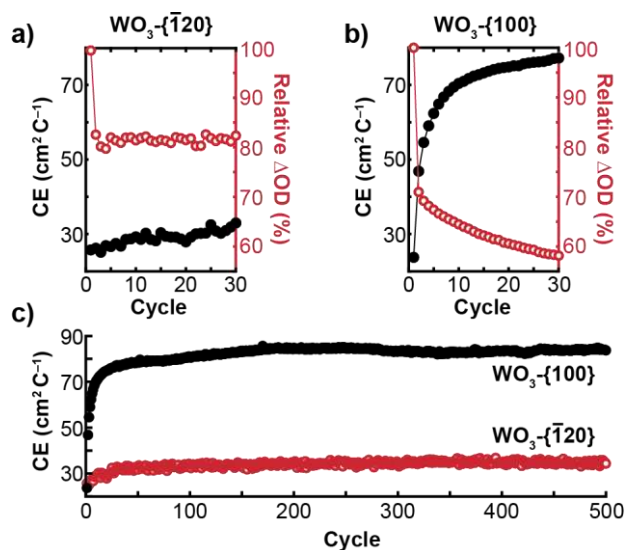


Figure 5.11 – Coloration efficiency of NR samples. a-b) CE (black filled circles) and relative change in ΔOD (open red circles) for $WO_3\{-\bar{1}20\}$ and $WO_3\{-100\}$ for the first 30 cycles. Solid lines are a guide for the eye. (c) CE versus cycle number for $WO_3\{-\bar{1}20\}$ and $WO_3\{-100\}$ films.

The electrical characteristics of the NR film electrodes before and after cycling were characterized to further understand how the surface facets influence electrochromic properties during long-term cycling using electrochemical impedance spectroscopy (EIS). **Figure 5.12a,b** shows Nyquist plots for $WO_3\{-\bar{1}20\}$ and $WO_3\{-100\}$, respectively, before and after cycling.

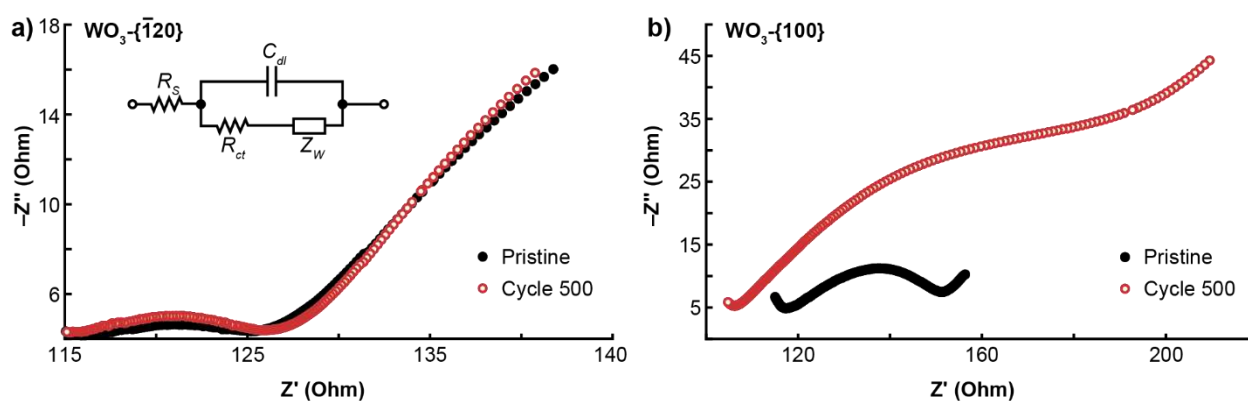


Figure 5.12 – Electrochemical impedance spectroscopy. a-b) Nyquist plot for the $WO_3\{-\bar{1}20\}$ and $WO_3\{-100\}$ samples before and after 500 cycles. Data acquired at -1.0 V vs Ag/AgCl over the range of 20 Hz to 150 kHz. The inset in panel (a) shows the Randle circuit used for fitting EIS data.

Both samples show a semi-circle at high frequencies and a linear response at low frequencies. Interestingly, these features did not change after 500 cycles for $WO_3\{-\bar{1}20\}$ (**Figure 5.12a**). In contrast, the

WO₃-{100} EIS data exhibits significant changes after 500 cycles (**Figure 5.12b**). The data shows a larger semi-circle over the 1700 Hz to 85 Hz frequency range and a shallower slope at low frequencies after 500 cycles, implying larger charge transfer resistance (R_{ct}) and ionic diffusivity. To quantify the changes in EIS data before and after cycling, the Nyquist plots were fit with the Randle's circuit (**Figure 5.12a inset**), which has been used to fit EIS data of electrochromic nanoparticle films,^{67,74,117} yielding R_{ct} and the Warburg diffusion element (Z_w). Note that this equivalent circuit assumes semi-infinite diffusion and a planar electrode surface. Relative trends, rather than absolute numbers, are used to compare the materials since the circuit likely oversimplifies these systems.

Table 3 shows that R_{ct} of the WO₃-{100} sample is initially three-times larger than the WO₃-{ $\bar{1}20$ } sample. The larger R_{ct} could be due to differences in packing density, film thickness, and porosity of the larger NRs. The R_{ct} of the WO₃-{ $\bar{1}20$ } sample does not change after 500 cycles whereas R_{ct} of the WO₃-{100} sample doubles after 500 cycles. In addition, Z_w of the WO₃-{100} quadruples after 500 cycles. The changes in fitting parameters indicate that the WO₃-{100} electrode conducts both electrons and Li-ions less effectively after 500 cycles.

Table 3 – Summary of EIS fit result using a Randle's circuit to fit EIS data in Figure 5.12. Z_w was calculated from the fit Warburg constant at 23 Hz.

	R_{ct} pristine (Ω)	R_{ct} cycle 500 (Ω)	Z_w pristine (Ω)	Z_w cycle 500 (Ω)
WO ₃ -{ $\bar{1}20$ }	7.7 \pm 0.01	8.8 \pm 0.01	23.0 \pm 0.01	22.0 \pm 0.01
WO ₃ -{100}	22. \pm 0.3	49. \pm 0.9	15. \pm 0.4	65. \pm 1

To understand the origin of the optical and electrical properties of the WO₃-{ $\bar{1}20$ } and WO₃-{100} electrodes before and after cycling, we examined the surface chemical composition of pristine and cycled films using X-ray photoelectron spectroscopy (XPS) and time-of-flight secondary-ion mass spectroscopy (TOF-SIMS). **Figure 5.13** compares carbon, lithium, oxygen, and tungsten XPS data for pristine and cycled

WO₃-{ $\bar{1}20$ } and WO₃-{100} films; all data normalized to the W 4f_{7/2} peak. The trends in XPS data before and after cycling were qualitatively similar for both samples. The changes in XPS data before and after cycling the WO₃-{ $\bar{1}20$ } film in 1 M LiClO₄ in propylene carbonate solvent is discussed as a representative example of the surface chemical changes that occur in both h-WO₃ NR film electrodes.

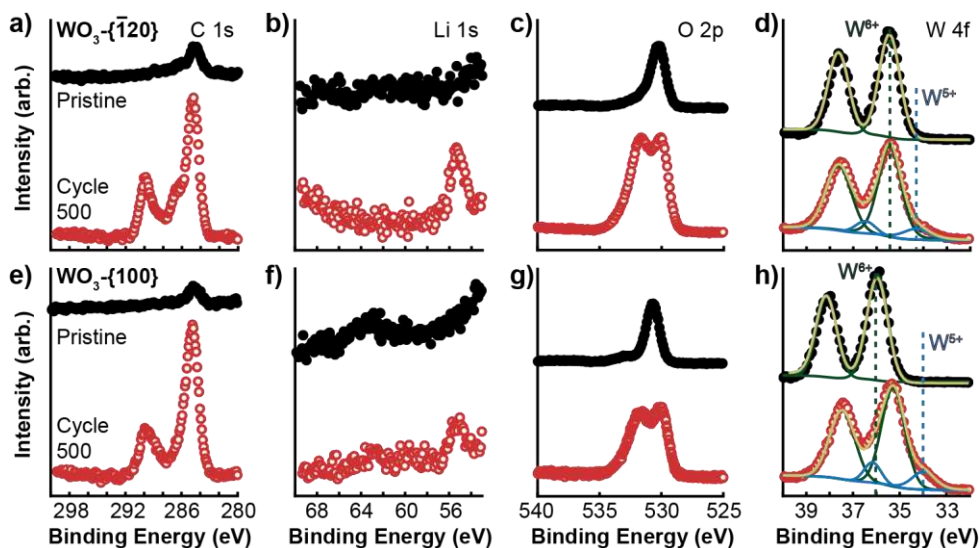


Figure 5.13 – XPS analysis. a-h) XPS data before (black, filled) and after 500 cycles (red, open) for C1s, Li 1s, O 2p, and W 4f regions for WO₃-{ $\bar{1}20$ } and WO₃-{100} films. W 4f data (d,h) were fit to W 4f_{7/2} and 4f_{5/2} peaks at 35.4 eV and 37.6 eV (green), corresponding to W⁶⁺. W 4f_{7/2} and 4f_{5/2} peaks at (d) 34.0 eV and 36.1 eV and (h) 34.3 eV and 36.5 eV (blue) were assigned to W⁵⁺. The composite fits are shown in gold. All peak intensities are normalized to the tungsten 4f_{7/2} peak for each sample.

The pristine WO₃-{ $\bar{1}20$ } film exhibits intense W 4f_{7/2} and 4f_{5/2} peaks at 35.4 eV and 37.6 eV, respectively, due to W⁶⁺. A prominent oxygen peak at 530.2 eV can be attributed to W-O bonds found in oxides.¹¹⁸ A small adventitious carbon peak appears at 284.8 eV. After cycling, substantial changes occur in the carbon, lithium, oxygen, and tungsten XPS data. The C 1s data of the WO₃-{ $\bar{1}20$ } film shows an increase in the adventitious carbon peak at 284.8 eV as well as new peaks at 286.7 eV and 290.0 eV (**Figure 5.13a**). The new peaks can be attributed to C-O and C=O bonds from the carbonate species, respectively, likely due to SEI layer formation as a result of propylene carbonate solvent decomposition.¹¹⁹ Prominent lithium and oxygen peaks appear at 55.4 eV and 531.7 eV, respectively (**Figure 5.13b-c**), further suggesting the presence of lithium carbonate species in the SEI at NR surfaces.¹¹⁹ However, we were unable to quantify

the SEI composition because deconvolution of the O and C 1s signals from propylene carbonate and WO_3 is challenging for these nanostructured films.¹²⁰ Nonetheless, the Li XPS data indicates Li-ions are a component of the SEI layer. No significant W^{5+} was expected since the cycling experiments ended on an anodic polarization pulse. However, a W^{5+} shoulder at 34.2 eV is evident in XPS data after 500 cycles (**Figure 5.13d**). Therefore, Li-ions are likely also trapped at reduced W sites in the NR interior. The relative amount of residual W^{5+} after cycling is 14.6% for WO_3 - $\{\bar{1}20\}$ and 20.0% for WO_3 - $\{100\}$, as determined by peak area comparison. Note a shift in the W and O binding energy after cycling, which could be due to surface charging during the XPS experiment as a result of excess insulating SEI on the $\{100\}$ facets. TOF-SIMS mapping experiments show qualitatively similar distributions of C, Li, and Cl across the surfaces of both films. **Figure 5.14** shows the 2D distributions of negatively charged species detected by TOF-SIMS on the surfaces of WO_3 - $\{\bar{1}20\}$.

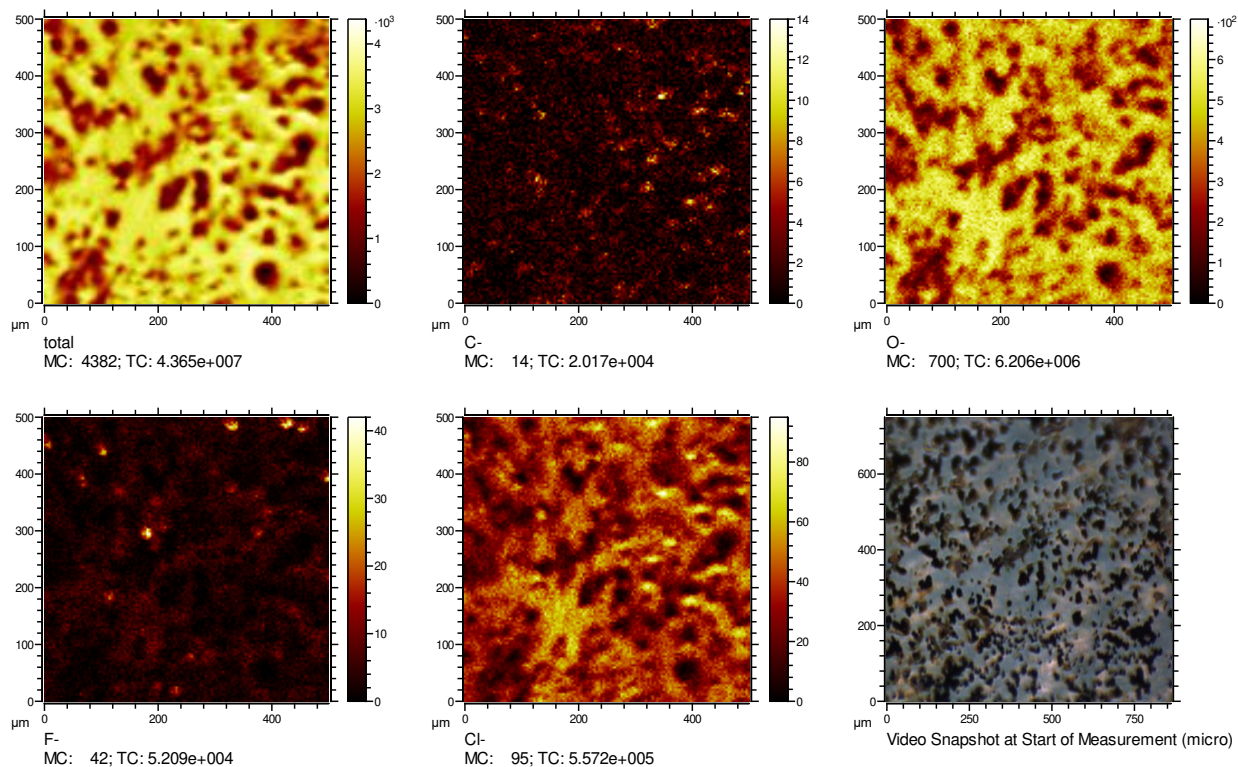


Figure 5.14 – 2D TOF-SIMS spectra for WO_3 - $\{\bar{1}20\}$. Top, left to right: total, C, O. Bottom, left to right: F, Cl, optical image. Brighter colors indicate larger abundance.

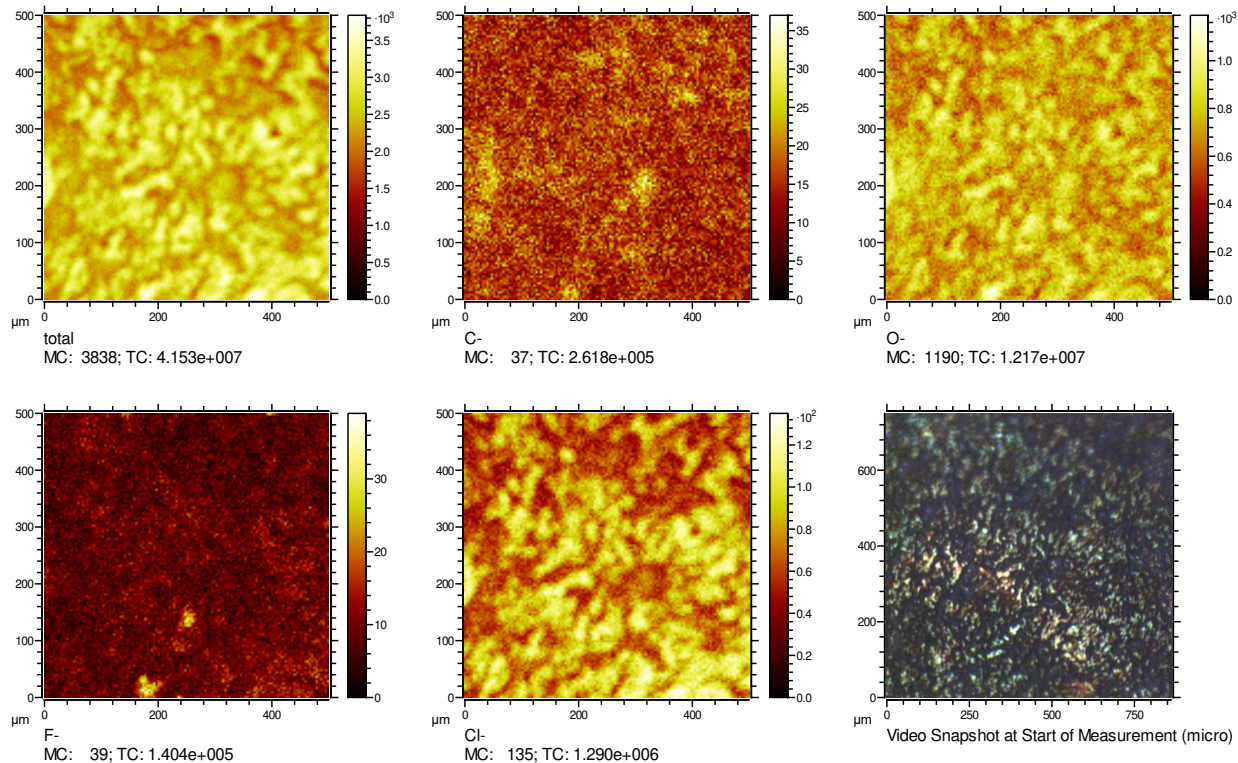


Figure 5.15 – 2D TOF-SIMS spectra for $\text{WO}_3\text{-}\{100\}$. Top, left to right: total, C, O. Bottom, left to right: F, Cl, optical image. Brighter colors indicate larger abundance.

Figure 5.15 shows the 2D distributions of negatively charged species detected by TOF-SIMS on the surface of $\text{WO}_3\text{-}\{100\}$. The C^- , O^- , and Cl^- species are likely parts of the solid electrolyte interface (SEI) on the WO_3 films. The F^- , and likely some of the Cl^- signal may be from impurities in the exposed glass substrate. The key point is that the distribution of SEI species is similar in both samples. The intensity of the signal is higher across the entire sampled surface for the $\text{WO}_3\text{-}\{100\}$ which indicates an SEI layer that covers more of the film. In addition, TOF-SIMS depth profiling measurements revealed similar spatial distribution of Li, W, and C throughout the film thickness, but the carbonaceous layer may be thinner on $\text{WO}_3\text{-}\{\bar{1}20\}$ (**Figure 5.16**). In summary, XPS and TOF-SIMS data indicate that lithium carbonate-containing SEI layers form on these h- WO_3 samples and the SEI composition does not vary among the samples.

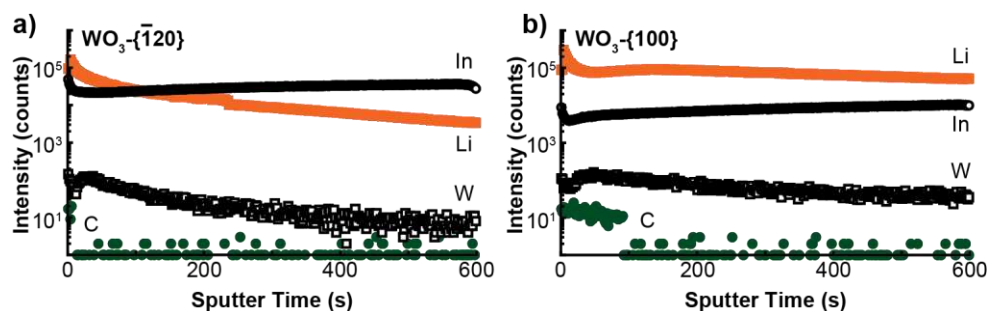


Figure 5.16 – Sputter time TOF-SIMS. a) The intensity of In, Li, W, and C species as a function of sputter time into the depth of the film for $\text{WO}_3\text{-}\{\bar{1}20\}$. b) same as (a) but for $\text{WO}_3\text{-}\{100\}$.

Figure 5.16 shows the intensity of In, Li, W, and C species in sputter time-dependent TOF-SIMS. Sputter time is proportional to (not equal to) depth bored into the sample. Direct comparisons of SEI depth cannot be made because the sputter time was not calibrated to depth for each sample. However, the C signal in $\text{WO}_3\text{-}\{\bar{1}20\}$ falls to zero 10× faster than for $\text{WO}_3\text{-}\{100\}$ which implies the SEI is thinner. This is not due to ablation through the thinner $\text{WO}_3\text{-}\{\bar{1}20\}$ film ($474 \text{ nm} \pm 170 \text{ nm}$ vs $1315 \text{ nm} \pm 300 \text{ nm}$ for $\text{WO}_3\text{-}\{100\}$); the W signal is well above zero. Additionally, the Li signals begin at the same intensity for both samples, but fall by two orders of magnitude for $\text{WO}_3\text{-}\{\bar{1}20\}$. This indicated less Li^+ is trapped in the film. This is consistent with the XPS results (**Figure 5.13**) showing less relative amount of reduced tungsten (W^{5+}). The above evidence seems to imply a thinner and smaller total surface area formation of SEI in $\text{WO}_3\text{-}\{\bar{1}20\}$.

5.2 Discussion

Based on literature¹⁰⁸ and previous single particle-level studies⁶⁹, the h- WO_3 particles with dominant $\{\bar{1}20\}$ facets were hypothesized to exhibit enhanced optical modulation and stability. Particles with $\{\bar{1}20\}$ facets showed increased OD stability but decreased CE. The $\text{WO}_3\text{-}\{100\}$ sample shows two types of optical modulation degradation: coloration degradation (i.e., maximum OD decays in the colored state with increasing cycle number) and transparency degradation (minimum OD decays in the bleached state with increasing cycle number). Both effects have been linked to ion trapping¹⁰⁹ where Li-ions insert in the WO_3 lattice during the coloration step and remain in the host lattice after the bleach step.^{107,121,122} The trapping mechanisms and chemical nature of the trapping sites are not entirely understood over a broad

range of electrochromic materials.^{107,109,122–127} These degradation effects are important for electrochromic smart windows because the material is unable to consistently reach a colored or transparent state with increasing on/off cycles. Interestingly, the $\text{WO}_3\text{-}\{\bar{1}20\}$ sample does not show either coloration or transparency degradation after the initial cycle (**Figure 5.7a**). Instead, coloration and transparency characteristics slightly improve with cycling, though the magnitude of the modulation is always lower for $\text{WO}_3\text{-}\{\bar{1}20\}$ than $\text{WO}_3\text{-}\{100\}$.

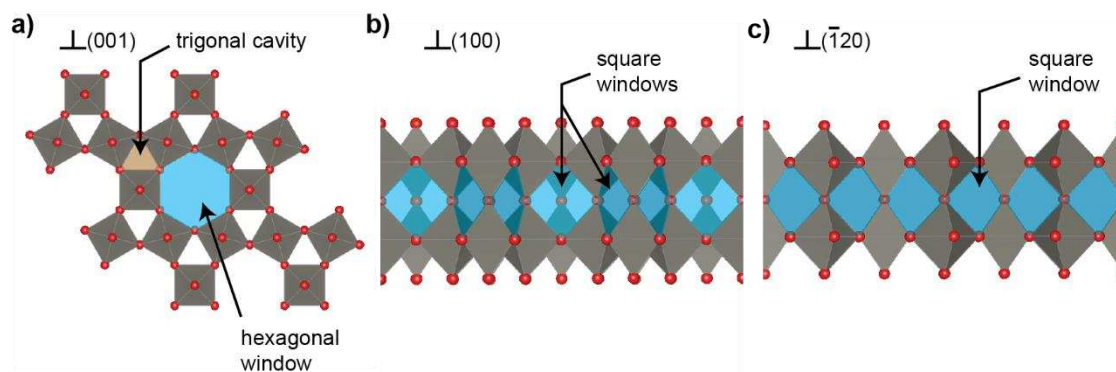


Figure 5.17 – Structure and binding sites in hexagonal WO_3 . Top (perpendicular) eye view looking down into the (a) (001) plane showing trigonal cavity and hexagonal window ion binding sites, (b) (100) plane showing square windows, and (c) $(\bar{1}20)$ plane also showing square window sites.

The lower ΔOD in $\text{WO}_3\text{-}\{\bar{1}20\}$ may be explained by a higher fraction of optically inactive sites.

Figure 5.17 shows perpendicular views into the (001), (100), and $(\bar{1}20)$ planes that are present at the surfaces of these NRs (see **Figure 5.3**). In addition, **Figure 5.17** illustrates the three Li-ion binding sites in h- WO_3 : trigonal cavities, hexagonal windows, and square windows. The hexagonal windows and square windows contribute to OD changes whereas the trigonal cavity site contributes little or no optical activity.^{52,54} The trigonal cavity and hexagonal window sites are most easily accessed by the (001) plane (**Figure 5.17a**) present on the endcaps of both samples (**Figure 5.3d,e**). The $\text{WO}_3\text{-}\{\bar{1}20\}$ sample has a larger surface area of {001} planes than the $\text{WO}_3\text{-}\{100\}$ sample (8% vs 3% with the geometry illustrated in **Figure 5.3**) and, therefore, has more optically inactive trigonal cavity sites at the NR surface. Hence, the lower ΔOD of $\text{WO}_3\text{-}\{\bar{1}20\}$ NRs may be explained by the fact that Li-ions prefer to occupy these optically inactive trigonal cavities^{52,54} and those sites are more abundant on $\text{WO}_3\text{-}\{\bar{1}20\}$ NR surfaces.

The CE increase of the $\text{WO}_3\text{-}\{100\}$ film can be attributed to the SEI layer formation process. In this scenario, applying cathodic polarization to the pristine materials induces an interfacial charge transfer reaction where solvent molecules are reduced at the NR surfaces. This SEI layer formation process reduces CE because injected electrons reduce solvent molecules instead of contributing to an OD increase at 940 nm. SEI growth diminishes with increasing cycle number presumably because the insulating surface coating inhibits the electro-reduction reaction.¹²⁸ This SEI formation process consumes more charge during initial cycling of the $\text{WO}_3\text{-}\{100\}$ sample than the $\text{WO}_3\text{-}\{\bar{1}20\}$ sample.

The $\text{WO}_3\text{-}\{100\}$ sample likely exhibits poor electrochromic stability due to a crowded path for Li-ions via (100) planes. **Figure 5.17b-c** shows Li-ion insertion pathways via square window sites at the (100) versus ($\bar{1}20$) surfaces. These planes make up the majority of the NR surfaces in the $\text{WO}_3\text{-}\{\bar{1}20\}$ sample. We speculate that the energy barriers for Li-ion insertion via the different surface planes are not equal due to the different orientation of square window sites. The (100) plane features parallel and perpendicular repeating patterns of square window sites (**Figure 5.17b**). This crowded environment differs from the square windows at the ($\bar{1}20$) plane (**Figure 5.17c**). The crowded square windows on the (100) plane are hypothesized to increase energy barriers for Li-ion insertion, creating Li-ion trapping sites. In this scenario, the overpotential for Li-ion extraction increases as more Li-ions occupy crowded square window sites. This effect could explain the long-term optical degradation of the colored state in $\text{WO}_3\text{-}\{100\}$ NRs. The trapping effect may prevent new Li-ions from inserting into the host, which also explains the transparent state degradation in $\text{WO}_3\text{-}\{100\}$.

Another explanation for optical degradation of the $\text{WO}_3\text{-}\{100\}$ sample could be growth of an insulating SEI on {100} and {001} planes that induces an overpotential for ion insertion/extraction. EIS data showed a significant increase in R_{ct} in the $\text{WO}_3\text{-}\{100\}$ samples that could be attributed to an insulating SEI layer on the {100} planes that account for 95% (area) of $\text{WO}_3\text{-}\{100\}$ NR surface area. Depth profiling via TOF-SIMS suggests the SEI layer may be thicker in the $\text{WO}_3\text{-}\{100\}$ films (**Figure 5.16**). In this scenario, the SEI layer rapidly grows on the {100} planes, contributing to the low CE at early cycle numbers

(Figure 5.11). Ion insertion becomes more difficult with increasing cycle number; increasing cathodic polarization would be required to achieve the same total charge as the early cycle numbers. Ion extraction also becomes more difficult because increasing anodic polarization would be required to de-populate Li-ions from stable, low energy binding sites. This would be unexpected because $\{\bar{1}20\}$ have a higher surface potential than both $\{100\}$ and $\{001\}$ ¹²⁹, and the type/rate of electrolyte decomposition is directly related to the surface potential.¹³⁰ However, the XPS and TOF-SIMS data showed no clear facet-dependent SEI characteristics and the mechanism of SEI formation on the different facets of h-WO₃ is not well understood.¹²⁸ An alternative hypothesis is that the high energy $\{\bar{1}20\}$ facet reconstructs under electrochemical conditions. An SEI layer with favorable charge/ion transfer characteristics could form on the reconstructed surface. Surface reconstruction can impact interfacial ion (de)insertion kinetics and also influence disorder in the bulk.¹³¹ In this scenario, the $\{\bar{1}20\}$ surface reconstructs into the lowest available surface potential and influences the location, morphology, or relative abundance of the SEI. In situ TEM or X-ray probe techniques may be necessary to test this hypothesis.

Particle size and shape have been shown to impact OD switching speeds and magnitude in electrochromic WO₃ systems¹³²⁻¹³⁴, but systematic studies on the role of particle size and shape on coloration or transparency degradation are lacking. One study by Yuan et al. suggested that particle size has little influence on the stability of tetragonal tungsten oxide.¹³² There are conflicting reports in the literature on the role of particle size on OD magnitude. Yuan et al. showed increasing particle size increases OD magnitude in tetragonal tungsten oxide films of equivalent thickness¹³², but Kim et al. and Subrahmanyam et al. observed the opposite effect for monoclinic¹³⁵ and amorphous¹³⁶ systems, respectively. While it is possible that the particle size could influence extinction spectra via confinement⁵⁰, our large h-WO₃ NRs are not in the confinement regime. The porosity and packing density within the film could influence electrochromic properties,^{137,138} but crystallinity was shown to be more impactful.¹³⁷ We conclude that particle size differences between these two samples is likely not the dominant contributor to enhanced OD stability in WO₃- $\{\bar{1}20\}$, but this possibility cannot be excluded.

Mechanical degradation (e.g. cracking, delaminating) of films are known to decrease lifetime of electrochromic devices.¹³⁹ SEM imaging before and after electrochemical cycling did not reveal mechanical degradation for $\text{WO}_3\text{-}\{100\}$ (**Figure 5.18**). h-WO_3 exhibits minimum volume expansion (and no crystalline phase change) during ion insertion⁴⁵, unlike amorphous¹⁴⁰, triclinic⁷⁶, and monoclinic⁷⁷ WO_3 polymorphs. Hence, differences in mechanical degradation likely cannot explain the electrochromic stability enhancement effect.

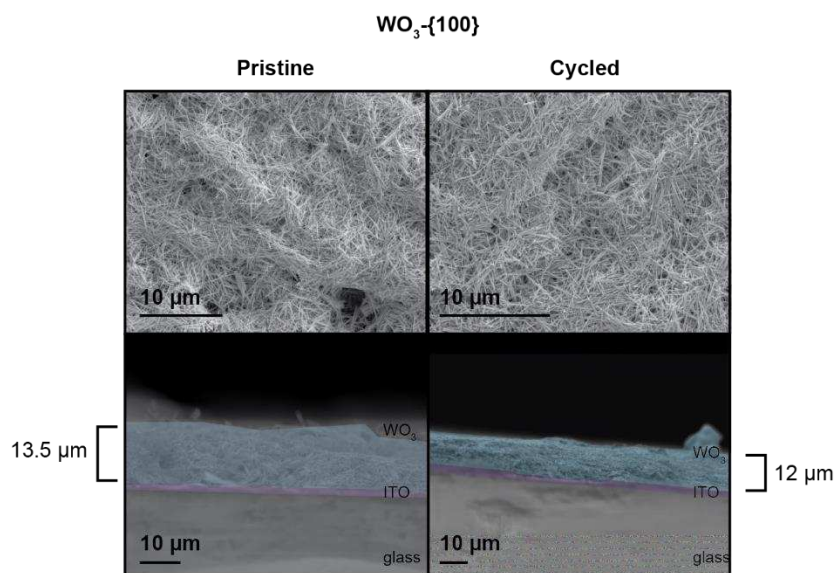


Figure 5.18 – SEM images before (pristine) and after 150 cycles. Top-down image of $\text{WO}_3\text{-}\{100\}$ before (top left) and after (top right cycling) and cross-sectional image before (bottom left) and after (bottom right) cycling. These thick films were not the same films as shown in the main text.

This facet-dependent study has implications for electrochromic smart windows based on nanoscale materials. The stability enhancement observed for $\text{WO}_3\text{-}\{\bar{1}20\}$ make it a better choice for electrochromic smart windows compared to $\text{WO}_3\text{-}\{100\}$. A device that can maintain constant optical changes over many cycles is more desirable than one that shows significant degradation after the first 100 cycles. The major benefits for the $\text{WO}_3\text{-}\{100\}$ film are the larger OD modulation and increased coloration efficiency. However, thicker $\text{WO}_3\text{-}\{\bar{1}20\}$ NR films and device optimization may mitigate these shortcomings. In summary, h-WO_3 particles with dominant $\{\bar{1}20\}$ facets could improve the performance of electrochromic smart windows.

5.3 Conclusion

Two h-WO₃ NR samples with distinct surface facet orientations were synthesized. The h-WO₃ NR sample with $\{\bar{1}20\}$ facets exhibited more stable long-term electrochromic behavior than NR samples with $\{001\}$ and $\{100\}$ surface facets only. The WO₃- $\{100\}$ film exhibited greater coloration efficiency but diminished total optical modulation after 500 cycles. The type and arrangement of Li-ion binding sites present at the different surface facets likely influence ion trapping and electrochromic reversibility. These findings suggest that nanoparticle surface facets can be used to optimize performance of nanostructured electrochromic thin films for smart window applications.

CHAPTER 6: QUANTIFYING CAPACITIVE-LIKE AND BATTERY-LIKE CHARGE STORAGE CONTRIBUTIONS USING SINGLE NANOPARTICLE ELECTRO-OPTICAL IMAGING^{iv}

Pseudocapacitors promise to combine the high-rate capability of electrochemical capacitors with the high energy-density of batteries. A major challenge in the field is to demonstrate that pseudocapacitors behave electrochemically like a capacitor and the charge storage process is faradaic in nature. It is challenging to do so because pseudocapacitive charging has the same electrical signatures as non-faradaic electrical double layer charging. Electro-optical imaging can measure Li-ion insertion reactions in single WO_3 nanoparticles, as discussed in previous chapters, without being muddled by contributions that plague electrochemical measurements alone (i.e. wide particle size distribution, pores, and interfacial contact between particles). On average, these single WO_3 particles exhibit a hybrid charge storage mechanism: both diffusion-limited (battery-like) and pseudocapacitive (capacitor-like) mechanisms contribute to the total charge stored as detailed in CHAPTER 4:. It is widely assumed that surface chemistry dictates the pseudocapacitive charge storage behavior for intrinsic pseudocapacitors like WO_3 but is not rigorously quantified. Electrical double layer charging, electrochemical corrosion, and surface impurity reactions could all contribute to the total current, but those processes have nothing to do with pseudocapacitance. Donne and co-workers recently reviewed the challenges and presented an elegant and reliable potential step method for deconvoluting the current-time response.^{142,143} Their method comparison study revealed how different electrochemical methods and data analysis procedures can influence the interpretation and quantification of charge storage processes in ion insertion electrodes.^{142,144} A major open

^{iv} This chapter contains adaptations from Evans, R. C.; Nilsson, Z.; Balch, B.; Wang, L.; Neilson, J. R.; Weinberger, C. R.; Sambur, J. B. Quantifying Capacitive-Like and Battery-Like Charge Storage Contributions Using Single-Nanoparticle Electro-Optical Imaging. *ChemElectroChem* **2020**, *7* (3), 753–760. <https://doi.org/10.1002/celec.201902011>. citation⁽¹⁴¹⁾. R.C.E. performed experiments, analyzed data, and wrote the manuscript. Z.N.N. performed SEM and TEM imaging experiments. B.B aided in mathematical modeling. L.W. performed integral AFM measurements. J.R.N. performed Rietveld refinement and provide materials chemistry insight. C.R.W. aided in the kinetics fitting routine development. J.B.S. and R.C.E. developed the experimental setup, analyzed data, and wrote the manuscript.

question in the field is how much, and on what time scale can charge be inserted into the bulk of a material at a rate that is not limited by typical solid state diffusion kinetics.

The results in this chapter show that individual particles exhibit different charge storage mechanisms at the same applied potential and that pseudocapacitive charge is stored at or near the nanorod surface (not in the bulk). Longer nanorods store more pseudocapacitive charge than shorter nanorods, presumably due to (1) a surface step edge gradient that exposes large hexagonal window Li-ion binding sites along the nanorod length (different crystalline facets are exposed) and/or (2) higher structural water content that influences the Li-ion binding energetics and diffusion behavior. Penetration depth of Li-ion insertion during pseudocapacitive kinetics were quantified. Li-ions insert as deep as two-unit cells below the surface. The methodology presented herein can be applied to a wide range of solid state ion-insertion materials.

6.1 Results and Discussion

6.1.1 Materials Synthesis and Characterization

The h-WO₃ nanorod sample was synthesized in the same fashion described in 3.1 Material Synthesis. Additional characterization of the same material was done through thermogravimetric analysis (TGA) and energy dispersive x-ray spectroscopy (EDS). TGA analysis results showed about 2.5% mass loss from 90 °C to 200 °C, which corresponds to ~0.3 H₂O per WO₃ (**Figure 6.1a**). The theoretical maximum water content is 7.2% for the monohydrate. **Figure 6.1b** shows the derivative of sample weight as a function of temperature in **Figure 6.1a**. The inflection points in the derivative (solid grey lines) were used to define the range over which mass loss could be attributed to water loss.

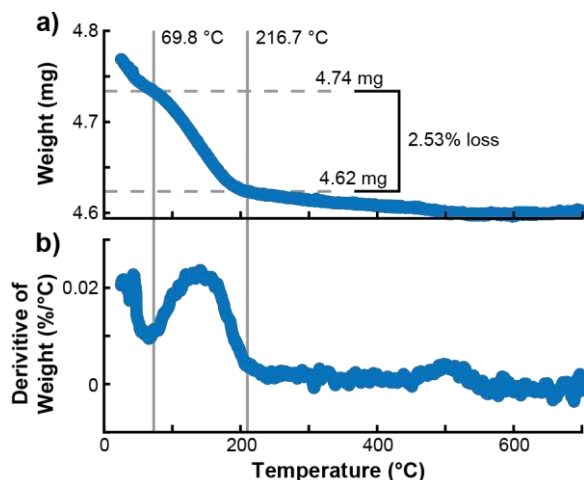


Figure 6.1 – Thermogravimetric analysis (TGA). a) The weight of the nanoparticle sample as a function of time. b) The derivative of weight with temperature plotted against temperature.

The TGA sample was prepared by first evaporating 1 mL of nanoparticle suspension, leaving behind the white nanoparticle sample. About 4.7 mg of this powder was loaded onto a platinum pan for TGA. The sample was heated from room temperature to 700 °C at 5 °C min⁻¹ under a nitrogen atmosphere.

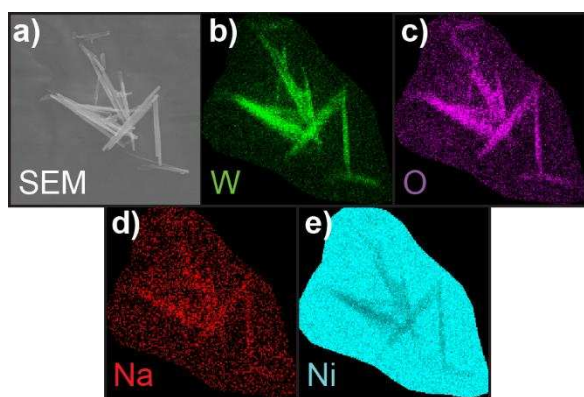


Figure 6.2 – Energy dispersion x-ray spectroscopy (EDS) for a cluster of nanorods. a) SEM image of nanorod cluster on nickel foil. b-e) W, O, Na, and Ni element specific maps from EDS.

EDS samples were prepared by washing about 1 mL of nanoparticle suspension from the reactor six times with 18.2 MΩ-cm water and suspended in 200 proof ethanol before being drop cast onto a nickel film. The sample was placed in the SEM (JEOL JEM-2100F) and imaged at 20 keV for EDS (**Figure 6.2a**).

Figure 6.2b-e shows the EDS maps for W, O, Na, and Ni, respectively. While the Na present in the

nanorods is evident, it should be noted that the Ni L α Peak at 0.851 keV is broad enough to increase the Na K α background signal at 1.04 keV. EDS showed that there is about 2.45% Na relative to W.

Figure 6.3 shows the PXRD data and Rietveld analysis accounting for water and sodium in the composition with inclusion of strong preferred orientation ((200) and (2 $\bar{1}$ 0) orientations), as expected from the anisotropic shape of the particles.

Electro-optical characterization was performed as described in CHAPTER 3: excepting at various potentials rather than only -1.0 V vs Ag/AgCl for the coloring step. Here, a bleaching pulse of 1.5 V for 200 s and color pulses from -0.2 V to -1.0 V with 100 mV resolution for 200 s were used.

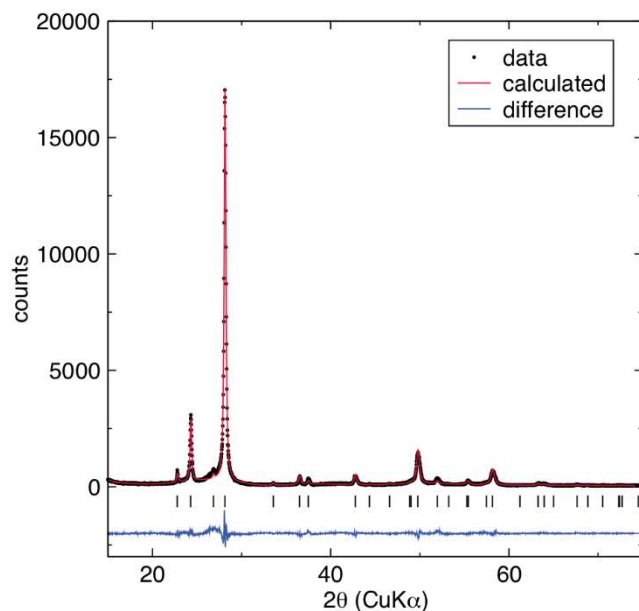


Figure 6.3 – PXRD of WO₃ nanorods on a zero-diffraction Si puck. PXRD from 10 2θ to 80 2θ.

Figure 6.4 shows a representative $\Delta OD_d(t)$ trajectory for a single nanoparticle during the normal pulse voltammetry experiment. For E more positive than -0.4 V, $\Delta OD_d(t)$ does not increase with time, which indicates that those potentials are not sufficiently cathodic to drive the ion insertion reaction in Equation 2-1. However, $\Delta OD_d(t)$ increases at $E = -0.4$ V. Onset potential (E_{onset}) is quantitatively defined as the value of E that causes $\Delta OD(t)$ to exceed a value of three times the standard deviation of background

noise plus the mean background noise, as described in previous chapters. Upon applying a potential more negative (cathodic) than -0.4 V, $\Delta OD_d(t)$ quickly increases, and then rises gradually with increasing cathodic polarization time. The $\Delta OD_d(t)$ decreases rapidly upon applying the anodic polarization step. The $\Delta OD_d(t)$ magnitude increases significantly with increasingly cathodic potentials, but the $\Delta OD_d(t)$ dynamics are essentially independent of E . Fifty-four individual nanoparticles were analyzed in this study and 41 particles exhibited an E_{onset} value that was more positive than -1.0 V. The optically inactive particles (13 of 54, or 24%) may require a larger overpotential for the electrochemical reaction in Equation 2-1 or have poor electrical contact to the ITO electrode.

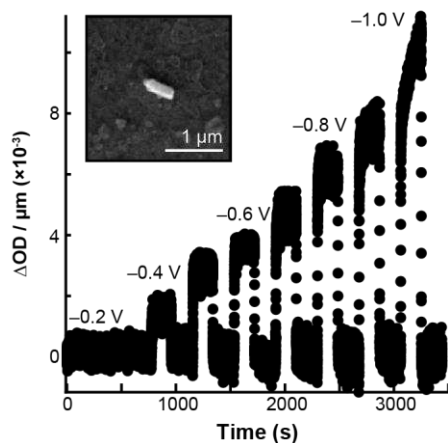


Figure 6.4 – Potential dependent single particle optical response. The particle thickness-corrected change in optical density (ΔOD_d) of the single WO_3 nanorod shown in the inset during a normal pulse voltammetry experiment. The potential was stepped from a constant anodic potential ($+1.5$ V) to different cathodic potentials (from -0.2 V to -1.0 V vs Ag/AgCl).

6.1.2 Hybrid Charge Storage Mechanism

This section is meant to serve as a reminder of the details for the hybrid charge storage kinetic model used to fit the optical density changes as described in 4.1 Kinetic Model. In 6.1.3 Single Nanoparticle Charge Storage Behavior a modification will be discussed so it is helpful to quickly reiterate here.

Figure 6.5a shows the average $\Delta OD_d(t)$ response from the optically active nanoparticles. The $\Delta OD_d(t)$ data has the following dynamic features: (1) a short waiting time (t_{wait}) for color center formation

due to Li-ion insertion at optically inactive sites (likely trigonal cavity sites)^{54,69}, (2) an exponential burst in ΔOD_d at short times, and (3) a slow rise in ΔOD_d that scales with $t^{1/2}$ at long times. The exponential ΔOD_d increase can be attributed to a faradaic reaction (Equation 2-1) that occurs at a capacitive-like rate (i.e., pseudocapacitance). According to the Cottrell equation, the ΔOD_d increase that scales with $t^{1/2}$ can be attributed to the diffusion-limited ion insertion process in the nanorod interior. The scaling laws suggest that these nanoparticles exhibit a hybrid charge storage mechanism where both pseudocapacitive and diffusion-limited charge storage mechanisms contribute to the total charge, in agreement with literature.⁹¹ These OD measurements do not have underlying contributions from non-faradaic double layer charging because those processes do not contribute to the OD change.

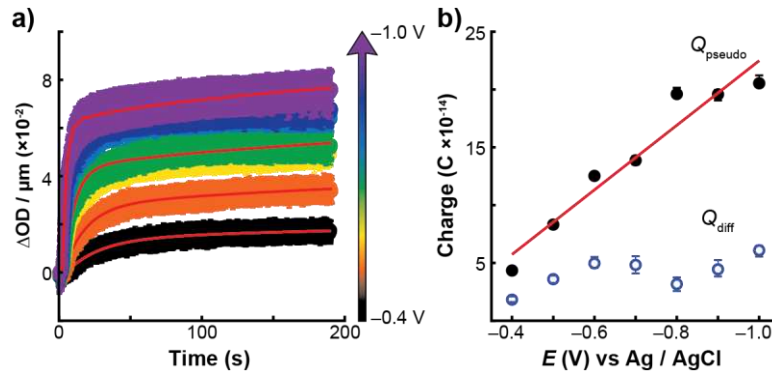


Figure 6.5 – Particle averaged $\Delta OD_d(t)$ analysis. a) $\Delta OD_d(t)$ trajectories as a function of applied cathodic step potential over the range of -0.4 V to -1.0 V vs Ag/AgCl. The red line represents fits to the data using Equation 5. Error bars on the data points represent the standard deviation between three cathodic cycles. b) Diffusion-limited (Q_{diff}) and pseudocapacitance (Q_{pseudo}) charge contributions to the total charge obtained from the fits in (a). The error bars are as the value obtained when the mean square error of the fit doubles. The red line represents a linear fit to the pseudocapacitance contribution, with an $R^2 = 0.97$ and a slope = 2.8×10^{-13} F, average capacitance is 6.4×10^{-13} F/cm² \pm 5×10^{-13} F/cm².

Equation 4-5 and Equation 4-6 are restated as Equation 6-1 and Equation 6-2, respectively.

Equation 6-1 was applied for potential dependent fitting as described for a single potential in 4.1 Kinetic Model.

$$H(t - t_{\text{wait}}) \left(-\frac{A}{k_{\text{pseudo}}} [\exp(-k_{\text{pseudo}}t) - \exp(k_{\text{pseudo}}t_{\text{wait}})] \right) + 2D'\sqrt{t} \quad \text{Equation 6-1}$$

Where A , k_{pseudo} , t_{wait} , and D' are fitting parameters. D' is given by Equation 4-5 below

$$D' = \frac{Q_{max}\sqrt{D_{Li}}}{d\sqrt{\pi}} \quad \text{Equation 6-2}$$

The fit result to the experimental data is shown in **Figure 6.5a**. Since the data could be fit with a time independent D_{Li+} value, the trajectory analysis suggests that D_{Li+} does not change significantly over the time scale of the experiment. Change in charge for both kinetic regimes, $\Delta Q_{diff}(t)$ and $\Delta Q_{pseudo}(t)$, can be summed to obtain the total charge injected during each process, Q_{diff} and Q_{pseudo} .

Figure 6.5b compares Q_{diff} and Q_{pseudo} versus E . The charge injected due to the diffusion-limited process, Q_{diff} , is generally independent of E for E more negative than -0.4 V. The small peak at -0.6 V in **Figure 6.5b** (blue points) could be due to the fact that the applied potential is not sufficiently cathodic to reduce all the electroactive sites in all the particles. This hypothesis is supported by recent optically-detected single particle-level cyclic voltammetry (CV) measurements that showed broad CV peaks over the range of -0.4 V to -0.8 V.⁶⁹ Thus, it is possible that the 100 mV steps in this potential range are not sufficiently cathodic to reduce all sites in all the particles. The standard potential (E^0) estimated for the reaction in Equation 2-1 is between -0.3 V and -0.4 V because of the observed dramatic increase in OD between those potentials.

On the other hand, Q_{pseudo} increases linearly with E ($R^2 = 0.97$, slope = 2.8×10^{-13} F, average capacitance is 6.4×10^{-13} F/cm² \pm 5×10^{-13} F/cm²). Linear behavior is expected for a capacitive-like charging process in a normal pulse voltammetry experiment because the total capacitive charge scales linearly with the magnitude of the potential step.¹⁴⁵

In summary, the single particle-averaged $\Delta OD_d(t)$ data showed clear scaling relations with time that could be attributed to both diffusion-limited and capacitive-like charge storage mechanisms, in agreement with literature.⁹¹ Since the origin of the OD signal is faradaic in nature, the capacitive-like charge storage process is denoted as pseudocapacitance.

6.1.3 Single Nanoparticle Charge Storage Behavior

Here $\Delta OD_d(t)$ data at the single particle-level is analyzed to understand how each nanorod contributes to the average response. **Figure 6.6c,d** shows potential-dependent $\Delta OD_d(t)$ traces (black circles) for the two different nanorods shown in **Figure 6.6a,b**. Note that the nanorod surfaces appear rough and the contrast is blurry in these ex-situ SEM images likely because the rinsing procedure did not completely remove electrolyte residue from the ITO substrate.

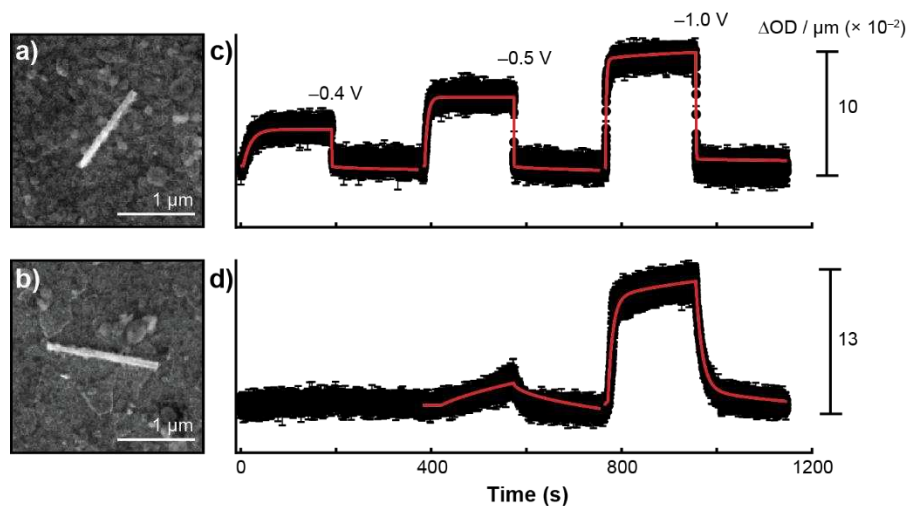


Figure 6.6 – Representative examples of single particle charge storage behavior. a, b) SEM images of a single WO_3 nanorods. c) The corresponding $\Delta OD_d(t)$ traces at -0.4 V, -0.5 V, and -1.0 V respectively. The red lines represent a fit to the data using Equation 5 and contributions from both ΔQ_{diff} and ΔQ_{pseudo} . d) same as (c), but for the other nanorod. The red line fit for -0.5 V data represents a fit to Equation 6-3 with contributions from ΔQ_{diff} only. The red line fit for -1.0 V data represents a fit to Equation 6-1 with contributions from ΔQ_{diff} and ΔQ_{pseudo} .

Single nanoparticle-level measurements show three important features that are hidden in particle-average data. First, E_{onset} is particle-dependent. For example, the nanorod in **Figure 6.6c** exhibits an OD change at -0.4 V whereas the nanorod in **Figure 6.6d** exhibits an OD change at -0.5 V. These two nanorods exhibit distinct E_{onset} values even though they were synthesized in the same batch, have similar physical properties, and are located just microns apart on the ITO electrode. Second, there is a particle dependent overpotential for the pseudocapacitive process. For example, the nanorod in **Figure 6.6d** does not exhibit an exponential OD burst at its onset potential (-0.5 V). The absence of the OD burst indicates that the nanorod in **Figure 6.6d** does not undergo the pseudocapacitive charge storage process at the same applied

potential as the nanorod in **Figure 6.6b**. Instead, the pseudocapacitive process onsets at more negative potentials (see -1.0 V data in **Figure 6.6d**). Third, some particles exhibit diffusion-limited charge storage mechanism only even though the particle-average measurements indicate that all particles follow the hybrid charge storage mechanism (see -0.5 V data in **Figure 6.6d**). As a result, the ΔQ_{pseudo} component from Equation 6-1 was not needed to fit the data. Equation 6-3 below describes the diffusion only fit.

$$\Delta Q_{diff}(t) = \int_{t_{wait}}^t J_{diff}(t) dt = H(t - t_{wait})2D'\sqrt{t} \quad \text{Equation 6-3}$$

To gain statistically meaningful results from the single particle-level observations discussed above, $\Delta OD_d(t)$ trajectories from 39 nanoparticles were fit under two sets of conditions: (1) $\Delta Q_{diff}(t)$ and $\Delta Q_{pseudo}(t)$ contribute to the total charge as in Equation 6-1 and (2) $\Delta Q_{diff}(t)$ contributes to the total charge as in Equation 6-3. Charge storage from only pseudocapacitive events were not observed, so no attempts were made to fit under only $\Delta Q_{pseudo}(t)$ conditions. An algorithm was developed based on the mean squared error (MSE) between the data and fit to classify whether a hybrid charge storage mechanism or a diffusion-limited charge storage mechanism described the single particle behavior (detailed in 6.2.1 Mean Square Error Algorithm). If the MSE exceeded a 1×10^{-4} threshold value or the fits produced negative parameters (e.g., A , k_{psuedo} , or D'), then the particles were classified as anomalous because their $\Delta OD_d(t)$ behavior could not be quantitatively described by either mechanism. **Figure 6.6** shows representative fitting results to the experimental data (red line). The fit adequately describes the data for a large number of particles over a range of applied potentials. This procedure allowed us to classify the charge storage behavior for each particle as a function of the applied potential.

Figure 6.7a shows the particle dependent classification results, where the magnitude of each bar represents the number of particles in the sample whose charge storage behavior could be described by a hybrid (yellow bar), diffusion-limited (red bar), or anomalous mechanism (blue bar). Since there was no OD change for particles at -0.2 V and -0.3 V, no particles appear in those bins. At -0.4 V, 53 % of particles exhibit a hybrid charge storage mechanism and 30% exhibit a diffusion-limited mechanism. 17% of

particles showed anomalous charge storage dynamics that could not be described by Equation 6-1 or Equation 6-3. More and more particles transition from the diffusion-limited or anomalous mechanisms to the hybrid mechanism with increasingly cathodic potentials. For E more negative than -0.6 V, almost every particle exhibits the hybrid charge storage mechanism. **Figure 6.7b** classifies the charge storage mechanism of each particle at E_{onset} . The single particle data shows a particle dependent onset potential for the hybrid charge storage mechanism. For example, 54% of nanorods onset with pseudocapacitance at -0.4 V while 36% and 33% of nanorods onset with pseudocapacitance at -0.5 V and -0.6 V, respectively. Thus, these single particle measurements reveal hidden behaviors that are not visible in the particle-averaged measurements. The particle-averaged data showed a smooth increase in capacitive-like charge storage with increasingly cathodic potentials, but single particles switch one-by-one from the diffusion-limited to hybrid charge storage mechanisms.

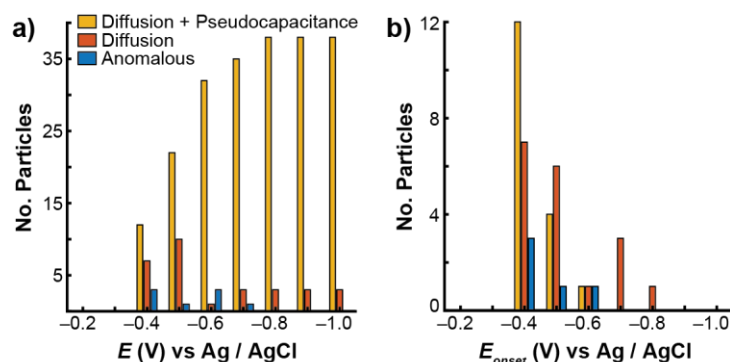


Figure 6.7 – Classifying charge storage mechanisms of single nanoparticles. a) Distribution of single particles that exhibited a diffusion-limited (red bar), hybrid diffusion-limited and pseudocapacitive mechanism (yellow bar), and anomalous mechanism (blue bar; see main text for description). No optical changes were detected at potentials more positive than -0.4 V. b) Distribution of charge storage mechanisms for single particles at their onset potential. E_{onset} is defined as the most positive potential where the $\Delta\text{OD}_d(t)$ signal exceeds three-times the limit of detection.

There are several possible origins of the particle dependent behaviors in **Figure 6.7**, such as physical parameters or morphology. There was no correlation between E_{onset} and nanorod physical properties such as length, width, height, and volume, as measured by Pearson’s correlation coefficient, between E_{onset} and the bulk physical properties of single nanoparticles.

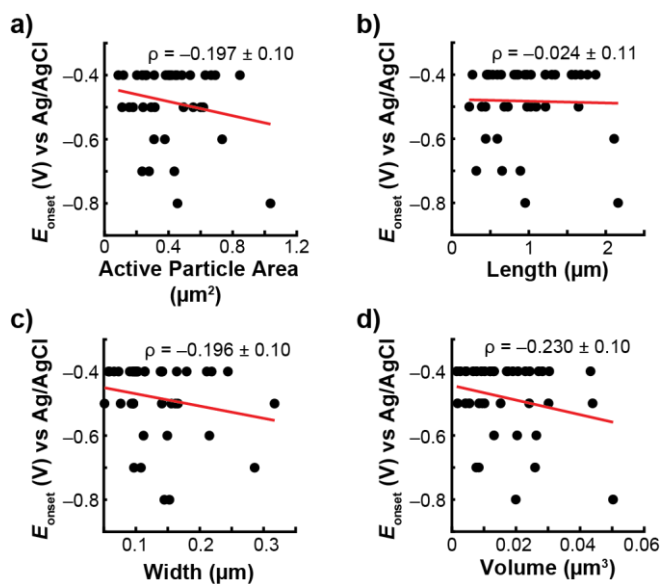


Figure 6.8 – Correlation of potential onset of optical activity (E_{onset}) with physical parameters. a-d) show the Pearson’s correlation with E_{onset} and active particle area, length, width, and volume, respectively. The Pearson’s correlation coefficients for (a-d) are $\rho = -0.197 \pm 0.10$, $\rho = -0.024 \pm 0.11$, $\rho = -0.196 \pm 0.10$, $\rho = -0.230 \pm 0.10$, respectively.

Figure 6.8 shows that different particles not only have different potential onsets (E_{onset}) for showing any optical changes, but can have onsets for certain types of charge storage behavior. Active surface area, length, width, and volume do not correlate to E_{onset} by Pearson’s correlation method, where the error in the coefficient is given by Eells.¹⁰⁵ Active surface area is defined as the area of the nanorod exposed to the electrolyte (all sides of the rod except the one laying on the ITO electrode). Thus, the driving force needed to induce optical changes is independent of the nanoparticle’s physical size.

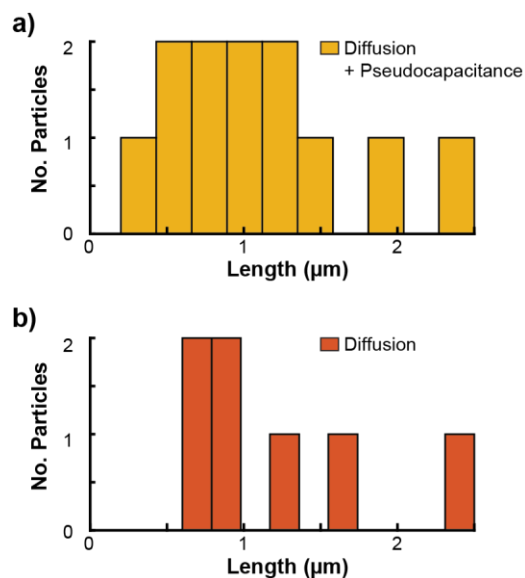


Figure 6.9 – Length distributions for different charge storage fits at -0.4 V vs Ag/AgCl. a) The distribution of nanoparticle lengths that were fit with a diffusion plus pseudocapacitance component at -0.4 V. b) The distribution of nanoparticle lengths that were fit with a diffusion only procedure at -0.4 V.

Note that E_{onset} and the onset of a specific charge storage mechanism are not mutually exclusive.

Figure 6.9 shows that the distribution of lengths do not differ between particle fits with a diffusion only vs a pseudocapacitance and diffusion fit at -0.4 V (the earliest onset seen). Therefore, the onset of a particular charge storage mechanism is independent of length at a 100 mV step resolution.

One possible explanation for this lack of correlation is that atomic-level or nanoscale surface structural heterogeneity induces the particle dependent E_{onset} for pseudocapacitance. Ex situ TEM measurements confirm that these WO_3 nanorods have a particle dependent surface step edge density; the subtle surface structural heterogeneities do not appear in the top-down view of the low-resolution SEM images. Those features could expose different crystallographic facets and Li-ion binding sites. For these hexagonal WO_3 nanorods, there are three Li-ion binding sites: trigonal cavities, hexagonal windows, and square windows— all of which result in different optical properties after ion insertion.^{52,54} It is possible that the distribution of surface sites have different energy levels for the redox reaction in Equation 2-1.¹⁴⁶ This hypothesis is supported by recent electro-optical cyclic voltammetry (CV) measurements that showed a distribution of redox waves for different nanoparticles.⁷⁵ Redox peaks in CV experiments are expected for

surface-limited faradaic reactions such as pseudocapacitive reactions.¹⁴⁷ One possible explanation for the particle dependent onset potential for diffusion-limited charge storage is that there is a significant contact resistance at the ITO/WO₃ interface. This contact resistance could be due to the wetting behavior of the WO₃ particles on the ITO substrate.¹⁴⁸ A significant contact resistance at the ITO/WO₃ interface could induce a larger potential drop for some particles. In this scenario, an additional driving force is needed to drive the electrochemical reaction in Equation 2-1 because some fraction of the applied potential drops across the interface. The OD onset could occur at more negative potentials for those particles with a significant contact resistance. Another possible explanation is that varying amounts of structural or surface adsorbed water in these nanorods influences the Li-ion binding energetics at the WO₃/electrolyte interface, and diffusion behavior within the nanorod bulk.¹⁴⁹⁻¹⁵¹

6.1.4 Quantifying Pseudocapacitive Charge Storage at Surface and Sub-Surface Sites

Pseudocapacitance is generally referred to as a faradaic charge transfer process that occurs at surface or near-surface sites. It is also possible that pseudocapacitance occurs throughout the material bulk.⁷ To determine the extent to which (Li⁺-W⁵⁺) color centers form at the surface or throughout the bulk, the total pseudocapacitive charge was compared with the total number of surface W sites. Total number of surface W sites were calculated using the surface area of a hexagonal prism using the particle dependent nanorod length and width from SEM. If the pseudocapacitive charge storage process is surface-limited, then we expect that the total number of (Li⁺-W⁵⁺) color centers will not exceed the total number of surface W atoms.

Figure 6.10a shows the total amount of (Li⁺-W⁵⁺) color centers produced during the pseudocapacitive process at -1.0 V vs the total number of surface W atoms. Each dot in **Figure 6.10a** represents a single particle (39 total) and the color scheme refers to the nanorod length. The red diagonal line represents 100% Li-ion occupation of surface sites. Short nanorods (blue data points) lie at or below the red diagonal, which indicates that surface sites are adequate to store all pseudocapacitive charge. Long nanorods lie above the diagonal line. At most, the longest nanorods have 2.5× more Li-ions inserted than

there are available surface sites. This trend indicates that sub-surface sites also participate in pseudocapacitive charge storage in longer nanorods.

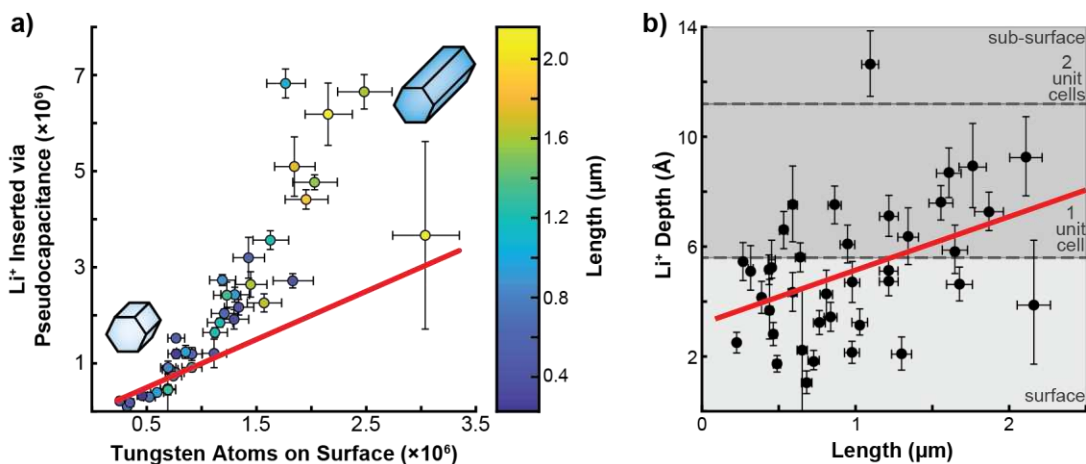


Figure 6.10 – Quantifying surface and near surface sites that contribute to the pseudocapacitive charge storage mechanism. a) Q_{pseudo} versus the number of surface W atoms for a particular nanorod, from $0.9\times$ to $3\times$ the number of W atoms on the surface of a particular nanorod. The red line is the diagonal and represents 100% Li^+ occupation of surface W sites. The color gradient represents the nanorod length. The cartoon nanorod schematically show that short and long nanorods have less and more pseudocapacitive charge storage contributions to the total charge, respectively. b) Li-ion insertion depth versus nanorod length. See Supplementary Note 2 for insertion depth calculation details. The insertion depth scales linearly with length (Pearson correlation coefficient is 0.43 ± 0.6). Error bars in Li^+ inserted represent the standard deviation from optical density propagated through the fitting procedure. The error in surface tungsten atoms was calculated using 5% relative error in SEM imaging propagated through the calculation. The error in nanorod length was calculated using 5% relative error in SEM, but the error in length was not used to calculate the Pearson correlation coefficient.

Depth of Li-ion insertion in each particle is estimated by assuming a uniform ion insertion rate from the entire nanorod surface that is in direct contact with the electrolyte (see 6.2.2 Quantifying Li^+ Insertion Depth). **Figure 6.10b** shows the Li-ion insertion depth versus particle length. The data shows that ($\text{Li}^+-\text{W}^{5+}$) color centers form 1 nm below the surface and there is a positive correlation between insertion depth and particle length (Pearson correlation coefficient is 0.43 ± 0.6). The positive correlation indicates that longer particles store more Li-ions in their bulk at a capacitive-like rate. The calculations also show that the extent of sub-surface Li-ion insertion is limited to 1-2 unit cells. Longer nanorods could store more pseudocapacitive charge than shorter nanorods because long nanorods could have more surface step features along their lengths, which exposes a gradient of large hexagonal window sites along the particle

(as described in CHAPTER 4:). In a perfect hexagonal prism morphology, the hexagonal window sites are confined to the nanorod end caps. A distribution of hexagonal window sites along the nanorod length could be more beneficial if an interfacial electric field at the step edge promotes the electrochemical reaction.^{69,101} Surface adsorbed or structural water present in larger quantities on longer nanorods could also improve kinetics.^{44,149} Regardless of the origin of the length-dependent effect, we conclude that these hexagonal nanorods do not exhibit intercalation pseudocapacitance. While it is possible that these calculations underestimate the total number of surface sites because we assume a perfect hexagonal prism morphology, that underestimation would still lead to the conclusion that less sub-surface sites participate in pseudocapacitive charge storage.

6.2 Algorithms and Derivations

6.2.1 Mean Square Error Algorithm

In order to classify the charge storage mechanism of single particles, an algorithm was developed to assign a mechanism to single particles. First, all particles are fit with Equation 6-1 and Equation 6-3. **Figure 6.11a,b** shows a representative example of ΔOD fits at -1.0 V vs Ag/AgCl for a single particle (shown in the inset) for diffusion only (Equation 6-3), and pseudocapacitance plus diffusion (Equation 6-1), respectively. The MSE for the diffusion fit is 7.4×10^{-6} while the MSE for the pseudocapacitance plus diffusion fit is 9.2×10^{-8} . Since that fit has an extra equation and could potentially over parameterize the data, the charge storage mechanism is classified as “pseudocapacitance plus diffusion” if the fit results in a 5-fold reduction of the error. In this case, the MSE for the pseudocapacitance plus diffusion fit is two orders of magnitude smaller, so the particle was assigned to the hybrid charge storage mechanism. This procedure is repeated for all particles at all potentials. **Figure 6.11c,d** show the MSE distributions for the diffusion only fit and pseudocapacitance fit at -1.0 V, respectively. The MSE is significantly lower for the pseudocapacitance plus diffusion fit, which is why almost all particles at -1.0 V are assigned to the hybrid charge storage mechanism

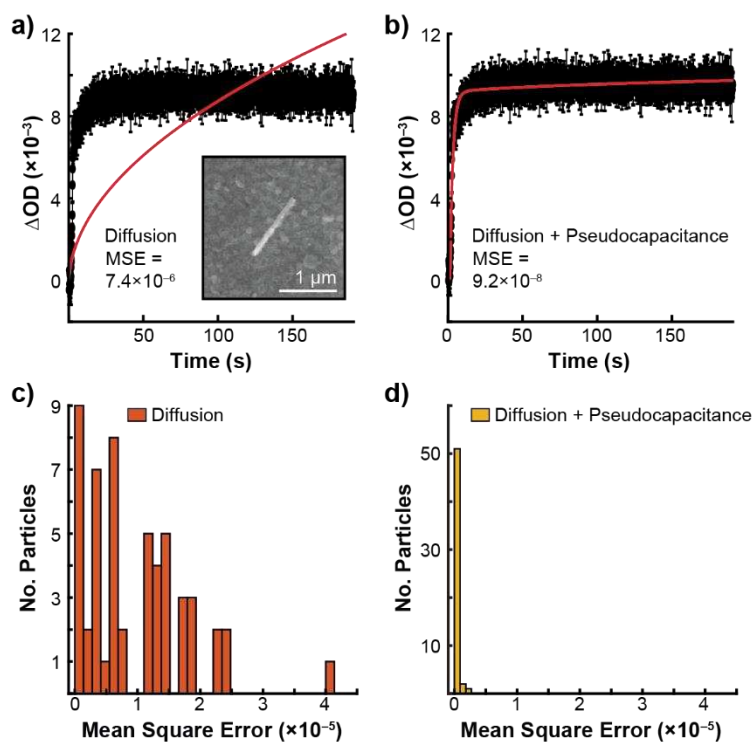


Figure 6.11 – Choosing a fitting routine. a,b) show a single particle ΔOD trace fit with diffusion only (Equation 6-3) and pseudocapacitance plus diffusion (Equation 6-1), respectively at $-1.0 \text{ V vs Ag/AgCl}$. The fits are shown as red lines and the data points are black dots. Error bars represent the standard deviation between three cathodic pulses. Inset shows the single nanoparticle. c) The distributions of mean square error (MSE) between the fit and data points for diffusion fitting. d) The distributions of mean square error between the fit and data points for pseudocapacitance plus diffusion fitting.

Figure 6.12a,b below shows a case at -0.4 V where the diffusion only fit is kept because the MSE is virtually the same for both cases. Indeed, the distribution of errors is much closer at this potential than at -1.0 V (**Figure 6.12b,c**), which accounts for the trends in **Figure 6.7**. If the fit produced negative parameters or MSE values larger than 1×10^{-4} , then the ΔOD trace for that particle at that potential was considered anomalous.

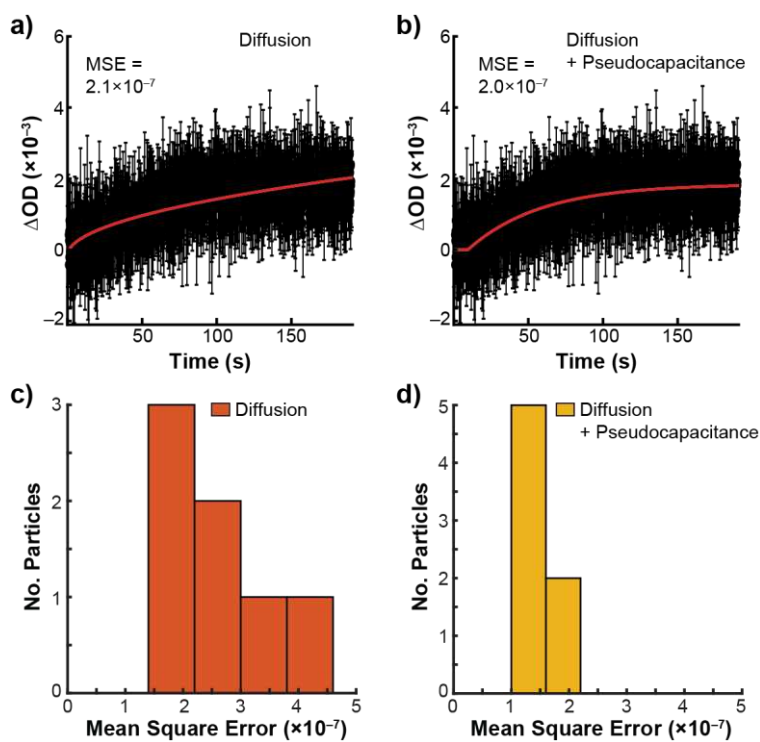


Figure 6.12 – Choosing a fitting routine. a,b) show a single particle ΔOD trace fit with diffusion only (Equation 6-3) and pseudocapacitance plus diffusion (Equation 6-1), respectively at -0.4 V vs Ag/AgCl. The fits are shown as red lines and the data points are black dots. Error bars represent the standard deviation between three cathodic pulses. Inset shows the single nanoparticle. c) The distributions of mean square error (MSE) between the fit and data points for diffusion fitting. d) The distributions of mean square error between the fit and data points for pseudocapacitance plus diffusion fitting.

6.2.2 Quantifying Li^+ Insertion Depth

In order to quantify the ion insertion depth in single nanoparticles the following assumptions were made: (1) The ion insertion depth is equal on all faces except the one on the electrode surface and (2) the nanorods can be approximated as perfect hexagonal prisms. While it is generally thought that the large hexagonal channels along the c -axis are the best for ion diffusion,⁵³ it is assumed that those channels are not orders of magnitude different from the (100) exposed faces. See section 3.2 Characterization for confirmation of the aforementioned morphology. The approximation to hexagonal prisms ignores the step edge defects on the nanorods but is close enough for relative comparison. The following derivation in how the ion insertion depth was quantified by knowing the particle length, width, and percent lithiation based on the optical trace.

Lithium (Li^+) ions driven into the WO_3 nanorods in a uniform manner from all directions with the exception of one face of the prism which is in contact with the electrode surface. It is thought the ions penetrate the surface of the nanorods and reach a depth d within the rod. Three physical measurements may be obtained to calculate d , namely the length of the rod, the maximal width (or diameter), and the percentage of the volume of the rod that contains Li^+ ions. The strategy for approximating the depth of Li^+ penetration will be to translate the problem into a simple root finding problem.

The formula must describe the percentage of the volume of the rod that contains Li^+ ions. In order to do this, slices of the rod that are devoid of Li^+ are subtracted from the volume of a hexagonal prism. The underlying assumptions are the following:

1. The rods are regular hexagons with length l and maximal width w ,
2. The volume of the rod that contains ions is equal to PV where $P \in [0,1]$ is a percentage and V is the volume of the entire rod.
3. The rods naturally occur with an aspect ratio $l:w$ of about 1 or greater.

The last assumption is reasonable by observation of the rods, and plays a crucial role in determining the correct depth of ion penetration, d .

The volume of a solid hexagonal prism depends only on the width of a face, which is denoted by a and its length l . Since adjacent faces of a regular hexagon form an angle of 120° , the triangle formed from the center of the hexagon the vertices of any edge has angles each equal to 60° (**Figure 6.13a**).

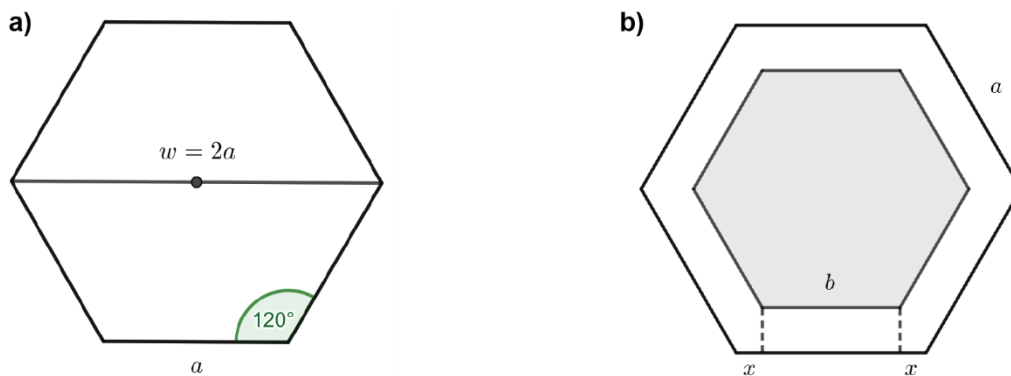


Figure 6.13 – Cross sections of a nanorod. a) By symmetry, we have $w = 2a$ (b) The situation shows that $b + 2x = a$.

This implies the triangle is equilateral and so each edge has length a . Since the maximal width w of the rod is formed by the edges of two equilateral triangles, each with edge length a , it follows that $w = 2a$. The point of this argument is to show that given the measurement w and l , we can appropriately compute the volume of any rod. Since $w = 2a$, we may write the volume of the rod as

$$V = \frac{3\sqrt{3}}{2}a^2l \quad \text{Equation 6-4}$$

Next, the volume of a shell with thickness d will be described. A slight modification is needed to describe the volume of the portion of a rod that contains Li^+ ions. The volume of the shell is obtained by subtracting the volume of a slightly smaller rod which is coaxial to the original rod. Suppose the smaller rod has length h and face width b . In this situation, each face of the smaller coaxial rod should be a distance d from the faces of the outer rod. Thus, $h = l - 2d$. To find b in terms of a and d , it suffices to consider coaxial regular hexagons with edge lengths a and b . First note that by symmetry, the side lengths a and b differ by a small amount x on each side, giving $2x = (a - b)$ (**Figure 6.13b**). Note that the segment joining the vertex of the outer hexagon to the inner forms a 60° angle with the base. A perpendicular line from a vertex of the inner hexagon to the face of the outer hexagon then forms a triangle with height d and base width x and base angle 60° . We then have

$$\sqrt{3} = \tan 60^\circ = \frac{d}{x} = \frac{2d}{a-b} \quad \text{Equation 6-5}$$

Solving for b gives

$$b = a - \frac{2d}{\sqrt{3}} \quad \text{Equation 6-6}$$

Hence the volume of the smaller coaxial rod is given by

$$V' = \frac{3\sqrt{3}}{2} b^2 h = \frac{3\sqrt{3}}{2} \left(a - \frac{2d}{\sqrt{3}} \right)^2 (l - 2d) \quad \text{Equation 6-7}$$

The volume of the shell is then given by subtracting Equation 6-7 from Equation 6-4.

The only thing that remains is subtracting the volume of the face which is protected from ion insertion. The face is seen to have width b , depth d and length h . Thus the face has volume

$$V_{\text{Face}} = bdh = \left(a - \frac{2d}{\sqrt{3}} \right) d(l - 2d) \quad \text{Equation 6-8}$$

Finally, the volume of the portion of the rod that contains ions is given by

$$\begin{aligned} V_{\text{ions}} &= V - V' - V_{\text{Face}} \quad \text{Equation 6-9} \\ &= \frac{3\sqrt{3}}{2} a^2 l - \frac{3\sqrt{3}}{2} \left(a - \frac{2d}{\sqrt{3}} \right)^2 (l - 2d) - \left(a - \frac{2d}{\sqrt{3}} \right) d(l - 2d) \end{aligned}$$

After some simplifying:

$$V_{\text{ions}} = \frac{8}{\sqrt{3}} d^3 - \left(10a + \frac{4l}{\sqrt{3}} \right) d^2 + (3\sqrt{3}a^2 + 5al)d \quad \text{Equation 6-10}$$

Since V_{ions} is a certain percentage of V :

$$V_{\text{ions}} = PV \quad \text{Equation 6-11}$$

for $0 \leq P \leq 1$. Rearranging and using Equation 6-4 and Equation 6-9 and the fact that $w = 2a$, the following root finding problem arises:

$$\frac{8}{\sqrt{3}}d^3 - \left(5w + \frac{4l}{\sqrt{3}}\right)d^2 + \left(\frac{3\sqrt{3}}{4}w^2 + \frac{5}{2}wl\right)d - P\frac{3\sqrt{3}}{8}w^2l = 0 \quad \text{Equation 6-12}$$

All that is left is to decide which root gives the correct approximation of the (positive) quantity d . Note that b is the width of a face of a rod and is therefore nonnegative. Then Equation 6-6 and $w = 2a$ together imply that $d \leq \sqrt{3}w/4$. The case when $l = \sqrt{3}a$ and $P = 1$ gives equality $d = \sqrt{3}w/4$ and the root occurs with multiplicity two.

6.3 Conclusion

In summary, this chapter explored the potential dependent Li-ion insertion in single WO_3 nanorods via optical detection of $(\text{Li}^+\text{-W}^{5+})$ color centers. Optical density measurements during normal pulse voltammetry experiments showed clear scaling relations with time and the applied potential. Specifically, the OD scaled exponentially with time at short times and with the square root of time at long times. These temporal scaling laws could be attributed to capacitive-like and diffusion-limited charge storage. Since the OD measurement reports on a faradaic charge injection reaction, the capacitive-like charge storage process was denoted as pseudocapacitance. The pseudocapacitive charge storage process is both potential and particle dependent, and individual particles can exhibit different charge storage mechanisms at the same applied potential. The wide distribution of local environments on the surface likely leads to the particle dependent onset for the pseudocapacitive process. In addition, the total amount of pseudocapacitive charge in the particles could exceed the total number of surface W atoms. At most, Li-ions penetrate up to 2 units cells below the surface. Longer nanorods store more sub-surface charge than short nanorods, presumably due to a surface step edge gradient that exposes large hexagonal window Li-ion binding sites along the nanorod length or more structural water. Understanding pseudocapacitive charge storage properties in nanoparticles could lead to improved performance for electrochemical technologies such as batteries, electrochromic smart windows, and fuel cells. The methodology presented herein represents a novel approach to quantify pseudocapacitive charge storage in nanostructured electrode materials.

CHAPTER 7: CONCLUSIONS AND OUTLOOK

Electro-optical imaging based on bright field microscopy and in operando electrochemistry, along with a wide array of complementary techniques, gave fundamental insight into a model h-WO₃ nanorod system. This work demonstrates additional evidence for the importance of crystal structure in the ion insertion processes. The local environment dictates where ions bind and move (or get trapped) inside a crystal. Studying h-WO₃ at the single particle and film levels uncovered behaviors that were intrinsic to the material but hidden at the ensemble. Importantly, exponential charge storage dominates at the single particle level, in contrast with square root behavior in a film where particle-particle interactions appear to be the major limiting factor. Further, longer nanorods with more step edge defects appeared to undergo more ion insertion reactions. Step edge defects expose different crystallographic facets (new arrangements of atoms) on the surface of the nanorod and prompted a facet-dependent study on ion insertion in h-WO₃. The addition of a new facet did not change the overall dynamics of ion insertion, but had a large impact on improved reversibility due to less crowded channels at the surface. All charge storage in single h-WO₃ nanorods can be explained by surface or near surface interactions, rather than primarily interior bulk diffusion of ions, highlighting the importance of surface facets. Lastly, there are a distribution of ion insertion kinetics across many potentials. Some individual particles were able to store charge at an exponential rate with low overpotentials, while others required high overpotentials for the slower square root rate. The phenomena responsible for potential dependent kinetics is still up for debate.

Commercial implications center mostly on improved electrochromic smart windows. Single particles tint 4× faster and cycle 20× more reversibly than thin films made of the same particles. A nanostructured electrode architecture that optimizes optical modulation rates and reversibility across large area smart windows was proposed. Further, surface engineering of the electrochromic material is vital to the long-term stability of the smart window. The exposed crystallographic facet can limit the total optical modulation of the film and change the ease that ions can be injected/extracted during repeated cycling.

Applying the principles of the electro-optical microscopy and complementary techniques to gain insight into charge storage dynamics of next generation charge storage materials is the most immediate extension of this work. Orthorhombic Nb₂O₅ (T-Nb₂O₅) and Wadsley-Roth (WR) materials (ternary metal oxides with alternating blocks of metal-oxygen octahedra) are capable of rapid and reversible charge/discharge by ion insertion.^{7,14-16} The exceptional kinetics of each material are attributed to different pathways: diffusion along a atomic plane equivalent binding energy throughout for T-Nb₂O₅,^{16,152} and diffusion through a specific crystallographic direction leading to subtle and reversible expansion/contraction of the block structure characteristic of WR materials,¹⁵³⁻¹⁵⁵ respectively. Both classes of materials rely on structural features for their performance yielding a rich opportunity to impact performance through synthetic manipulation. Probing ion insertion dynamics of samples with different cation disorder or transition metal vacancy in a particular atomic plane will lead to a more fundamental understanding of how structure gives rise to high-rate performance. Note that the electro-optical approach is not limited to transition metal oxides. MXenes are a class 2-D transition metal carbides and nitrides that are showing promise in both the high-rate energy storage and smart window devices, whose electrochromic behavior make them an ideal next target.^{42,156}

I predict electrochemical energy storage technology will advance through two different feedback systems: (1) fundamental materials insight reworking our understanding of ion dynamics in solids that inspire new material design, and (2) new material discovery that warrants novel experiments to understand its seemingly unfounded performance. These processes may be recursive and are certainly not mutually exclusive. Both directions will require development of new methodologies or combinations of existing techniques in novel ways.

BIBLIOGRAPHY

- (1) Augustyn, V.; Simon, P.; Dunn, B. Pseudocapacitive Oxide Materials for High-Rate Electrochemical Energy Storage. *Energy Environ. Sci.* **2014**, *7* (5), 1597–1614.
- (2) Carrilero, I.; González, M.; Anseán, D.; Viera, J. C.; Chacón, J.; Pereirinha, P. G. Redesigning European Public Transport: Impact of New Battery Technologies in the Design of Electric Bus Fleets. *Transp. Res. Procedia* **2018**, *33*, 195–202. <https://doi.org/10.1016/j.trpro.2018.10.092>.
- (3) Alhadri, M.; Mohammed, A. H.; Farhad, S. Comparison of Duty-Cycle of a Lithium-Ion Battery for Electric Airplane and Electric Vehicle Applications; 2018; pp 2018-01–0666. <https://doi.org/10.4271/2018-01-0666>.
- (4) Zhao, W.; Choi, W.; Yoon, W.-S. Nanostructured Electrode Materials for Rechargeable Lithium-Ion Batteries. *J. Electrochem. Sci. Technol.* **2020**, *11* (3), 195–219. <https://doi.org/10.33961/jecst.2020.00745>.
- (5) Peters, G. P.; Marland, G.; Le Quéré, C.; Boden, T.; Canadell, J. G.; Raupach, M. R. Rapid Growth in CO₂ Emissions after the 2008–2009 Global Financial Crisis. *Nat. Clim. Change* **2012**, *2* (1), 2–4. <https://doi.org/10.1038/nclimate1332>.
- (6) Ragone, D. V. Review of Battery Systems for Electrically Powered Vehicles; 1968; p 680453. <https://doi.org/10.4271/680453>.
- (7) Augustyn, V.; Come, J.; Lowe, M. A.; Kim, J. W.; Taberna, P.-L.; Tolbert, S. H.; Abruña, H. D.; Simon, P.; Dunn, B. High-Rate Electrochemical Energy Storage through Li⁺ Intercalation Pseudocapacitance. *Nat. Mater.* **2013**, *12* (6), 518–522. <https://doi.org/10.1038/nmat3601>.
- (8) Dunn, B.; Kamath, H.; Tarascon, J.-M. Electrical Energy Storage for the Grid: A Battery of Choices. *Science* **2011**, *334* (6058), 928–935. <https://doi.org/10.1126/science.1212741>.
- (9) Choi, C.; Ashby, D. S.; Butts, D. M.; DeBlock, R. H.; Wei, Q.; Lau, J.; Dunn, B. Achieving High Energy Density and High Power Density with Pseudocapacitive Materials. *Nat. Rev. Mater.* **2019**. <https://doi.org/10.1038/s41578-019-0142-z>.
- (10) Aricò, A. S.; Bruce, P.; Scrosati, B.; Tarascon, J.-M.; van Schalkwijk, W. Nanostructured Materials for Advanced Energy Conversion and Storage Devices. *Nat. Mater.* **2005**, *4*, 366.
- (11) Wagemaker, M.; Mulder, F. M. Properties and Promises of Nanosized Insertion Materials for Li-Ion Batteries. *Acc. Chem. Res.* **2013**, *46* (5), 1206–1215. <https://doi.org/10.1021/ar2001793>.
- (12) Ellis, B.; Subramanya Herle, P.; Rho, Y. H.; Nazar, L. F.; Dunlap, R.; Perry, L. K.; Ryan, D. H. Nanostructured Materials for Lithium-Ion Batteries: Surface Conductivity vs. Bulk Ion/Electron Transport. *Faraday Discuss.* **2007**, *134*, 119–141; discussion 215–233, 415–419. <https://doi.org/10.1039/b602698b>.
- (13) Lu, J.; Chen, Z.; Ma, Z.; Pan, F.; Curtiss, L. A.; Amine, K. The Role of Nanotechnology in the Development of Battery Materials for Electric Vehicles. *Nat. Nanotechnol.* **2016**, *11* (12), 1031–1038. <https://doi.org/10.1038/nnano.2016.207>.
- (14) Griffith, K. J.; Harada, Y.; Egusa, S.; Ribas, R. M.; Monteiro, R. S.; Von Dreele, R. B.; Cheetham, A. K.; Cava, R. J.; Grey, C. P.; Goodenough, J. B. Titanium Niobium Oxide: From Discovery to Application in Fast-Charging Lithium-Ion Batteries. *Chem. Mater.* **2021**, *33* (1), 4–18. <https://doi.org/10.1021/acs.chemmater.0c02955>.
- (15) Griffith, K. J.; Wiaderek, K. M.; Cibir, G.; Marbella, L. E.; Grey, C. P. Niobium Tungsten Oxides for High-Rate Lithium-Ion Energy Storage. *Nature* **2018**, *559* (7715), 556–563. <https://doi.org/10.1038/s41586-018-0347-0>.

- (16) Griffith, K. J.; Forse, A. C.; Griffin, J. M.; Grey, C. P. High-Rate Intercalation without Nanostructuring in Metastable Nb₂O₅ Bronze Phases. *J. Am. Chem. Soc.* **2016**, *138* (28), 8888–8899. <https://doi.org/10.1021/jacs.6b04345>.
- (17) Tjong, S.-C. *Nanocrystalline Materials: Their Synthesis-Structure-Property Relationships and Applications*; Newnes, 2013.
- (18) P. Carvalho, R.; N. Marchiori, C. F.; Oltean, V.-A.; Renault, S.; Willhammar, T.; Gómez, C. P.; Moyses Araujo, C.; Brandell, D. Structure–Property Relationships in Organic Battery Anode Materials: Exploring Redox Reactions in Crystalline Na- and Li-Benzene Diacrylate Using Combined Crystallography and Density Functional Theory Calculations. *Mater. Adv.* **2021**, *2* (3), 1024–1034. <https://doi.org/10.1039/D0MA00900H>.
- (19) Wang, Y.; Zhang, W.; Chen, L.; Shi, S.; Liu, J. Quantitative Description on Structure–Property Relationships of Li-Ion Battery Materials for High-Throughput Computations. *Sci. Technol. Adv. Mater.* **2017**, *18* (MGI), 134–146. <https://doi.org/10.1080/14686996.2016.1277503>.
- (20) Vasconcelos, L. S. de; Xu, R.; Li, J.; Zhao, K. Grid Indentation Analysis of Mechanical Properties of Composite Electrodes in Li-Ion Batteries. *Extreme Mech. Lett.* **2016**, *9*, 495–502. <https://doi.org/10.1016/j.eml.2016.03.002>.
- (21) Huang, J. Y.; Zhong, L.; Wang, C. M.; Sullivan, J. P.; Xu, W.; Zhang, L. Q.; Mao, S. X.; Hudak, N. S.; Liu, X. H.; Subramanian, A.; Fan, H.; Qi, L.; Kushima, A.; Li, J. In Situ Observation of the Electrochemical Lithiation of a Single SnO₂ Nanowire Electrode. *Science* **2010**, *330* (6010), 1515–1520.
- (22) Qi, K.; Wei, J.; Sun, M.; Huang, Q.; Li, X.; Xu, Z.; Wang, W.; Bai, X. Real-Time Observation of Deep Lithiation of Tungsten Oxide Nanowires by In Situ Electron Microscopy. *Angew. Chem. Int. Ed.* **2015**, *54* (50), 15222–15225. <https://doi.org/10.1002/anie.201508112>.
- (23) Wu, Y.; Liu, N. Visualizing Battery Reactions and Processes by Using In Situ and In Operando Microscopies. *Chem* **2018**, *4* (3), 438–465. <https://doi.org/10.1016/j.chempr.2017.12.022>.
- (24) Basak, S.; Migunov, V.; Tavabi, A. H.; George, C.; Lee, Q.; Rosi, P.; Arszewska, V.; Ganapathy, S.; Vijay, A.; Ooms, F.; Schierholz, R.; Tempel, H.; Kungl, H.; Mayer, J.; Dunin-Borkowski, R. E.; Eichel, R.-A.; Wagemaker, M.; Kelder, E. M. Operando Transmission Electron Microscopy Study of All-Solid-State Battery Interface: Redistribution of Lithium among Interconnected Particles. *ACS Appl. Energy Mater.* **2020**, *3* (6), 5101–5106. <https://doi.org/10.1021/acsaem.0c00543>.
- (25) Wolf, M.; May, B. M.; Cabana, J. Visualization of Electrochemical Reactions in Battery Materials with X-Ray Microscopy and Mapping. *Chem. Mater.* **2017**, *29* (8), 3347–3362.
- (26) Deb, A.; Bergmann, U.; Cairns, E. J.; Cramer, S. P. X-Ray Absorption Spectroscopy Study of the Li_xFePO₄ Cathode during Cycling Using a Novel Electrochemical In Situ Reaction Cell. *J. Synchrotron Radiat.* **2004**, *11* (6), 497–504.
- (27) Yu, Y.-S.; Kim, C.; Liu, Y.; van der Ven, A.; Meng, Y. S.; Kostecki, R.; Cabana, J. Nonequilibrium Pathways during Electrochemical Phase Transformations in Single Crystals Revealed by Dynamic Chemical Imaging at Nanoscale Resolution. *Adv. Energy Mater.* **2015**, *5* (7), 1402040. <https://doi.org/10.1002/aenm.201402040>.
- (28) Wang, J.; Karen Chen-Wiegart, Y.; Eng, C.; Shen, Q.; Wang, J. Visualization of Anisotropic-Isotropic Phase Transformation Dynamics in Battery Electrode Particles. *Nat. Commun.* **2016**, *7* (1), 12372. <https://doi.org/10.1038/ncomms12372>.
- (29) Jiang, D.; Jiang, Y. Y.; Li, Z. M.; Liu, T.; Wo, X.; Fang, Y. M.; Tao, N. J.; Wang, W.; Chen, H. Y. Optical Imaging of Phase Transition and Li-Ion Diffusion Kinetics of Single LiCoO₂ Nanoparticles During Electrochemical Cycling. *J. Am. Chem. Soc.* **2017**, *139* (1), 186–192.
- (30) Li, J.-T.; Zhou, Z.-Y.; Broadwell, I.; Sun, S.-G. In-Situ Infrared Spectroscopic Studies of Electrochemical Energy Conversion and Storage. *Acc. Chem. Res.* **2012**, *45* (4), 485–494.
- (31) Stöckle, R. M.; Suh, Y. D.; Deckert, V.; Zenobi, R. Nanoscale Chemical Analysis by Tip-Enhanced Raman Spectroscopy. *Chem. Phys. Lett.* **2000**, *318* (1), 131–136.
- (32) Stancovski, V.; Badilescu, S. In Situ Raman Spectroscopy–Electrochemical Studies of Lithium-Ion Battery Materials: A Historical Overview. *J. Appl. Electrochem.* **2014**, *44* (1), 23–43.

- (33) Luo, Y.; Cai, W.-B.; Xing, X.; Scherson, D. A. In Situ, Time-Resolved Raman Spectromicrotopography of an Operating Lithium-Ion Battery. *Electrochem. Solid-State Lett.* **2004**, *7* (1), E1–E5.
- (34) Penders, J.; Pence, I. J.; Horgan, C. C.; Bergholt, M. S.; Wood, C. S.; Najer, A.; Kauscher, U.; Nagelkerke, A.; Stevens, M. M. Single Particle Automated Raman Trapping Analysis. *Nat. Commun.* **2018**, *9* (1), 4256. <https://doi.org/10.1038/s41467-018-06397-6>.
- (35) Yamanaka, T.; Okazaki, K.; Ogumi, Z.; Abe, T. Reactivity and Mechanisms in Fluoride Shuttle Battery Reactions: Difference between Orthorhombic and Cubic BiF₃ Single Microparticles. *ACS Appl. Energy Mater.* **2019**, *2* (12), 8801–8808. <https://doi.org/10.1021/acsaem.9b01803>.
- (36) Ilott, A. J.; Mohammadi, M.; Chang, H. J.; Grey, C. P.; Jerschow, A. Real-Time 3D Imaging of Microstructure Growth in Battery Cells Using Indirect MRI. *Proc. Natl. Acad. Sci.* **2016**, *113* (39), 10779–10784.
- (37) Li, X.; Tang, M. X.; Feng, X. Y.; Hung, I.; Rose, A.; Chien, P. H.; Gan, Z. H.; Hu, Y. Y. Lithiation and Delithiation Dynamics of Different Li Sites in Li-Rich Battery Cathodes Studied by Operando Nuclear Magnetic Resonance. *Chem. Mater.* **2017**, *29* (19), 8282–8291.
- (38) Ilott, A. J.; Jerschow, A. Super-Resolution Surface Microscopy of Conductors Using Magnetic Resonance. *Sci. Rep.* **2017**, *7*, 7.
- (39) Granqvist, C. G. Chapter 23 - Systematics for the Electrochromism in Transition Metal Oxides. In *Handbook of Inorganic Electrochromic Materials*; Granqvist, C. G., Ed.; Elsevier Science B.V.: Amsterdam, 1995; pp 413–419.
- (40) Manka, D.; Ivers-Tiffée, E. Electro-Optical Measurements of Lithium Intercalation/de-Intercalation at Graphite Anode Surfaces. *Electrochimica Acta* **2015**, *186*, 642–653.
- (41) Jebaraj, A. J. J.; Scherson, D. A. Microparticle Electrodes and Single Particle Microbatteries: Electrochemical and in Situ MicroRaman Spectroscopic Studies. *Acc. Chem. Res.* **2013**, *46* (5), 1192–1205.
- (42) Valurouthu, G.; Maleski, K.; Kurra, N.; Han, M.; Hantanasirisakul, K.; Sarycheva, A.; Gogotsi, Y. Tunable Electrochromic Behavior of Titanium-Based MXenes. *Nanoscale* **2020**, *12* (26), 14204–14212. <https://doi.org/10.1039/D0NR02673E>.
- (43) Jiang, X.; Van den Broek, W.; Koch, C. T. Inverse Dynamical Photon Scattering (IDPS): An Artificial Neural Network Based Algorithm for Three-Dimensional Quantitative Imaging in Optical Microscopy. *Opt. Express* **2016**, *24* (7), 7006–7018.
- (44) Delichere, P.; Falaras, P.; M. Froment; Goff, A. Hugot-Le; Agius, B. ELECTROCHROMISM IN ANODIC WO₃ FILMS I: PREPARATION AND PHYSICOCHEMICAL PROPERTIES OF FILMS IN THE VIRGIN AND COLOURED STATES. *Thin Solid Films* **1988**, *161*, 35–46. [https://doi.org/10.1016/0040-6090\(88\)90233-7](https://doi.org/10.1016/0040-6090(88)90233-7).
- (45) Oi, J.; Kishimoto, A.; Kudo, T.; Hiratani, M. Hexagonal Tungsten Trioxide Obtained from Peroxopolytungstate and Reversible Lithium Electro-Intercalation into Its Framework. *J. Solid State Chem.* **1992**, *96* (1), 13–19. [https://doi.org/10.1016/S0022-4596\(05\)80292-0](https://doi.org/10.1016/S0022-4596(05)80292-0).
- (46) Wang, J.; Khoo, E.; Lee, P. S.; Ma, J. Synthesis, Assembly, and Electrochromic Properties of Uniform Crystalline WO₃ Nanorods. *J. Phys. Chem. C* **2008**, *112* (37), 14306–14312. <https://doi.org/10.1021/jp804035r>.
- (47) Klein, J. D.; Yen, A. Crystal Phase Effects in Electrochromic WO₃. *MRS Proc.* **1992**, *293*, 389. <https://doi.org/10.1557/PROC-293-389>.
- (48) Lin, F.; Cheng, J.; Engtrakul, C.; Dillon, A. C.; Nordlund, D.; Moore, R. G.; Weng, T.-C.; Williams, S. K. R.; Richards, R. M. In Situ Crystallization of High Performing WO₃-Based Electrochromic Materials and the Importance for Durability and Switching Kinetics. *J. Mater. Chem.* **2012**, *22* (33), 16817. <https://doi.org/10.1039/c2jm32742b>.
- (49) Granqvist, C. G.; Arvizu, M. A.; Bayrak Pehlivan, I.; Qu, H.-Y.; Wen, R.-T.; Niklasson, G. A. Electrochromic Materials and Devices for Energy Efficiency and Human Comfort in Buildings: A Critical Review. *Electrochimica Acta* **2018**, *259*, 1170–1182. <https://doi.org/10.1016/j.electacta.2017.11.169>.

- (50) Runnerstrom, E. L.; Llordés, A.; Lounis, S. D.; Milliron, D. J. Nanostructured Electrochromic Smart Windows: Traditional Materials and NIR-Selective Plasmonic Nanocrystals. *Chem Commun* **2014**, 50 (73), 10555–10572. <https://doi.org/10.1039/C4CC03109A>.
- (51) Lokhande, V.; Lokhande, A.; Namkoong, G.; Kim, J. H.; Ji, T. Charge Storage in WO₃ Polymorphs and Their Application as Supercapacitor Electrode Material. *Results Phys.* **2019**, 12, 2012–2020. <https://doi.org/10.1016/j.rinp.2019.02.012>.
- (52) Hibino, M. Electrochemical Lithium Intercalation into a Hexagonal WO₃ Framework and Its Structural Change. *Solid State Ion.* **2000**, 135 (1–4), 61–69. [https://doi.org/10.1016/S0167-2738\(00\)00332-5](https://doi.org/10.1016/S0167-2738(00)00332-5).
- (53) Slade, R.; West, B.; Hall, G. Chemical and Electrochemical Mixed Alkali Metal Insertion Chemistry of the Hexagonal Tungsten Trioxide Framework. *Solid State Ion.* **1989**, 32–33, 154–161. [https://doi.org/10.1016/0167-2738\(89\)90216-6](https://doi.org/10.1016/0167-2738(89)90216-6).
- (54) Balaji, S.; Djaoued, Y.; Albert, A.-S.; Ferguson, R. Z.; Brüning, R. Hexagonal Tungsten Oxide Based Electrochromic Devices: Spectroscopic Evidence for the Li Ion Occupancy of Four-Coordinated Square Windows. *Chem. Mater.* **2009**, 21 (7), 1381–1389.
- (55) Wang, Y.; Runnerstrom, E. L.; Milliron, D. J. Switchable Materials for Smart Windows. *Annu. Rev. Chem. Biomol. Eng.* **2016**, 7 (1), 283–304. <https://doi.org/10.1146/annurev-chembioeng-080615-034647>.
- (56) Lee, S.-H.; Cheong, H. M.; Zhang, J.-G.; Mascarenhas, A.; Benson, D. K.; Deb, S. K. Electrochromic Mechanism in A-WO₃-y Thin Films. *Appl. Phys. Lett.* **1999**, 74 (2), 242–244. <https://doi.org/10.1063/1.123268>.
- (57) Lee, S. Effect of Crystallinity on Electrochromic Mechanism of Li_xWO₃ Thin Films. *Solid State Ion.* **2003**, 156 (3–4), 447–452. [https://doi.org/10.1016/S0167-2738\(02\)00732-4](https://doi.org/10.1016/S0167-2738(02)00732-4).
- (58) Jin, A.; Chen, W.; Zhu, Q.; Jian, Z. Multi-Electrochromism Behavior and Electrochromic Mechanism of Electrodeposited Molybdenum Doped Vanadium Pentoxide Films. *Electrochimica Acta* **2010**, 55 (22), 6408–6414. <https://doi.org/10.1016/j.electacta.2010.06.047>.
- (59) Hersh, H. N.; Kramer, W. E.; McGee, J. H. Mechanism of Electrochromism in WO₃. *Appl. Phys. Lett.* **1975**, 27 (12), 646–648. <https://doi.org/10.1063/1.88346>.
- (60) Luo, Z.; Liu, L.; Yang, X.; Luo, X.; Bi, P.; Fu, Z.; Pang, A.; Li, W.; Yi, Y. Revealing the Charge Storage Mechanism of Nickel Oxide Electrochromic Supercapacitors. *ACS Appl. Mater. Interfaces* **2020**, 12 (35), 39098–39107. <https://doi.org/10.1021/acsami.0c09606>.
- (61) Dong, D.; Djaoued, H.; Vienneau, G.; Robichaud, J.; Brown, D.; Brüning, R.; Djaoued, Y. Electrochromic and Colorimetric Properties of Anodic NiO Thin Films: Uncovering Electrochromic Mechanism of NiO. *Electrochimica Acta* **2020**, 335, 135648. <https://doi.org/10.1016/j.electacta.2020.135648>.
- (62) Deb, S. K. Opportunities and Challenges in Science and Technology of WO₃ for Electrochromic and Related Applications. *Sol. Energy Mater. Sol. Cells* **2008**, 92 (2), 245–258. <https://doi.org/10.1016/j.solmat.2007.01.026>.
- (63) Kamal, H.; Akl, A. A.; Abdel-Hady, K. Influence of Proton Insertion on the Conductivity, Structural and Optical Properties of Amorphous and Crystalline Electrochromic WO₃ Films. *Phys. B Condens. Matter* **2004**, 349 (1), 192–205. <https://doi.org/10.1016/j.physb.2004.03.088>.
- (64) Tsuboi, A.; Nakamura, K.; Kobayashi, N. A Localized Surface Plasmon Resonance-Based Multicolor Electrochromic Device with Electrochemically Size-Controlled Silver Nanoparticles. *Adv. Mater.* **2013**, 25 (23), 3197–3201. <https://doi.org/10.1002/adma.201205214>.
- (65) Granqvist, C. G. *Handbook of Inorganic Electrochromic Materials*; Elsevier Science: Amsterdam, 1995.
- (66) Aller Pellitero, M.; del Campo, F. J. Electrochromic Sensors: Innovative Devices Enabled by Spectroelectrochemical Methods. *Curr. Opin. Electrochem.* **2019**, 15, 66–72. <https://doi.org/10.1016/j.coelec.2019.03.004>.

- (67) Heo, S.; Dahlman, C. J.; Staller, C. M.; Jiang, T.; Dolocan, A.; Korgel, B. A.; Milliron, D. J. Enhanced Coloration Efficiency of Electrochromic Tungsten Oxide Nanorods by Site Selective Occupation of Sodium Ions. *Nano Lett.* **2020**, *20* (3), 2072–2079. <https://doi.org/10.1021/acs.nanolett.0c00052>.
- (68) Heo, S.; Cho, S. H.; Dahlman, C. J.; Agrawal, A.; Milliron, D. J. Influence of Crystalline and Shape Anisotropy on Electrochromic Modulation in Doped Semiconductor Nanocrystals. *ACS Energy Lett.* **2020**, 2662–2670. <https://doi.org/10.1021/acsenerylett.0c01236>.
- (69) Evans, R. C.; Ellingworth, A.; Cashen, C. J.; Weinberger, C. R.; Sambur, J. B. Influence of Single-Nanoparticle Electrochromic Dynamics on the Durability and Speed of Smart Windows. *Proc. Natl. Acad. Sci.* **2019**, *116* (26), 12666–12671. <https://doi.org/10.1073/pnas.1822007116>.
- (70) Daniel C. Harris; Michael Bertolucci. *Symmetry and Spectroscopy: An Introduction to Vibrational and Electronic Spectroscopy*; Dover Publications Inc.: New York, 1989.
- (71) Zalyubovskiy, S. J.; Bogdanova, M.; Deinega, A.; Lozovik, Y.; Pris, A. D.; An, K. H.; Hall, W. P.; Potyrailo, R. A. Theoretical Limit of Localized Surface Plasmon Resonance Sensitivity to Local Refractive Index Change and Its Comparison to Conventional Surface Plasmon Resonance Sensor. *JOSA A* **2012**, *29* (6), 994–1002. <https://doi.org/10.1364/JOSAA.29.000994>.
- (72) Schulz, L. G. An Experimental Confirmation of the Drude Free Electron Theory of the Optical Properties of Metals for Silver, Gold, and Copper in the Near Infrared. *J. Opt. Soc. Am.* **1954**, *44* (7), 540. <https://doi.org/10.1364/JOSA.44.000540>.
- (73) Scarminio, J.; Urbano, A.; Gardes, B. The Beer-Lambert Law for Electrochromic Tungsten Oxide Thin Films. *Mater. Chem. Phys.* **1999**, *61* (2), 143–146.
- (74) Kondalkar, V. V.; Mali, S. S.; Kharade, R. R.; Khot, K. V.; Patil, P. B.; Mane, R. M.; Choudhury, S.; Patil, P. S.; Hong, C. K.; Kim, J. H.; Bhosale, P. N. High Performing Smart Electrochromic Device Based on Honeycomb Nanostructured H-WO₃ Thin Films: Hydrothermal Assisted Synthesis. *Dalton Trans.* **2015**, *44* (6), 2788–2800. <https://doi.org/10.1039/C4DT02953D>.
- (75) Evans, R. C.; Nilsson, Z. N.; Sambur, J. B. High-Throughput Single-Nanoparticle-Level Imaging of Electrochemical Ion Insertion Reactions. *Anal. Chem.* **2019**, *91* (23), 14983–14991. <https://doi.org/10.1021/acs.analchem.9b03487>.
- (76) Dang, W.; Wang, W.; Yang, Y.; Wang, Y.; Huang, J.; Fang, X.; Wu, L.; Rong, Z.; Chen, X.; Li, X.; Huang, L.; Tang, X. One-Step Hydrothermal Synthesis of 2D WO₃ Nanoplates@ Graphene Nanocomposite with Superior Anode Performance for Lithium Ion Battery. *Electrochimica Acta* **2019**, *313*, 99–108. <https://doi.org/10.1016/j.electacta.2019.04.184>.
- (77) He, Y.; Gu, M.; Xiao, H.; Luo, L.; Shao, Y.; Gao, F.; Du, Y.; Mao, S. X.; Wang, C. Atomistic Conversion Reaction Mechanism of WO₃ in Secondary Ion Batteries of Li, Na, and Ca. *Angew. Chem.* **2016**, *128* (21), 6352–6355. <https://doi.org/10.1002/ange.201601542>.
- (78) Wang, J.; Gao, L. Wet Chemical Synthesis of Ultralong and Straight Single-Crystalline ZnO Nanowires and Their Excellent UV Emission Properties. *J. Mater. Chem.* **2003**, *13* (10), 2551. <https://doi.org/10.1039/b307565f>.
- (79) Juárez, B. H.; López, C.; Alonso, C. Formation of Zinc Inverted Opals on Indium Tin Oxide and Silicon Substrates by Electrochemical Deposition. *J. Phys. Chem. B* **2004**, *108* (43), 16708–16712. <https://doi.org/10.1021/jp047475n>.
- (80) Stephen G. Lipson; Henry Lipson; Khurram Kazi. *Optical Physics*; Cambridge: United Kingdom.
- (81) Lee, Y.; Lee, T.; Jang, W.; Soon, A. Unraveling the Intercalation Chemistry of Hexagonal Tungsten Bronze and Its Optical Responses. *Chem. Mater.* **2016**, *28* (13), 4528–4535.
- (82) Bueno, P. R.; Leite, E. R. Nanostructured Li Ion Insertion Electrodes. 1. Discussion on Fast Transport and Short Path for Ion Diffusion. *J. Phys. Chem. B* **2003**, *107* (34), 8868–8877. <https://doi.org/10.1021/jp034513e>.
- (83) Vuillemin, B.; Bohnke, O. Kinetics Study and Modelling of the Electrochromic Phenomenon in Amorphous Tungsten Trioxide Thin Films in Acid and Lithium Electrolytes. *Solid State Ion.* **1994**, *68* (3), 257–267.
- (84) Faughnan, B. W.; Crandall, R. S.; Lampert, M. A. Model for the Bleaching of WO₃ Electrochromic Films by an Electric Field. *Appl Phys Lett* **1975**, *27* (5), 275–277.

- (85) Crandall, R. S.; Faughnan, B. W. Dynamics of Coloration of Amorphous Electrochromic Films of WO_3 at Low Voltages. *Appl. Phys. Lett.* **1976**, *28* (2), 95–97. <https://doi.org/10.1063/1.88653>.
- (86) McEvoy, T. M.; Stevenson, K. J. Spatially Resolved Measurement of Inhomogeneous Electrocoloration/Insertion in Polycrystalline Molybdenum Oxide Thin Films via Chronoabsorptometric Imaging. *J. Am. Chem. Soc.* **2003**, *125* (28), 8438–8439.
- (87) McEvoy, T. M.; Stevenson, K. J. Spatially Resolved Imaging of Inhomogeneous Charge Transfer Behavior in Polymorphous Molybdenum Oxide. I. Correlation of Localized Structural, Electronic, and Chemical Properties Using Conductive Probe Atomic Force Microscopy and Raman Microprobe Spectroscopy. *Langmuir* **2005**, *21* (8), 3521–3528. <https://doi.org/10.1021/la047276v>.
- (88) Simon, B.; T., E. M.; Bernhard, L.-W.; J., K. P. In Situ Monitoring of Lateral Hydrogen Diffusion in Amorphous and Polycrystalline WO_3 Thin Films. *Adv. Mater. Interfaces* **2018**, *5* (6), 1701587.
- (89) R. Roldán; Y.E. Romanyuk. Dynamics in Electrochromic Windows Interpreted with an Extended Logistic Model. *J. Electrochem. Soc.* **2016**, *163* (8), E2235–E2240.
- (90) Wang, J.; Polleux, J.; Lim, J.; Dunn, B. Pseudocapacitive Contributions to Electrochemical Energy Storage in TiO_2 (Anatase) Nanoparticles. *J. Phys. Chem. C* **2007**, *111* (40), 14925–14931. <https://doi.org/10.1021/jp074464w>.
- (91) Yang, P.; Sun, P.; Du, L.; Liang, Z.; Xie, W.; Cai, X.; Huang, L.; Tan, S.; Mai, W. Quantitative Analysis of Charge Storage Process of Tungsten Oxide That Combines Pseudocapacitive and Electrochromic Properties. *J. Phys. Chem. C* **2015**, *119* (29), 16483–16489.
- (92) Peihua, Y.; Peng, S.; Zhisheng, C.; Langhuan, H.; Xiang, C.; Shaozao, T.; Jinhui, S.; Wenjie, M. Large-Scale Fabrication of Pseudocapacitive Glass Windows That Combine Electrochromism and Energy Storage. *Angew. Chem. Int. Ed.* **2014**, *53* (44), 11935–11939.
- (93) Zhu, M.; Meng, W.; Huang, Y.; Huang, Y.; Zhi, C. Proton-Insertion-Enhanced Pseudocapacitance Based on the Assembly Structure of Tungsten Oxide. *ACS Appl. Mater. Interfaces* **2014**, *6* (21), 18901–18910. <https://doi.org/10.1021/am504756u>.
- (94) Jo, C.; Hwang, I.; Lee, J.; Lee, C. W.; Yoon, S. Investigation of Pseudocapacitive Charge-Storage Behavior in Highly Conductive Ordered Mesoporous Tungsten Oxide Electrodes. *J. Phys. Chem. C* **2011**, *115* (23), 11880–11886.
- (95) Giannuzzi, R.; Scarfiello, R.; Sibillano, T.; Nobile, C.; Grillo, V.; Giannini, C.; Cozzoli, P. D.; Manca, M. From Capacitance-Controlled to Diffusion-Controlled Electrochromism in One-Dimensional Shape-Tailored Tungsten Oxide Nanocrystals. *Nano Energy* **2017**, *41*, 634–645.
- (96) Xie, F. Y.; Gong, L.; Liu, X.; Tao, Y. T.; Zhang, W. H.; Chen, S. H.; Meng, H.; Chen, J. XPS Studies on Surface Reduction of Tungsten Oxide Nanowire Film by Ar^+ Bombardment. *J. Electron Spectrosc. Relat. Phenom.* **2012**, *185* (3–4), 112–118. <https://doi.org/10.1016/j.elspec.2012.01.004>.
- (97) Darmawi, S.; Burkhardt, S.; Leichtweiss, T.; Weber, D. A.; Wenzel, S.; Janek, J.; Elm, M. T.; Klar, P. J. Correlation of Electrochromic Properties and Oxidation States in Nanocrystalline Tungsten Trioxide. *Phys. Chem. Chem. Phys.* **2015**, *17* (24), 15903–15911.
- (98) Miao, B.; Zeng, W.; Hussain, S.; Mei, Q.; Xu, S.; Zhang, H.; Li, Y.; Li, T. Large Scale Hydrothermal Synthesis of Monodisperse Hexagonal WO_3 Nanowire and the Growth Mechanism. *Mater. Lett.* **2015**, *147*, 12–15. <https://doi.org/10.1016/j.matlet.2015.02.020>.
- (99) Martin, J. J.; Armington, A. F. Effect of Growth Rate on Quartz Defects. *J. Cryst. Growth* **1983**, *62* (1), 203–206. [https://doi.org/10.1016/0022-0248\(83\)90026-X](https://doi.org/10.1016/0022-0248(83)90026-X).
- (100) Zhou, X.; Andoy, N. M.; Liu, G.; Choudhary, E.; Han, K.-S.; Shen, H.; Chen, P. Quantitative Super-Resolution Imaging Uncovers Reactivity Patterns on Single Nanocatalysts. *Nat. Nanotechnol.* **2012**, *7* (4), 237–241. <https://doi.org/10.1038/nnano.2012.18>.
- (101) Lewerenz, H. J.; Heller, A.; DiSalvo, F. J. Relationship between Surface Morphology and Solar Conversion Efficiency of Tungsten Diselenide Photoanodes. *J. Am. Chem. Soc.* **1980**, *102* (6), 1877–1880. <https://doi.org/10.1021/ja00526a019>.
- (102) Sun, W.; Yeung, M. T.; Lech, A. T.; Lin, C.-W.; Lee, C.; Li, T.; Duan, X.; Zhou, J.; Kaner, R. B. High Surface Area Tunnels in Hexagonal WO_3 . *Nano Lett.* **2015**, *15* (7), 4834–4838. <https://doi.org/10.1021/acs.nanolett.5b02013>.

- (103) Bisquert, J.; Garcia-Belmonte, G.; Fabregat-Santiago, F. Modelling the Electric Potential Distribution in the Dark in Nanoporous Semiconductor Electrodes. *J. Solid State Electrochem.* **1999**, *3* (6), 337–347. <https://doi.org/10.1007/s100080050164>.
- (104) Niklasson, G. A.; Berggren, L.; Larsson, A.-L. Electrochromic Tungsten Oxide: The Role of Defects. *Sol. Energy Mater. Sol. Cells* **2004**, *84* (1–4), 315–328. <https://doi.org/10.1016/j.solmat.2004.01.045>.
- (105) Eells, W. C. Formulas for Probable Errors of Coefficients of Correlation. *J. Am. Stat. Assoc.* **1929**, *24* (166), 170–173. <https://doi.org/10.1080/01621459.1929.10502524>.
- (106) Cheng, K. H.; Jacobson, A. J.; Whittingham, M. S. Hexagonal Tungsten Trioxide and Its Intercalation Chemistry. *Solid State Ion.* **1981**, *5*, 355–358. [https://doi.org/10.1016/0167-2738\(81\)90266-6](https://doi.org/10.1016/0167-2738(81)90266-6).
- (107) Wen, R.-T.; Granqvist, C. G.; Niklasson, G. A. Eliminating Degradation and Uncovering Ion-Trapping Dynamics in Electrochromic WO₃ Thin Films. *Nat. Mater.* **2015**, *14*, 996.
- (108) Lian, C.; Xiao, X.; Chen, Z.; Liu, Y.; Zhao, E.; Wang, D.; Chen, C. Preparation of Hexagonal Ultrathin WO₃ Nano-Ribbons and Their Electrochemical Performance as an Anode Material in Lithium Ion Batteries. *Nano Res.* **2016**, *9* (2), 435–441. <https://doi.org/10.1007/s12274-015-0924-6>.
- (109) Dong, D.; Wang, W.; Rougier, A.; Barnabé, A.; Dong, G.; Zhang, F.; Diao, X. Lithium Trapping as a Degradation Mechanism of the Electrochromic Properties of All-Solid-State WO₃/NiO Devices. *J. Mater. Chem. C* **2018**, *6* (37), 9875–9889. <https://doi.org/10.1039/C8TC01372A>.
- (110) Liu, Z. Y.; Brady, B. K.; Carter, R. N.; Litteer, B.; Budinski, M.; Hyun, J. K.; Muller, D. A. Characterization of Carbon Corrosion-Induced Structural Damage of PEM Fuel Cell Cathode Electrodes Caused by Local Fuel Starvation. *J. Electrochem. Soc.* **2008**, *155* (10), B979–B984.
- (111) Evans, R. C.; Austin, R.; Miller, R. C.; Preston, A.; Nilsson, Z. N.; Ma, K.; Sambur, J. B. Surface-Facet-Dependent Electrochromic Properties of WO₃ Nanorod Thin Films: Implications for Smart Windows. *ACS Appl. Nano Mater.* **2021**, *4* (4), 3750–3759. <https://doi.org/10.1021/acsnm.1c00215>.
- (112) Ding, J.; Chai, Y.; Liu, Q.; Liu, X.; Ren, J.; Dai, W.-L. Selective Deposition of Silver Nanoparticles onto WO₃ Nanorods with Different Facets: The Correlation of Facet-Induced Electron Transport Preference and Photocatalytic Activity. *J. Phys. Chem. C* **2016**, *120* (8), 4345–4353. <https://doi.org/10.1021/acs.jpcc.5b10580>.
- (113) Murphy, C. J.; Jana, N. R. Controlling the Aspect Ratio of Inorganic Nanorods and Nanowires. *Adv. Mater.* **2002**, *14* (1), 80–82. [https://doi.org/10.1002/1521-4095\(20020104\)14:1<80::AID-ADMA80>3.0.CO;2-#](https://doi.org/10.1002/1521-4095(20020104)14:1<80::AID-ADMA80>3.0.CO;2-#).
- (114) Hai, B.; Shukla, A. K.; Duncan, H.; Chen, G. The Effect of Particle Surface Facets on the Kinetic Properties of LiMn_{1.5}Ni_{0.5}O₄ Cathode Materials. *J Mater Chem A* **2013**, *1* (3), 759–769. <https://doi.org/10.1039/C2TA00212D>.
- (115) Wang, Q.; Shen, L.; Xue, T.; Cheng, G.; Huang, C. Z.; Fan, H. J.; Feng, Y. P. Single-Crystalline TiO₂(B) Nanobelts with Unusual Large Exposed 100 Facets and Enhanced Li-Storage Capacity. *Adv. Funct. Mater.* **2021**, *31* (2), 2002187. <https://doi.org/10.1002/adfm.202002187>.
- (116) Besnardiere, J.; Ma, B.; Torres-Pardo, A.; Wallez, G.; Kabbour, H.; González-Calbet, J. M.; Von Bardeleben, H. J.; Fleury, B.; Buissette, V.; Sanchez, C.; Le Mercier, T.; Cassaignon, S.; Portehault, D. Structure and Electrochromism of Two-Dimensional Octahedral Molecular Sieve h⁺-WO₃. *Nat. Commun.* **2019**, *10* (1), 327. <https://doi.org/10.1038/s41467-018-07774-x>.
- (117) Li, Y.; McMaster, W. A.; Wei, H.; Chen, D.; Caruso, R. A. Enhanced Electrochromic Properties of WO₃ Nanotree-like Structures Synthesized via a Two-Step Solvothermal Process Showing Promise for Electrochromic Window Application. *ACS Appl. Nano Mater.* **2018**, *1* (6), 2552–2558. <https://doi.org/10.1021/acsnm.8b00190>.
- (118) Vasilopoulou, M.; Soutati, A.; Georgiadou, D. G.; Stergiopoulos, T.; Palilis, L. C.; Kennou, S.; Stathopoulos, N. A.; Davazoglou, D.; Argitis, P. Hydrogenated Under-Stoichiometric Tungsten Oxide Anode Interlayers for Efficient and Stable Organic Photovoltaics. *J Mater Chem A* **2014**, *2* (6), 1738–1749. <https://doi.org/10.1039/C3TA13975A>.

- (119) Kanamura, K.; Tamura, H.; Takehara, Z. XPS Analysis of a Lithium Surface Immersed in Propylene Carbonate Solution Containing Various Salts. *J. Electroanal. Chem.* **1992**, 333 (1–2), 127–142. [https://doi.org/10.1016/0022-0728\(92\)80386-I](https://doi.org/10.1016/0022-0728(92)80386-I).
- (120) Stickle, W.; Stickle, T. Propylene Carbonate - XPS Reference Spectra. *Surf. Sci. Spectra* **2014**, 21 (1), 28–34. <https://doi.org/10.1116/11.20140301>.
- (121) Arvizu, M. A.; Wen, R.-T.; Primetzhofer, D.; Klemberg-Sapieha, J. E.; Martinu, L.; Niklasson, G. A.; Granqvist, C. G. Galvanostatic Ion Detrapping Rejuvenates Oxide Thin Films. *ACS Appl. Mater. Interfaces* **2015**, 7 (48), 26387–26390. <https://doi.org/10.1021/acsami.5b09430>.
- (122) Baloukas, B.; Arvizu, M. A.; Wen, R.-T.; Niklasson, G. A.; Granqvist, C. G.; Vernhes, R.; Klemberg-Sapieha, J. E.; Martinu, L. Galvanostatic Rejuvenation of Electrochromic WO₃ Thin Films: Ion Trapping and Detrapping Observed by Optical Measurements and by Time-of-Flight Secondary Ion Mass Spectrometry. *ACS Appl. Mater. Interfaces* **2017**, 9 (20), 16995–17001. <https://doi.org/10.1021/acsami.7b01260>.
- (123) Wen, R.-T.; Arvizu, M. A.; Morales-Luna, M.; Granqvist, C. G.; Niklasson, G. A. Ion Trapping and Detrapping in Amorphous Tungsten Oxide Thin Films Observed by Real-Time Electro-Optical Monitoring. *Chem. Mater.* **2016**, 28 (13), 4670–4676.
- (124) Bisquert, J. Fractional Diffusion in the Multiple-Trapping Regime and Revision of the Equivalence with the Continuous-Time Random Walk. *Phys. Rev. Lett.* **2003**, 91 (1).
- (125) Bisquert, J. Beyond the Quasistatic Approximation: Impedance and Capacitance of an Exponential Distribution of Traps. *Phys. Rev. B* **2008**, 77 (23), 235203.
- (126) Jiménez, J. M.; Bourret, G. R.; Berger, T.; McKenna, K. P. Modification of Charge Trapping at Particle/Particle Interfaces by Electrochemical Hydrogen Doping of Nanocrystalline TiO₂. *J. Am. Chem. Soc.* **2016**, 138 (49), 15956–15964.
- (127) Bisquert, J. Analysis of the Kinetics of Ion Intercalation - Ion Trapping Approach to Solid-State Relaxation Processes. *Electrochimica Acta* **2002**, 47 (15), 2435–2449.
- (128) Wang, A.; Kadam, S.; Li, H.; Shi, S.; Qi, Y. Review on Modeling of the Anode Solid Electrolyte Interphase (SEI) for Lithium-Ion Batteries. *Npj Comput. Mater.* **2018**, 4 (1), 15. <https://doi.org/10.1038/s41524-018-0064-0>.
- (129) Wang, X.; Tian, F. H.; Zhao, W.; Fu, A.; Zhao, L. Surface Stabilization of Hexagonal WO₃ by Non-Metallic Atoms: A DFT Study. *Comput. Mater. Sci.* **2013**, 68, 218–221. <https://doi.org/10.1016/j.commatsci.2012.10.022>.
- (130) Goodenough, J. B.; Kim, Y. Challenges for Rechargeable Li Batteries. *Chem. Mater.* **2010**, 22 (3), 587–603. <https://doi.org/10.1021/cm901452z>.
- (131) Li, S.; Jiang, Z.; Han, J.; Xu, Z.; Wang, C.; Huang, H.; Yu, C.; Lee, S.-J.; Pianetta, P.; Ohldag, H.; Qiu, J.; Lee, J.-S.; Lin, F.; Zhao, K.; Liu, Y. Mutual Modulation between Surface Chemistry and Bulk Microstructure within Secondary Particles of Nickel-Rich Layered Oxides. *Nat. Commun.* **2020**, 11 (1), 4433. <https://doi.org/10.1038/s41467-020-18278-y>.
- (132) Yuan, G.; Hua, C.; Khan, S.; Jiang, S.; Wu, Z.; Liu, Y.; Wang, J.; Song, C.; Han, G. Improved Electrochromic Performance of WO₃ Films with Size Controlled Nanorods. *Electrochimica Acta* **2018**, 260, 274–280. <https://doi.org/10.1016/j.electacta.2017.10.193>.
- (133) Vemuri, R. S.; Bharathi, K. K.; Gullapalli, S. K.; Ramana, C. V. Effect of Structure and Size on the Electrical Properties of Nanocrystalline WO₃ Films. *ACS Appl. Mater. Interfaces* **2010**, 2 (9), 2623–2628. <https://doi.org/10.1021/am1004514>.
- (134) Lee, S.-H.; Deshpande, R.; Parilla, P. A.; Jones, K. M.; To, B.; Mahan, A. H.; Dillon, A. C. Crystalline WO₃ Nanoparticles for Highly Improved Electrochromic Applications. *Adv. Mater.* **2006**, 18 (6), 763–766. <https://doi.org/10.1002/adma.200501953>.
- (135) Kim, H.; Choi, D.; Kim, K.; Chu, W.; Chun, D.-M.; Lee, C. S. Effect of Particle Size and Amorphous Phase on the Electrochromic Properties of Kinetically Deposited WO₃ Films. *Sol. Energy Mater. Sol. Cells* **2018**, 177, 44–50. <https://doi.org/10.1016/j.solmat.2017.06.010>.

- (136) Subrahmanyam, A.; Karuppasamy, A. Optical and Electrochromic Properties of Oxygen Sputtered Tungsten Oxide (WO₃) Thin Films. *Sol. Energy Mater. Sol. Cells* **2007**, *91* (4), 266–274. <https://doi.org/10.1016/j.solmat.2006.09.005>.
- (137) Sallard, S.; Brezesinski, T.; Smarsly, B. M. Electrochromic Stability of WO₃ Thin Films with Nanometer-Scale Periodicity and Varying Degrees of Crystallinity. *J. Phys. Chem. C* **2007**, *111* (19), 7200–7206. <https://doi.org/10.1021/jp068499s>.
- (138) Schlotter, P. High Contrast Electrochromic Tungsten Oxide Layers. *Sol. Energy Mater.* **1987**, *16* (1), 39–46. [https://doi.org/10.1016/0165-1633\(87\)90006-2](https://doi.org/10.1016/0165-1633(87)90006-2).
- (139) Yoo, S. J.; Lim, J. W.; Sung, Y.-E. Improved Electrochromic Devices with an Inorganic Solid Electrolyte Protective Layer. *Sol. Energy Mater. Sol. Cells* **2006**, *90* (4), 477–484. <https://doi.org/10.1016/j.solmat.2005.04.033>.
- (140) Arvizu, M. A.; Qu, H.-Y.; Cindemir, U.; Qiu, Z.; Rojas-González, E. A.; Primetzhofer, D.; Granqvist, C. G.; Österlund, L.; Niklasson, G. A. Electrochromic WO₃ Thin Films Attain Unprecedented Durability by Potentiostatic Pretreatment. *J. Mater. Chem. A* **2019**, *7* (6), 2908–2918. <https://doi.org/10.1039/C8TA09621J>.
- (141) Evans, R. C.; Nilsson, Z.; Balch, B.; Wang, L.; Neilson, J. R.; Weinberger, C. R.; Sambur, J. B. Quantifying Capacitive-Like and Battery-Like Charge Storage Contributions Using Single-Nanoparticle Electro-Optical Imaging. *ChemElectroChem* **2020**, *7* (3), 753–760. <https://doi.org/10.1002/celec.201902011>.
- (142) Forghani, M.; Donne, S. W. Method Comparison for Deconvoluting Capacitive and Pseudo-Capacitive Contributions to Electrochemical Capacitor Electrode Behavior. *J. Electrochem. Soc.* **2018**, *165* (3), A664–A673. <https://doi.org/10.1149/2.0931803jes>.
- (143) Forghani, M.; Donne, S. W. Complications When Differentiating Charge Transfer Processes in Electrochemical Capacitor Materials: Assessment of Cyclic Voltammetry Data. *J. Electrochem. Soc.* **2019**, *166* (8), A1370–A1379. <https://doi.org/10.1149/2.1021906jes>.
- (144) Costentin, C.; Porter, T. R.; Savéant, J.-M. How Do Pseudocapacitors Store Energy? Theoretical Analysis and Experimental Illustration. *ACS Appl. Mater. Interfaces* **2017**, *9* (10), 8649–8658. <https://doi.org/10.1021/acsami.6b14100>.
- (145) Bard, A. J.; Faulkner, L. R. *Electrochemical Methods: Fundamentals and Applications*, 2nd ed.; Wiley: New York, 2001.
- (146) Ali Eftekhari; Mohamed Mohamedi. Tailoring Pseudocapacitive Materials from a Mechanistic Perspective. *Mater. Today Energy* **2017**, *6*, 211–229. <https://doi.org/10.1016/j.mtener.2017.10.009>.
- (147) Costentin, C.; Savéant, J.-M. Energy Storage: Pseudocapacitance in Prospect. *Chem. Sci.* **2019**, *10* (22), 5656–5666. <https://doi.org/10.1039/C9SC01662G>.
- (148) Bertus, L. M.; Faure, C.; Danine, A.; Labrugere, C.; Campet, G.; Rougier, A.; Duta, A. Synthesis and Characterization of WO₃ Thin Films by Surfactant Assisted Spray Pyrolysis for Electrochromic Applications. *Mater. Chem. Phys.* **2013**, *140* (1), 49–59. <https://doi.org/10.1016/j.matchemphys.2013.02.047>.
- (149) Mitchell, J. B.; Lo, W. C.; Genc, A.; LeBeau, J.; Augustyn, V. Transition from Battery to Pseudocapacitor Behavior via Structural Water in Tungsten Oxide. *Chem. Mater.* **2017**, *29* (9), 3928–3937. <https://doi.org/10.1021/acs.chemmater.6b05485>.
- (150) Nam, K. W.; Kim, S.; Lee, S.; Salama, M.; Shterenberg, I.; Gofer, Y.; Kim, J.-S.; Yang, E.; Park, C. S.; Kim, J.-S.; Lee, S.-S.; Chang, W.-S.; Doo, S.-G.; Jo, Y. N.; Jung, Y.; Aurbach, D.; Choi, J. W. The High Performance of Crystal Water Containing Manganese Birnessite Cathodes for Magnesium Batteries. *Nano Lett.* **2015**, *15* (6), 4071–4079. <https://doi.org/10.1021/acs.nanolett.5b01109>.
- (151) Zhou, Y.; Peng, Y.; Yin, Y.; Zhou, F.; Liu, C.; Ling, J.; Lei, L.; Zhou, W.; Tang, D. Modulating Memristive Performance of Hexagonal WO₃ Nanowire by Water-Oxidized Hydrogen Ion Implantation. *Sci. Rep.* **2016**, *6* (1), 32712. <https://doi.org/10.1038/srep32712>.
- (152) Chen, D.; Wang, J.-H.; Chou, T.-F.; Zhao, B.; El-Sayed, M. A.; Liu, M. Unraveling the Nature of Anomalously Fast Energy Storage in T-Nb₂O₅. *J. Am. Chem. Soc.* **2017**, *139* (20), 7071–7081. <https://doi.org/10.1021/jacs.7b03141>.

- (153) Koçer, C. P.; Griffith, K. J.; Grey, C. P.; Morris, A. J. Cation Disorder and Lithium Insertion Mechanism of Wadsley–Roth Crystallographic Shear Phases from First Principles. *J. Am. Chem. Soc.* **2019**, *141* (38), 15121–15134. <https://doi.org/10.1021/jacs.9b06316>.
- (154) Voskanyan, A. A.; Abramchuk, M.; Navrotsky, A. Entropy Stabilization of TiO₂–Nb₂O₅ Wadsley–Roth Shear Phases and Their Prospects for Lithium-Ion Battery Anode Materials. *Chem. Mater.* **2020**, *32* (12), 5301–5308. <https://doi.org/10.1021/acs.chemmater.0c01553>.
- (155) Yang, Y.; Zhao, J. Wadsley–Roth Crystallographic Shear Structure Niobium-Based Oxides: Promising Anode Materials for High-Safety Lithium-Ion Batteries. *Adv. Sci.* *n/a* (n/a), 2004855. <https://doi.org/10.1002/advs.202004855>.
- (156) Shao, H.; Lin, Z.; Xu, K.; Taberna, P.-L.; Simon, P. Electrochemical Study of Pseudocapacitive Behavior of Ti₃C₂T_x MXene Material in Aqueous Electrolytes. *Energy Storage Mater.* **2019**, *18*, 456–461. <https://doi.org/10.1016/j.ensm.2018.12.017>.

APPENDIX A



LIST OF ABBREVIATIONS

- h-WO₃ is hexagonal tungsten trioxide
- TEM is transmission electron microscope
- SPRM is surface plasmon resonance microscopy
- FT-IR is Fourier transform infrared
- NMR is nuclear magnetic resonance
- ITO is indium tin oxide
- OD is optical density
- SEM is scanning electron microscope
- PXRD is powder x-ray diffraction
- AFM is atomic force microscope
- DAQ is data acquisition
- LED is light emitting diode
- CCD is charge coupled device
- EM-CCD is electron multiplying charge coupled device
- TTL is camera trigger signal
- NP is nanoparticle
- LOD is limit of detection
- HW is hexagonal window
- SW is square window
- TC is trigonal cavity
- XPS is x-ray photoelectron
- CE is coloration efficiency
- FFT is fast Fourier transform

- EIS is electrochemical impedance spectroscopy
- SEI is solid electrolyte interface
- E_{onset} is the onset potential